

THESIS

2

2004

5662 1799

LIBRARY
Michigan State
University

This is to certify that the
dissertation entitled

**SOLID-STATE NUCLEAR MAGNETIC RESONANCE
STRUCTURAL STUDIES OF THE HIV-1 FUSION
PEPTIDE IN THE MEMBRANE ENVIRONMENT**

presented by

Jun Yang

has been accepted towards fulfillment
of the requirements for the

Ph.D. degree in Chemistry

David P. Wality

Major Professor's Signature

9/12/03

Date

PLACE IN RETURN BOX to remove this checkout from your record.
TO AVOID FINES return on or before date due.
MAY BE RECALLED with earlier due date if requested.

DATE DUE	DATE DUE	DATE DUE

**SOLID-STATE NUCLEAR MAGNETIC RESONANCE STRUCTURAL STUDIES
OF THE HIV-1 FUSION PEPTIDE IN THE MEMBRANE ENVIRONMENT**

By

Jun Yang

A DISSERTATION

Submitted to
Michigan State University
In partial fulfillment of the requirements
For the degree of

DOCTOR OF PHILOSOPHY

Department of Chemistry

2003

ABSTRACT

SOLID-STATE NUCLEAR MAGNETIC RESONANCE STRUCTURAL STUDIES OF THE HIV-1 FUSION PEPTIDE IN THE MEMBRANE ENVIRONMENT

By

Jun Yang

Solid-state nuclear magnetic resonance (NMR) spectroscopy was applied to understand the structures of a synthetic peptide representing the 23-residue N-terminal fusion peptide domain of the HIV-1 gp41 envelope glycoprotein in the membrane environment. Numerous biochemical and biophysical studies have shown that the free peptide by itself can cause the fusion of liposome without the rest of the glycoprotein. Hence, the information provided by the free peptide should be applicable to learn the mechanism of HIV-1 viral fusion with the host cells.

The wild peptide and a series of its variant peptides were synthesized and examined for their physical properties and their biological activities toward large unilamellar vesicles that were made with different lipid compositions. These measurements provided evidence that the probed peptide structures were indeed biologically relevant.

Peptides were ^{13}C carbonyl carbon labeled and/or ^{15}N amide nitrogen labeled at different residues according to the requirement of specific solid-state NMR experiments. Sample preparation studies provided the protocol so that only the contribution from membrane-bound fusion peptide is observed in the solid-state NMR measurement. The initial linewidth measurements of singly ^{13}C carbonyl labeled peptides showed that a

significant population of the membrane-bound peptide is well structured in its N-terminal and central regions while the C-terminus has more disorder. There was some dependence of linewidth on lipid composition, with narrower linewidth and hence greater structural order observed for a lipid composition comparable to that found in the virus-infected host cells. In the ordered N-terminal and central regions of the peptide, the ^{13}C carbonyl chemical shifts are consistent with a β strand membrane-bound conformation. Additional evidence for a β strand membrane-bound conformation was provided by analysis of two-dimensional rotor-synchronized magic angle spinning NMR spectra of doubly ^{13}C carbonyl labeled peptides.

The β strand structure was further investigated in terms of its oligomeric state by applying solid-state NMR rotational-echo double-resonance spectroscopy (REDOR). Comparison of REDOR spectra on samples that were labeled at different residue positions suggests that there are both parallel and anti-parallel arrangements of peptide strands in the oligomers. In the parallel arrangement, inter-peptide hydrogen bonding decreases toward the C-terminus while in the anti-parallel arrangement, hydrogen bonds are observed along the entire length of residues that was probed (Gly-5 to Gly-16). For the parallel arrangement, these observations are consistent with the model in which the apolar N-terminal and central regions of the peptides penetrate into the membrane and hydrogen bond with one another while the polar C-terminus of the peptide is outside the membrane and hydrogen bonds with water. These measurements show that at least at the end state of fusion, the peptide can adopt an oligomeric β strand structure.

Dedicated to my family, especially my lovely wife.

ACKNOWLEDGMENTS

This work would not have been possible if not for the help and support of many people. First and foremost I would like to thank my advisor, Dr. David P. Weliky. Through his guidance and example I have learned much of what it means to be a scientist, teacher and mentor.

I also want to thank my committee members, Drs. Gregory. L. Baker, John. L. McCracken and James Geiger for being supportive and providing me helpful critiques of my dissertation. I would like to thank Dr. Robert E. Maleczka, Jr. for lending the advice and support throughout my graduate career and Drs. Babak Borhan, Honggao Yan and David L. DeWitt for giving me the opportunities to run experiments in their labs.

The Max T. Rogers NMR Facility and the MSU Mass Spectrometry Facility all provided me the indispensable technical support for my work. I sincerely thank the faculties and staffs there for their assistance.

I would like to thank all the past and present members of the Weliky group for their friendship and partnership in science. Special thanks to Dr. Charles Gabrys, for his patience and selfless help during my research, and Paul Parkanzky, Christian Canlas, Rong Yang, Chris Wasniewski, Michele Bodner, Zhaoxiong Zheng (Norm), Vamshi Cotla and Robert Boes for sharing the expertise of science and happiness of life with me and making the years at MSU such an enjoyable experience to me. I wish all of you good luck in your NMR adventure!

I cannot thank life enough for bringing me the most wonderful friends! Ouyang, Yinghui, Yang and Wei, thank you for sharing with me such a loyal friendship. Janathon

and Wendy for your selfless help over the years. And for all my dear friends, thank you all for creating a positive and uplifting friend circle and being my cheerleaders whenever need. My life is so blessed with all of you!

As always, the past five years' journey will not be successful without the support from my family, my mom, dad, little sister, and grandparents. I can never tell you how much your love means to me. With you, my faith in the virtues of human nature will never die. Finally, my deep thanks go to Zhengyi for being a considerate and supportive wife. There is not an easy way to tell you my appreciation of the love, encouragement and trust that you have translated in a unique way. I am so glad that we will take the many new journeys ahead together.

TABLE OF CONTENTS

	Page
LIST OF TABLES	ix
LIST OF FIGURES.....	x
LIST OF SYMBOLS AND ABBREVIATIONS	xv
<u>CHAPTER I. INTRODCUTION</u>	1
BACKGROUND	2
REFERENCE	8
<u>CHAPTER II. PHYSICAL AND BIOLOGICAL PROPERTIES OF THE FUSION PEPTIDE</u>	12
BACKGROUND	13
MATERIALS AND METHODS	13
RESULTS AND DISCUSSION	18
Peptide Aggregation in Aqueous Solution	18
Peptide Overall Structure in Solution	26
Peptide-Induced Fusion of LM Vesicles	28
CONCLUSION	32
REFERENCE	34
<u>CHAPTER III. CONFORMATIONAL STUDIES OF THE MEMBRANE-ASSOCIATED FUSION PEPTIDE BY SOLID-STATE ONE-DIMENSIONAL NMR MEASUREMENTS</u>	36
BACKGROUND	37
METHODS	38
RESULTS AND DISCUSSION	42
Peptide binding to Lipids	42
Dependence of 1D NMR Spectra on Sample Conditions	44
1D NMR Spectral Scanning down the FP23 Backbone	51
Correlation of Carbonyl Chemical Shifts with Secondary Structure	53
Structure Similarity of Membrane-Associated FP, FPK3, FPW, and FPK3W	54
CONCLUSION	56
REFERENCE	57
<u>CHAPTER IV. CONFORMATIONAL STUDIES OF THE MEMBRANE-ASSOCIATED FUSION PEPTIDE BY SOLID-STATE TWO-DIMENSIONAL EXCHANGE NMR MEASUREMENTS</u>	58

BACKGROUND	59
METHODS	61
RESULTS AND DISCUSSION	63
Model Studies	63
2D Exchange Measurements for Refined Secondary Structure Determination of Membrane-Associated Fusion Peptide	66
CONCLUSION	70
REFERENCE	71
<u>CHAPTER V. DESIGN AND OPTIMIZATION OF SOLID-STATE ROTATIONAL- ECHO DOUBLE-RESONANCE (REDOR) MEASUREMENTS TO PROBE DISTANCES BETWEEN CARBONYL CARBONS AND AMIDE NITROGENS</u>	73
BACKGROUND	74
MATERIALS AND METHODS	75
RESULTS AND DISCUSSION	78
Quality of REDOR π Pulses	78
^1H Decoupling Sequence and Strength in REDOR Experiments ...	85
Selection of REDOR Sequences	91
CONCLUSION	104
REFERENCE	106
<u>CHAPTER VI. OLIGOMERIZATION STUDIES OF THE MEMBRANE- ASSOCIATED FUSION PEPTIDE BY REDOR MEASUREMENTS: PARALLEL VS. ANTI-PARALLEL STRAND ARRANGEMENTS</u>	108
BACKGROUND	109
MATERIALS AND METHODS	111
RESULTS	113
REDOR Simulations of Multiple ^{15}N Coupled to ^{13}C	113
REDOR Control Experiments	117
REDOR Experiments to Probe Inter-Peptide Hydrogen Bonding	121
DISCUSSION AND CONCLUSION	128
REFERENCE	131
<u>CHAPTER VI. SUMMARY AND FUTURE DIRECTIONS OF THE RESEARCH</u>	134
REFERENCE	140

LIST OF TABLES

	Page
<u>CHAPTER II</u>	
Table 1. FP Peptide Aggregation in Different Aqueous Buffer Solutions	21
<u>CHAPTER III</u>	
Table 2. Fusion Peptides Binding to Membranes	43
Table 3. Structural Correlations from Carbonyl Chemical Shift Analysis	53
<u>CHAPTER IV</u>	
Table 4. Structural Correlations from 2D Exchange Measurements	69
<u>CHAPTER V</u>	
Table 5. Pulse Length at Different Positions in the 4 mm Rotor	80
Table 6. Pulse Length at Different Positions in the 6 mm Rotor	81
Table 7. Pulse Profile Adjustment and Corresponding REDOR Dephasing Ratio	84
Table 8. Dependence of REDOR $\Delta S/S_0$ on the ^1H Decoupling/ ^{15}N π Pulse Field Ratio	86
<u>CHAPTER VI</u>	
Table 9. REDOR Control Experiments	119
Table 10. REDOR Measurements to Probe Inter-Peptide Hydrogen Bonds	123

LIST OF FIGURES

Page

CHAPTER I

Figure 1. Model (left) and freeze fracture electron microscopy (right) of HIV virion (a) binding to, (b) fusion with, (c-d) forming large pore, and infecting host cell 3

Figure 2. Model of HIV fusion. FP: Fusion Peptide. Time sequence: left to right 3

CHAPTER II

Figure 3. Solution amide ^1H NMR spectra of (a) FP at pH 6.7, (b) FP at pH 3.7, (c) FPK3 at pH 6.4, and (d) FPK3 at pH 3.7 24

Figure 4. Sedimentation equilibrium experiments of (a) 80 μM FPK3W and (b) 80 μM FPW in buffer. In (a), the main panel shows the absorbance at 280 nm as a function of the centrifugal radius after reaching the equilibrium in 20 hours at 52,000 rpm. The best fit to the model for a single species was obtained with a molecular weight of ~ 2630 (shown as a solid line through the experimental points). The upper panel shows the residuals between the data and the fit. In (b), the logarithm of 280 nm absorbance is plotted as a function of $(\text{radius})^2$ at 5,000 rpm. The data are represented as dark circles and the dark dotted and light-dashed lines represent the expected results for FPW 100-mers and monomers, respectively 25

Figure 5. CD spectra of four 20 μM fusion peptide constructs in unbuffered water: FP (I), FPK3 (II), FPW (III), and FPK3W (IV); and in 5 mM HEPES buffer: FP (I'), FPK3 (II'), FPW (III'), and FPK3W (IV') 27

Figure 6. CD spectra of 20 μM FP peptide in unbuffered water (I), and a series of acidified water solutions at pH 5.0 (II), pH 4.1 (III), and pH 3.1 (IV). The pH is adjusted by adding a small amount of 30 mM HCl solution 27

Figure 7. FP-induced lipid mixing (top) and FP-promoted aqueous contents leakage (bottom) as observed by fluorescence assays at 37 °C. For the lipid-mixing assay, 150 μM LM-3 lipid was extruded into 100 nm diameter vesicles. Lipid mixing was induced with (I) 7.5 μM and (II) 1.5 μM FP. For the aqueous contents leakage assay, 80 μM LM-3 lipid was extruded into 100 nm diameter vesicles loaded with ANTS/DPX. Leakage was promoted by FP at (III) 4 μM and (IV) 1 μM concentrations 29

Figure 8. Lipid mixing induced by four fusion peptide constructs. In the assay, 150 μM LM3 was extruded into 100 nm diameter vesicles and mixing was induced by (I) 3 μM

and (I') 1.5 μM FP; (II) 3 μM and (II') 1.5 μM FPK3; (III) 3 μM and (III') 1.5 μM FPK3W; and (IV) 3 μM and (IV') 1.5 μM FPW 31

CHAPTER III

Figure 9. ^{13}C solid-state NMR spectra of (a) 5% polycrystalline AGG-(A1G2)_C peptide; (b) 20 mM frozen aqueous solution of HGRVGIYFGMK-F8_C epitope peptide; (c) 7.5 mM frozen aqueous solution of FP-(L7F8)_C; and (d) FP-(L7F8)_C/DTPC made by preparation method (2) at 1:20 peptide:lipid molar ratio. The AGG spectrum was taken at room temperature and the other spectra were taken at $-50\text{ }^{\circ}\text{C}$ 45

Figure 10. ^{13}C solid-state NMR spectra of samples made from FP-F8_C bound to (a) DTPC dispersion, (b) LM-1 dispersion, (c) LM-3 dispersion, and (d) 100 nm diameter LM-3 vesicles with a peptide:lipid molar ratio of (a), (b) 1:200 and (c), (d) 1:80; and spectra of samples made from FP-(G10F11)_C bound to LM-3 with a peptide:lipid molar ratio of (e) 1:100 and (f) 1:20 48

Figure 11. ^{13}C solid-state NMR spectra of samples made from FP-(L7F8)_C/DTPC with a peptide:lipid molar ratio of 1:200 by (a) method 1 and (b) method 2; and spectra of sample made from FPK3-L7_NF8_C/LM-3 with a peptide:lipid molar ratio of 1:100 by (c) method 1 and (d) method 3 50

Figure 12. ^{13}C solid-state NMR difference spectra of LM-bound (a) FP-A1_C, (b) FP-V2_C, (c) FP-F8_C, (d) FP-G10_C, (e) FP-F11_C, (f) FP-A14_C, (g) FP-A15_C, and (h) FP-A21_C. Samples were prepared by method 1 with a peptide:lipid molar ratio of 1:100 52

Figure 13. ^{13}C solid-state NMR spectra of membrane-associated fusion peptide samples with (a) FP-F8_CL9_N, (b) FPK3-F8_CL9_N, (c) FPW-F8_CL9_N, and (d) FPK3W-F8_CL9_N. Each sample contained $\sim 0.3\text{ }\mu\text{mol}$ peptide and $40\text{ }\mu\text{mol}$ LM3. The displayed REDOR-filtered difference spectra are dominated by the Phe-8 carbonyl signals 55

CHAPTER IV

Figure 14. 2D ^{13}C solid-state NMR exchange spectra of (a) 5% polycrystalline AGG-(A1G2)_C peptide, and (b) Melittin-(G3A4)_C/DTPC with a peptide:lipid molar ratio of 1:20. The corresponding secondary structure analyses are shown in (c) and (d), respectively. These analyses are displayed as contour plots of the total squared deviation χ^2 (normalized to spectral noise) between experimental and calculated off-diagonal crosspeak intensities for a grid of dihedral angles. The darkest region in each plot represents the best global fitting 65

Figure 15. 2D ^{13}C solid-state NMR exchange spectra of (a) FP-(A1V2)_C/LM-3, (b) FP-(L7F8)_C/DTPC, (c) FP-(G10F11)_C/LM-3, and (d) FP-(A14A15)_C/LM-3. Each spectrum represents the summation of 10-15 twelve-hour data blocks. Secondary structure analyses for (a)-(d) are shown respectively in (e)-(h). These analyses are displayed as contour plots of the total squared deviation χ^2 (normalized to spectral noise)

between the experimental and calculated off-diagonal crosspeak intensities for a grid of dihedral angles. The darkest regions represent values of χ^2 less than 6, 9, 12, and 12 for (e)-(h), respectively. Each lighter contour level represents an increase of two units in χ^2 68

CHAPTER V

Figure 16. ^{13}C -observed REDOR dephasing curve of calibrated $\Delta S/S_0$ for the 5% $1\text{-}^{13}\text{C}$, ^{15}N L-leucine sample placed at different positions in the 4 mm rotor. λ is the product of dipolar coupling D (195 Hz, calculated from the 2.5 \AA $^{13}\text{C}\text{-}^{15}\text{N}$ distance) and dephasing time T . All experiments used the pulse lengths from the central position. The filled triangles represent the results from two central 1/6 positions and the open triangles represent the results from two outer 1/6 positions. The results from the two outmost 1/6 positions are not shown because the signals are significantly attenuated 80

Figure 17. ^{13}C -observed REDOR dephasing curve of calibrated $\Delta S/S_0$ for the 10% $1\text{-}^{13}\text{C}$, ^{15}N glycine sample placed at different positions in the 6 mm rotor. A 195 Hz dipolar coupling D from 2.5 \AA $^{13}\text{C}\text{-}^{15}\text{N}$ distance was applied. All experiments used the pulse lengths from the central position. The filled triangles represent the results from two central 1/6 positions and the open triangles represent the results from two outer 1/6 positions. The half-filled triangles represent the results from two outmost 1/6 positions 81

Figure 18. ^{13}C -observed REDOR dephasing curve of calibrated $\Delta S/S_0$ for the MB(i+4)EK-A $_9\text{C}$ A $_{13}\text{N}$ peptide in full and 2/3 full 4 mm rotor (open and filled upper triangles " Δ "), and in full and 2/3 full 6 mm rotor (open and filled lower triangles " ∇ "). 100 kHz and 65 kHz TPPM decoupling were applied for the 4 mm and 6 mm rotors, respectively 82

Figure 19. ^{13}C -observed REDOR (a) S_0 intensity and (b) calibrated $\Delta S/S_0$ for the MB(i+4)EK-A $_9\text{C}$ A $_{13}\text{N}$ peptide in the 4 mm rotor. A 42 Hz dipolar coupling D from a 4.2 \AA $^{13}\text{C}\text{-}^{15}\text{N}$ distance was applied. The filled and open triangles represent the results with TPPM and CW decoupling sequences, respectively. The upper (Δ) and lower (∇) triangles represent the results with 100 kHz and 70 kHz decoupling field, respectively 88

Figure 20. ^{13}C -observed REDOR calibrated $\Delta S/S_0$ for (a) 10% $1\text{-}^{13}\text{C}$, ^{15}N Glycine with 196 Hz dipolar coupling D (2.50 \AA), and (b) FP-F $_8\text{C}$ L $_9\text{N}$ peptide with 1165 Hz dipolar coupling D (1.38 \AA) in the 2/3 full 4 mm rotor. The upper (Δ) and lower (∇) triangles represent the results with 100 kHz and 65 kHz TPPM decoupling field, respectively 89

Figure 21. ^{13}C -observed REDOR calibrated $\Delta S/S_0$ for FP-F $_8\text{C}$ L $_9\text{N}$ peptide spinning at 16 kHz (open lower triangles) and 8 kHz (open upper triangles), 10% $1\text{-}^{13}\text{C}$, ^{15}N Glycine spinning at 16 kHz (half-filled lower triangles) and 8 kHz (half-filled upper triangles) (half-filled triangles), and MB(i+4)EK-A $_9\text{C}$ A $_{13}\text{N}$ peptide spinning at 8 kHz (filled lower triangles) and 4 kHz (filled upper triangles). All the experiments use 65 kHz TPPM decoupling. At each dephasing time for the same sample, the experiment running at lower speed contains half the amount of ^{15}N π pulses as the one at higher speed 90

Figure 22. Three REDOR sequences with (a) “all ^{15}N π pulse” version, (b) “alternating $^{15}\text{N}/^{13}\text{C}$ π pulse” version, and (c) “all ^{13}C π pulse” version. XY-8 phase cycling is shown in (a) and (b) and XY-4 phase cycling is shown in (c) 92

Figure 23. ^{13}C -observed REDOR (a) S_0 intensity and (b) calibrated $\Delta S/S_0$ for the 10% 1- ^{13}C , ^{15}N Glycine in the 2/3 full 4 mm rotor with all ^{15}N π pulse version (filled triangles), alternating $^{15}\text{N}/^{13}\text{C}$ π pulse version (half-filled triangles), and all ^{13}C π pulse version (open triangles). All REDOR experiments use 100 kHz TPPM decoupling. In (b), a calculated REDOR dephasing curve based on 196 Hz dipolar coupling (2.50 \AA ^{13}C - ^{15}N distance) is represented by the solid line 93

Figure 24. ^{13}C -observed REDOR calibrated $\Delta S/S_0$ for the FP-F8_CL9_N peptide in the 2/3 full 4 mm rotor using all ^{15}N π pulse version with 100 kHz (upper triangles) and 65 kHz (lower triangles) TPPM decoupling. The calculated REDOR dephasing curve based on 1165 Hz dipolar coupling (1.38 \AA ^{13}C - ^{15}N distance) is represented by the solid line 96

Figure 25. ^{13}C -observed REDOR calibrated $\Delta S/S_0$ for the MB(i+4)EK-A9_CA13_N peptide in the 2/3 full 4 mm rotor (filled triangles) and 6 mm rotor (open triangles). All ^{15}N π pulse version REDOR with 100 kHz (upper triangles) and 70 kHz (lower triangles) TPPM decoupling was used for the samples in the 4 mm rotor. All ^{15}N π pulse version (lower triangles) and alternating $^{15}\text{N}/^{13}\text{C}$ π pulse version (upper triangles) REDOR with 65 kHz TPPM decoupling were used for the samples in the 6 mm rotor. The calculated REDOR dephasing curve based on 42 Hz dipolar coupling (4.20 \AA ^{13}C - ^{15}N distance) is represented by the solid line 97

Figure 26. ^{13}C -observed REDOR (a) S_0 intensity and (b) calibrated $\Delta S/S_0$ MB(i+4)EK-A9_CA13_N peptide in the 2/3 full 6 mm rotor with alternating $^{15}\text{N}/^{13}\text{C}$ π pulse REDOR using $8n$ (upper triangles) and $8n + 2$ (lower triangles) rotor periods 99

Figure 27. ^{13}C -observed REDOR calibrated $\Delta S/S_0$ for the MB(i+4)EK-A9_CA13_N peptide in the 2/3 full 6 mm rotor using 40 kHz ^{15}N π pulse field (lower triangles) and 20 kHz ^{15}N π pulse field (upper triangles). The all ^{15}N π pulse REDOR with 65 kHz TPPM decoupling was used. The calculated REDOR dephasing curves based on 4.2 \AA (I), 4.3 \AA (II), 4.4 \AA (III), 4.5 \AA (IV), 4.6 \AA (V), and 4.7 \AA (VI) ^{13}C - ^{15}N distances are represented by solid lines 101

CHAPTER VI

Figure 28. Structure of the gp41 soluble ectodomain trimer. (A) Ribbon drawing of the trimer. (B) An end-on view looking down the 3-fold axis of the trimer..... 109

Figure 29. REDOR simulation from the SIMPSON program (triangles) and numeric calculation (solid line). A 44.4 Hz dipolar coupling D (4.1 \AA) was used in both cases 114

Figure 30. (a) Coordinates of one ^{13}C coupled to three adjacent ^{15}N in parallel and anti-parallel segments of streptococcal protein G B1 domain with the carbonyl carbon

hydrogen bonded to the middle amide nitrogen. (b) SIMPSON simulated REDOR dephasing ratios of the ^{13}C dephased by only hydrogen bonded ^{15}N (open circles), or two more adjacent ^{15}N in parallel strand arrangement (open upper triangles), or two more adjacent ^{15}N in anti-parallel strand arrangement (open lower triangles). The filled symbols represent the corresponding simulation results when all the distances are extended by a factor of 4.6/4.1 as the hydrogen bond distance expands from 4.1 Å to 4.6 Å based on the REDOR result of MK(i+4)-A9_CA13_N peptide at 24 ms dephasing time 116

Figure 31. ^{13}C solid-state NMR spectra of the FPK3-(G5A6L7)_C/FPK3-(A14A15G16)_N/LM-3 sample from (a) CP experiment and (b) S₀ REDOR experiment with a 24.0 ms dephasing time. The spectral intensities in each experiment were divided by the number of scans in that experiment. The vertical scale in (b) is 8 times that in (a), showing that the signal/scan in (b) is ~ 1/8 as large as that in (a). The (b) spectrum appears better resolved than the (a) spectrum because the natural abundance lipid carbonyls make a relatively smaller contribution to the S₀ signal than to the CP signal 117

Figure 32. ^{13}C solid-state NMR S₀ (left) and S₁ (right) REDOR spectra of membrane-associated fusion peptides that had (a) ~ 0.8 μmol each of FP-(F8L9G10)_C and FP-unlabeled, (b) ~ 0.8 μmol each of FP-(F8L9G10)_N and FP-unlabeled, (c) ~ 1.6 μmol FPK3-unlabeled, and (d) ~ 1.6 μmol FP-(F8L9G10)_N. Each of the samples in (a-d) also contained 40 μmol lipid and 20 μmol cholesterol. For samples (a-c), LM-3 lipid mixture was used and for sample (d), LM-4 lipid mixture was used 120

Figure 33. ^{13}C solid-state NMR S₀ and S₁ REDOR spectra of membrane-associated fusion peptides. Each sample was made with LM-3 lipid mixture, ~ 0.8 μmol peptide with selective ^{13}C carbonyl labeling and ~ 0.8 μmol peptide with selective ^{15}N amide labeling. The specific labeling schemes were: (a) FPK3-(G5A6L7)_C/FPK3-(G5A6L7)_N, (b) FP-(F8L9G10)_C/FP-(F8L9G10)_N, (c) FP-(F11L12G13)_C/FP-(F11L12G13)_N, (d) FPK3-(A14A15G16)_C/FPK3-(A14A15G16)_N, (e) FPK3-(G5A6L7)_C/FPK3-(A14A15G16)_N, (f) FP-(F8L9G10)_C/FP-(F11L12G13)_N, (g) FP-(F11L12G13)_C/FP-(F8L9G10)_N, and (h) FPK3-(A14A15G16)_C/FPK3-(G5A6L7)_N. Samples (a)-(d) primarily probed the presence of parallel strand arrangements and samples (e)-(h) primarily probed the presence of anti-parallel strand arrangements. The dotted lines are included for visual comparison of the spectral intensities 124

Figure 34. Peptide oligomerization and membrane insertion models for the (a) parallel strand arrangement, and (b) anti-parallel strand arrangement. The arrows indicate the peptide direction from N-terminus to C-terminus while the numbers label the indices of individual residues. In the parallel arrangement, inter-peptide hydrogen bonding was observed at N-terminal and central regions, and considerably weaker toward the C-terminus, which is consistent with an apolar region of peptide insertion into membrane interior model. In the anti-parallel arrangement, inter-peptide hydrogen bonding was detected along the whole length of the probed region. Since this arrangement would place the polar region of one peptide and the apolar region of the other peptide at the same side, it is unclear whether it is a result of peptides binding on the surface of membrane or peptides inserting through the membrane 125

LIST OF SYMBOLS AND ABBREVIATIONS

1D/2D	One-Dimensional / Two-Dimensional
AIDS	Acquired Immune Deficiency Syndrome
ANTS	8-AminoNaphthalene-1,3,6-TriSulfonic acid
CD	Circular Dichroism
CP	Cross-Polarization
CSA	Chemical Shift Anisotropy
CW	Continuous Wave
DMPC	1,2-DiMyristoyl-sn-glycero-3-PhosphoCholine
DMPS	1,2-DiMyristoyl-sn-glycero-3-[Phospho-L-Serine]
DMSO	DiMethyl SulfOxide
DPPC-1- ¹³ C	1,2-DiPalmitoyl[1- ¹³ C]-sn-glycero-3-PhosphoCholine
DPX	<i>p</i> -xylene-bis-pyridinium bromide
DTPC	Di-o-Tetradecyl-sn-glycero-3-PhosphoCholine
FWHM	Full-Width-at-Half-Maximum
HEPES	N-2-HydroxyEthylPiperazine-N'-2-EthaneSulfonic acid
HIV	Human Immunodeficiency Virus
HPLC	High Performance Liquid Chromatography
IR	InfraRed
LUV	Large Unilamellar Vesicles
MALDI	Matrix Assisted Laser Desorption Ionization
MAS	Magic Angle Spinning

<i>N</i> -NBD-PE	<i>N</i> -(7-Nitro-2,1,3-BenzoxaDiazol-4-yl)-PhosphatidylEthanolamine
<i>N</i> -Rh-PE	<i>N</i> -(lissamine Rhodamine B sulfonyl)-PhosphatidylEthanolamine
NMR	Nuclear Magnetic Resonance
PI	PhosphatidylInositol
POPG	1-Palmitoyl-2-Oleoyl-sn-glycero-3-[Phospho-rac-(1-Glycerol)]
POPC	1-Palmitoyl-2-Oleoyl-sn-glycero-3-PhosphoCholine
POPE	1-Palmitoyl-2-Oleoyl-sn-glycero-3-PhosphoEthanolamine
POPS	1-Palmitoyl-2-Oleoyl-sn-glycero-3-[Phospho-L-Serine]
ppm	parts per million
REDOR	Rotational-Echo DOuble-Resonance spectroscopy
RF	RadioFrequency
TFA	TriFluoroacetic Acid
TPPM	Two-Pulse Phase-Modulation

CHAPTER I

INTRODUCTION

BACKGROUND

Fusion between cells and cellular components has an essential role in organismal life and is an integral part of critical processes such as egg fertilization and synaptic transmission in the nervous system. Membrane fusion is also an important step in viral infection for the widespread diseases measles, influenza and most seriously, acquired immunodeficiency syndrome (AIDS)¹. As a crucial step in the viral life cycle, viral fusion can be the potential target for anti-viral therapeutics. In March 2003, Roche and Trimeris, Inc. introduced the first U. S. Food and Drug Administration (FDA) approved anti-fusion treatment for human immunodeficiency virus type-1 (HIV-1), FUZEON™ (enfuvirtide), which is a peptide inhibitor that prevents fusion of the viral and cell membranes²⁻⁷. This drug also obtained the approval of European Commission to be used against HIV in the European Union. T-1249, a second-generation fusion inhibitor through the Roche/Trimeris partnership, is also in Phase I/II clinical testing.

Fusion between two membrane-bound bodies such as cells, viruses or vesicles is a protein-mediated process and is generally separated into three sequential steps⁸: (1) binding of the two bodies; (2) mixing of their membrane lipids; (3) formation of a large fusion pore through which the contents of virus and cell can mix. Figure 1 illustrates a series of freeze fracture electron micrographs that follow the time evolution of HIV virion infection of a host cell⁹.

In AIDS, fusion and infection are mediated by the heavily glycosylated, predominantly extraviral envelope proteins gp120 and gp41 which form a non-covalently bound complex. The complex is attached to the virus through a transmembrane segment in gp41. Conserved regions in the gp120 subunit are responsible for the binding of the

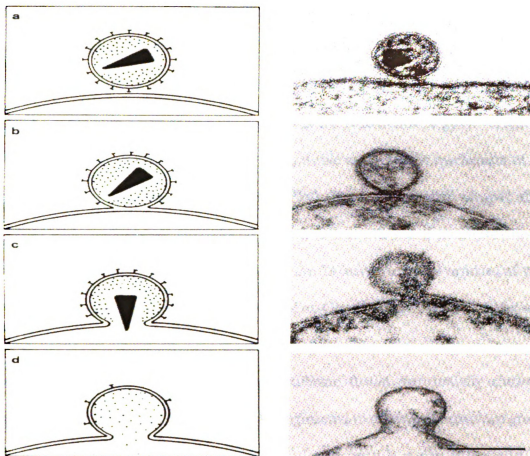


Figure 1. Model (left) and freeze fracture electron microscopy (right) of HIV virion (a) binding to, (b) fusion with, (c-d) forming large pore, and infecting host cell.

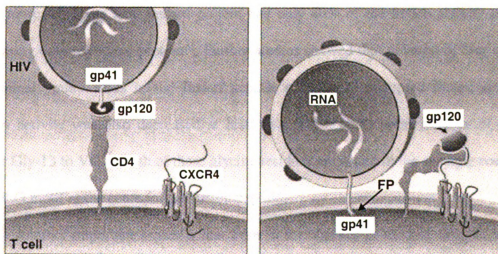


Figure 2. Model of HIV fusion. FP: Fusion Peptide. Time sequence: left to right.

virus to the CD4 and chemokine (e.g. CXCR4) receptors of human T and macrophage cells prior to fusion^{10, 11}. This interaction is followed by a series of poorly understood conformational changes which are believed to eventually lead to the exposure of a conserved segment of about twenty amino acids at the N-terminus of gp41¹² (Figure 2). This region has been proposed to have an integral role in the fusion mechanism of HIV and thus is given the name “Fusion Peptide (FP)”. The fusion peptide of gp41 shares homology with regions of other enveloped viruses, such as ortho- and paramyxoviruses¹³. A typical fusion peptide consensus sequence is the 23-mer N-terminal residues of gp41: Ala-Val-Gly-Ile-Gly-Ala-Leu-Phe-Leu-Gly-Phe-Leu-Gly-Ala-Ala-Gly-Ser-Thr-Met-Gly-Ala-Arg-Ser.

The importance of this region in membrane fusion was initially shown by mutation/fusion activity studies on HeLa cells engineered to express the envelope protein. Hydrophobic to polar mutations throughout the fusion peptide region decreased fusion activity by more than 50 times but had no effect on binding to the CD4 receptor¹⁴. Significantly, the Val-2 to Glu-2 mutation was trans-dominant, i.e. cells expressing ten times more wild-type than mutant protein had only 40% of the fusion activity of those expressing only wild-type protein¹⁵. Further studies showed that deletion of four or more N-terminal amino acids in the fusion peptide completely disrupted fusion activity¹⁶. Fusion activity was also decreased at least twenty-fold with point mutants of Gly-10 and/or Gly-13 to Val¹⁷. Both of these glycine residues are found in the strongly conserved FLGFLG motif at the center of the fusion peptide.

Another important aspect is that even in the absence of the rest of gp41, the 20-residue fusion peptide at ~10 μ M concentration and 1:20 – 1:100 peptide:lipid molar

ratios causes rapid fusion and/or leakage of lipid vesicles or erythrocytes. In these studies, fusion is detected fluorimetrically with assays which monitor (1) mixing of lipids from different vesicles, (2) mixing of contents between different vesicles, and/or (3) mixing of vesicle contents with the extravascular medium. In addition, the growth in the size of vesicles or erythrocytes in the presence of fusion peptide has been monitored with either light scattering or electron microscopy¹⁸⁻²⁶. Also the site-directed mutation/fusion activity or deletion/fusion activity studies showed the same pattern as is formed in the intact protein. In particular, (1) deletion of three or four N-terminal amino acids eliminates intervesicle lipid mixing and vesicle leakage^{19, 23}; (2) hydrophobic to polar point mutations also eliminate intervesicle lipid mixing and vesicle leakage^{24, 25, 27}; and (3) the Val-2 to Glu-2 point mutation peptide had a trans-dominant effect in mixtures with wild-type peptide. In these latter studies, lipid mixing was inhibited by a factor of four relative to having only wild-type peptide. The observed trans-dominant effect was attributed to the inability of the mutated peptide to form aggregates larger than dimer²⁴. These data provide strong evidence that the free fusion peptide is a good model system to probe biologically relevant fusion.

Despite its biological importance, there is no atomic-level structure of the fusion peptide region in membranes. The hydrophobicity of this region impairs the solubility requirement of traditional high-resolution structural techniques, such as crystallographic and solution nuclear magnetic resonance (NMR) analysis, and neither technique is suited to studies in intact membrane systems. Other techniques (e.g. circular dichroism, infrared, fluorescence, electron spin resonance, etc.) have provided general structural information about the membrane-bound fusion peptide. However, due to the difference in sample

preparation protocols, the results from these studies are complex and sometimes contradictory.

Circular dichroism (CD) measurements on the HIV-1 fusion peptide show significant helical character for samples in organic solvent^{24, 28-31}, in sodium dodecyl sulfate (SDS) detergent at a 1:200 peptide:lipid ratio^{24, 29, 32}, and in an environment of negatively charged vesicles with a 1:200 peptide:lipid molar ratio¹⁸. NMR studies on the peptide in SDS micelles are also consistent with a helical central region³⁰. By contrast, at 1:10 peptide:SDS molar ratio²⁹ or 1:30 peptide:lipid molar ratio¹⁸, there is significant β strand character. Similar results were found in 1:1 mixtures of neutral:negatively charged lipids³³.

With neutral lipid vesicles or erythrocyte ghosts at peptide:lipid molar ratios of ~ 1:200, there are two infrared reports of predominantly helical structure^{23, 29}, three reports of predominantly β structure^{18, 25, 34}, and one report of mixed helical and β structure²⁰. Two investigators report that the peptide conformation changes from helical to β as the peptide:lipid molar ratio is increased from 1:200 to 1:30^{23, 29} while two others report that the β conformation does not change with these ratios^{18, 25}. These differences in structure may have to do with differences in peptide sequence, lipid composition, sample preparation, or hydration level. A recent infrared study of the peptide in a neutral membrane monolayer was also consistent with a β structure³⁵.

Fluorescence and ESR measurements on derivatized HIV-1 fusion peptides in membrane vesicle environments provide evidence that the N-terminal and central regions are inserted into the membrane and the C-terminus is outside the membrane^{24, 29}. In some contrast, a H/D NMR exchange study in SDS micelles suggests that the N-terminus is

outside the micelle³⁶.

These complicated structure results suggest that residue-specific structural information is necessary because different regions of the peptide may adopt different structures. Solid-state NMR is suitable to this kind of structural measurement because unlike the X-ray technique, crystals are not required and the sample can be studied in a fully hydrated membrane environment. In solid-state NMR, orientational information is also retained in the system.

The goal of this study is to apply solid-state NMR methodologies to determine the structure of synthetic fusion peptide in a membrane environment. We will exploit isotopic labeling at specific positions to probe the secondary structures as well as the peptide oligomerization status of the peptide. These results will be incorporated with the orientation measurements of the peptide with respect to the membrane and the peptide effect on lipid dynamics and structure to understand HIV-1 viral fusion at a molecular level.

REFERENCE

1. Piel, J. (1988) *The Science of AIDS*, W. H. Freeman and Company, New York.
2. Wild, C. T., Shugars, D. C., Greenwell, T. K., McDanal, C. B., and Matthews, T. J. (1994) Peptides corresponding to a predictive alpha-helical domain of human immunodeficiency virus type 1 gp41 are potent inhibitors of virus infection. *Proc. Natl. Acad. Sci. U. S. A.* 91, 9770-9774.
3. Kilby, J. M., Hopkins, S., Venetta, T. M., DiMassimo, B., Cloud, G. A., Lee, J. Y., Alldredge, L., Hunter, E., Lambert, D., Bolognesi, D., Matthews, T., Johnson, M. R., Nowak, M. A., Shaw, G. M., and Saag, M. S. (1998) Potent suppression of HIV-1 replication in humans by T-20, a peptide inhibitor of gp41-mediated virus entry. *Nat. Med.* 4, 1302-1307.
4. Kilby, J. M., Lalezari, J. P., Eron, J. J., Carlson, M., Cohen, C., Arduino, R. C., Goodgame, J. C., Gallant, J. E., Volberding, P., Murphy, R. L., Valentine, F., Saag, M. S., Nelson, E. L., Sista, P. R., and Dusek, A. (2002) The safety, plasma pharmacokinetics, and antiviral activity of subcutaneous enfuvirtide (T-20), a peptide inhibitor of gp41-mediated virus fusion, in HIV-infected adults. *Aids Res. Hum. Retrovir.* 18, 685-693.
5. Barretina, J., Blanco, J., Armand-Ugon, M., Gutierrez, A., Clotet, B., and Este, J. A. (2003) Anti-HIV-1 activity of enfuvirtide (T-20) by inhibition of bystander cell death. *Antivir. Ther.* 8, 155-161.
6. Cooleya, L. A., and Lewin, S. R. (2003) HIV-1 cell entry and advances in viral entry inhibitor therapy. *J. Clin. Virol.* 26, 121-132.
7. Gulick, R. M. (2003) New antiretroviral drugs. *Clin. Microbiol. Infect.* 9, 186-193.
8. Hernandez, L. D., Hoffman, L. R., Wolfsberg, T. G., and White, J. M. (1996) Virus-cell and cell-cell fusion. *Annu. Rev. Cell Dev. Biol.* 12, 627-661.
9. Grewe, C., Beck, A., and Gelderblom, H. R. (1990) HIV: early virus-cell interaction. *J. Acq. Immun. Def. Synd.* 3, 965-974.
10. Bleul, C. C., Farzan, M., Choe, H., Parolin, C., ClarkLewis, I., Sodroski, J., and Springer, T. A. (1996) The lymphocyte chemoattractant SDF-1 is a ligand for LESTR/fusin and blocks HIV-1 entry. *Nature* 382, 829-833.
11. Oberlin, E., Amara, A., Bachelier, F., Bessia, C., Virelizier, J. L., ArenzanaSeisdedos, F., Schwartz, O., Heard, J. M., ClarkLewis, I., Legler, D. F., Loetscher, M., Baggiolini, M., and Moser, B. (1996) The CXC chemokine SDF-1

is the ligand for LESTR/fusin and prevents infection by T-cell-line-adapted HIV-1. *Nature* 382, 833-835.

12. Balter, M. (1996) New hope in HIV disease. *Science* 274, 1988-1989.
13. Gallaher, W. R. (1987) Detection of a fusion peptide sequence in the transmembrane protein of human-immunodeficiency-virus. *Cell* 50, 327-328.
14. Freed, E. O., Myers, D. J., and Risser, R. (1990) Characterization of the fusion domain of the human-immunodeficiency-virus type-1 envelope glycoprotein Gp41. *Proc. Natl. Acad. Sci. U. S. A.* 87, 4650-4654.
15. Freed, E. O., Delwart, E. L., Buchschacher, G. L., and Panganiban, A. T. (1992) A mutation in the human-immunodeficiency-virus type-1 transmembrane glycoprotein-gp41 dominantly interferes with fusion and infectivity. *Proc. Natl. Acad. Sci. U. S. A.* 89, 70-74.
16. Schaal, H., Klein, M., Gehrman, P., Adams, O., and Scheid, A. (1995) Requirement of N-terminal amino-acid-residues of gp41 For human-immunodeficiency-virus type 1-mediated cell fusion. *J. Virol.* 69, 3308-3314.
17. Delahunty, M. D., Rhee, I., Freed, E. O., and Bonifacino, J. S. (1996) Mutational analysis of the fusion peptide of the human immunodeficiency virus type 1: Identification of critical glycine residues. *Virology* 218, 94-102.
18. Rafalski, M., Lear, J. D., and Degrado, W. F. (1990) Phospholipid interactions of synthetic peptides representing the N-terminus of HIV gp41. *Biochemistry* 29, 7917-7922.
19. Slepishkin, V. A., Melikyan, G. B., Sidorova, M. S., Chumakov, V. M., Andreev, S. M., Manulyan, R. A., and Karamov, E. V. (1990) Interaction of human-immunodeficiency-virus (HIV-1) fusion peptides with artificial lipid-membranes. *Biochem. Biophys. Res. Commun.* 172, 952-957.
20. Martin, I., Defrisequertain, F., Decroly, E., Vandenbranden, M., Brasseur, R., and Ruyschaert, J. M. (1993) Orientation and structure of the NH₂-terminal HIV-1 gp41 peptide in fused and aggregated liposomes. *Biochim. Biophys. Acta* 1145, 124-133.
21. Nieva, J. L., Nir, S., Muga, A., Goni, F. M., and Wilschut, J. (1994) Interaction of the HIV-1 fusion peptide with phospholipid vesicles - different structural requirements for fusion and leakage. *Biochemistry* 33, 3201-3209.
22. Mobley, P. W., Lee, H. F., Curtain, C. C., Kirkpatrick, A., Waring, A. J., and Gordon, L. M. (1995) The amino-terminal peptide of HIV-1 glycoprotein-41 fuses human erythrocytes. *Biochim. Biophys. Acta-Mol. Basis Dis.* 1271, 304-314.

23. Martin, I., Schaal, H., Scheid, A., and Ruyschaert, J. M. (1996) Lipid membrane fusion induced by the human immunodeficiency virus type 1 gp41 N-terminal extremity is determined by its orientation in the lipid bilayer. *J. Virol.* 70, 298-304.
24. Kliger, Y., Aharoni, A., Rapaport, D., Jones, P., Blumenthal, R., and Shai, Y. (1997) Fusion peptides derived from the HIV type 1 glycoprotein 41 associate within phospholipid membranes and inhibit cell-cell fusion - Structure-function study. *J. Biol. Chem.* 272, 13496-13505.
25. Pereira, F. B., Goni, F. M., Muga, A., and Nieva, J. L. (1997) Permeabilization and fusion of uncharged lipid vesicles induced by the HIV-1 fusion peptide adopting an extended conformation: Dose and sequence effects. *Biophys. J.* 73, 1977-1986.
26. Nieva, J. L., Nir, S., and Wilschut, J. (1998) Destabilization and fusion of zwitterionic large unilamellar lipid vesicles induced by a beta-type structure of the HIV-1 fusion peptide. *J. Liposome Res.* 8, 165-182.
27. Pereira, F. B., Goni, F. M., and Nieva, J. L. (1995) Liposome destabilization induced by the HIV-1 fusion peptide effect of a single amino-acid substitution. *FEBS Lett.* 362, 243-246.
28. Slepishkin, V. A., Andreev, S. M., Sidorova, M. V., Melikyan, G. B., Grigoriev, V. B., Chumakov, V. M., Grinfeldt, A. E., Manukyan, R. A., and Karamov, E. V. (1992) Investigation of human-immunodeficiency-virus fusion peptides - analysis of interrelations between their structure and function. *Aids Res. Hum. Retrovir.* 8, 9-18.
29. Gordon, L. M., Curtain, C. C., Zhong, Y. C., Kirkpatrick, A., Mobley, P. W., and Waring, A. J. (1992) The amino-terminal peptide of HIV-1 glycoprotein-41 interacts with human erythrocyte membranes - peptide conformation, orientation and aggregation. *Biochim. Biophys. Acta* 1139, 257-274.
30. Chang, D. K., Chien, W. J., and Cheng, S. F. (1997) The FLG motif in the N-terminal region of glucoprotein 41 of human immunodeficiency virus type 1 adopts a type-I beta turn in aqueous solution and serves as the initiation site for helix formation. *Eur. J. Biochem.* 247, 896-905.
31. Waring, A. J., Mobley, P. W., and Gordon, L. M. (1998) Conformational mapping of a viral fusion peptide in structure- promoting solvents using circular dichroism and electrospray mass spectrometry. *Proteins*, 38-49.
32. Chang, D. K., Cheng, S. F., and Chien, W. J. (1997) The amino-terminal fusion domain peptide of human immunodeficiency virus type 1 gp41 inserts into the

- sodium dodecyl sulfate micelle primarily as helix with a conserved glycine at the micelle-water interface. *J. Virol.* 71, 6593-6602.
33. Mobley, P. W., Waring, A. J., Sherman, M. A., and Gordon, L. M. (1999) Membrane interactions of the synthetic N-terminal peptide of HIV-1 gp41 and its structural analogs. *Biochim. Biophys. Acta* 1418, 1-18.
 34. Peisajovich, S. G., Epan, R. F., Pritsker, M., Shai, Y., and Epan, R. M. (2000) The polar region consecutive to the HIV fusion peptide participates in membrane fusion. *Biochemistry* 39, 1826-1833.
 35. Taylor, S. E., Desbat, B., Blaudez, D., Jacobi, S., Chi, L. F., Fuchs, H., and Schwarz, G. (2000) Structure of a fusion peptide analogue at the air-water interface, determined from surface activity, infrared spectroscopy and scanning force microscopy. *Biophys. Chem.* 87, 63-72.
 36. Chang, D. K., and Cheng, S. F. (1998) Determination of the equilibrium micelle-inserting position of the fusion peptide of gp41 of human immunodeficiency virus type 1 at amino acid resolution by exchange broadening of amide proton resonances. *J. Biomol. NMR* 12, 549-552.

CHAPTER II

PHYSICAL AND BIOLOGICAL PROPERTIES OF THE FUSION PEPTIDE

BACKGROUND

The first step of the project involves the examination of the physical properties of the fusion peptide in aqueous solution before it binds to the membrane. The biological functionality of the peptide is also investigated.

In order to investigate the peptide structure in its native membrane environment, we need to ensure that the system is biologically relevant. As discussed in the previous chapter, the free fusion peptide without the rest of the gp41 protein has similar biological function as the intact protein. Therefore, a series of fusion assays were applied to the synthetic fusion peptide and the results were compared to those from other groups to prove that our sample system is indeed biologically relevant.

It is important that we can compare the physical properties of the fusion peptide before and after binding to the membrane and correlate any physical property differences with the biological functionality. Therefore we also examined the physical properties of the fusion peptide prior to membrane association.

MATERIALS AND METHODS

Materials. Rink amide resin was purchased from Advanced Chemtech (Louisville, KY), and 9-fluorenylmethoxycarbonyl (Fmoc)-amino acids were obtained from Peptides International (Louisville, KY). ^{13}C Carbonyl labeled amino acids were purchased from Icon Services Inc. (Summit, NJ) and the Fmoc group was added using literature methods^{1,2}. 1,2-Dimyristoyl-*sn*-glycero-3-phosphocholine (DMPC), 1,2-dimyristoyl-*sn*-glycero-3-[phospho-L-serine] (DMPS), 1,2-dipalmitoyl[1- ^{13}C]-*sn*-glycero-3-phosphocholine (DPPC-1- ^{13}C), di-*o*-tetradecyl-*sn*-glycero-3-phosphocholine

(DTPC), 1-palmitoyl-2-oleoyl-*sn*-glycero-3-[phospho-*rac*-(1-glycerol)] (POPG), 1-palmitoyl-2-oleoyl-*sn*-glycero-3-phosphocholine (POPC), 1-palmitoyl-2-oleoyl-*sn*-glycero-3-phosphoethanolamine (POPE), 1-palmitoyl-2-oleoyl-*sn*-glycero-3-[phospho-*L*-serine] (POPS), phosphatidylinositol (PI), sphingomyelin, *N*-(7-nitro-2,1,3-benzoxadiazol-4-yl)-phosphatidylethanolamine (*N*-NBD-PE), *N*-(lissamine Rhodamine B sulfonyl)-phosphatidylethanolamine (*N*-Rh-PE) and cholesterol were purchased from Avanti Polar Lipids, Inc. (Alabaster, AL). 8-aminonaphthalene-1,3,6-trisulfonic acid (ANTS) and *p*-xylene-bis-pyridinium bromide (DPX) were purchased from Molecular Probes (Eugene, OR). The Micro BCA (bicinchoninic acid) protein assay was obtained from Pierce (Rockford, IL). *N*-2-hydroxyethylpiperazine-*N'*-2-ethanesulfonic acid (HEPES) and Triton X-100 were obtained from Sigma. All other reagents were analytical grade.

Peptides. FP peptides corresponding to the 23 N-terminal residues (AVGIGALFLGFLGAAGSTMGARS) of the LAV_{1a} strain of HIV-1 gp41 were synthesized as their C-terminal amides using a peptide synthesizer (ABI 431A, Foster City, CA) equipped for Fmoc chemistry. FP was either unlabeled (denoted as "FP") or singly, doubly or triply ¹³C carbonyl or ¹⁵N amide labeled (denoted as "FP-An_{CN}" where "A" and "n" are the one-letter abbreviation and the index of the labeled residue and the subscript indicates whether the carbonyl carbon or amide nitrogen is ¹³C or ¹⁵N labeled). Other FP peptide analogs were synthesized in a similar approach, including FPK3 (AVGIGALFLGFLGAAGSTMGARSKKK) with three-lysine addition at the C-terminus to improve aqueous solubility, FPW (AVGIGALFLGFLGAAGSTMGARSW) with one-tryptophan addition at the C-terminus as a UV/Vis chromophore, and FPK3W

(AVGIGALFLGFLGAAGSTMGARSKKKW) to take advantage of both aspects. The unlabeled and labeled peptides are denoted in the same pattern as the FP peptide. Peptides were cleaved from the resin in a three hour reaction using a mixture of trifluoroacetic acid (TFA):H₂O:phenol:thioanisole:ethanedithiol in a 33:2:2:2:1 volume ratio. Peptides were subsequently purified by reverse-phase HPLC using a preparative C₁₈ column (Vydac, Hesperia, CA) and a water/acetonitrile gradient containing 0.1% TFA. Matrix assisted laser desorption ionization (MALDI) mass spectroscopy was used to demonstrate the success of the synthesis.

Lipid Preparation. Samples were either prepared using single lipids or using a lipid/cholesterol mixture reflecting the approximate lipid and cholesterol content of the HIV-1 virus infected host cells³. Three such mixtures were used: (a) "LM-1" had POPC, POPE, DMPS, and cholesterol in a 10:6:4:10 molar ratio; (b) "LM-2" had POPC, POPE, DMPS, sphingomyelin and cholesterol in a 10:6:4:2:10 molar ratio; (c) "LM-3" had POPC, POPE, POPS, sphingomyelin, PI and cholesterol in a 10:5:2:2:1:10 molar ratio. Lipid and cholesterol powders were dissolved together in chloroform. The chloroform was removed under a stream of nitrogen followed by overnight vacuum pumping. Lipid dispersions were formed by addition of water or buffer containing 0.01% NaN₃ followed by homogenization with ten freeze-thaw cycles. Large Unilamellar Vesicles (LUV) of 100 nm diameter were prepared by extruding the lipid dispersions ~30 times through two stacked 0.1 µm polycarbonate filters⁴ (Avestin, Inc., Ottawa, ON, Canada).

Peptide Aggregation. Peptide aggregation in aqueous solution was estimated from measurements of peptide concentration (by the BCA assay) in solution before and after centrifugation. Centrifugation was either done on a Sorvall RC-5B centrifuge (Newtown,

CT) with a GSA rotor (14,000 × g, 90 minutes) or on a Sorvall Ultra 80 ultracentrifuge (Newtown, CT) with a SW50.1 or SW25.1 rotor (100,000 - 150,000 × g, 120-240 minutes).

Solution NMR Spectroscopy. The NMR measurements were carried out on a Varian INOVA-600 spectrometer at 25 °C. The sample was dissolved in a mixture of 700 µl H₂O/D₂O (6:1 v/v) and acidified with 30 mM HCl solution in some experiments. The strong H₂O proton signal was suppressed by applying the binomial pulse sequence⁵.

Sedimentation Equilibrium. Sedimentation equilibrium experiments were performed at 20 °C on a Beckman XL-I analytical ultracentrifuge using an An-60 Ti rotor. The measurements were carried out using six-channel centerpieces loaded with 110 µl of peptide solution against 110 µl of the buffer. Samples were spun between 5,000 rpm and 52,000 rpm and the 280 nm absorbance was recorded as a function of the centrifugal radius. For each speed, data were collected three times at every 4 h and the profiles at the 8th and 12th hours were identical, confirming that equilibrium had been reached. Multiple records at different speed were subjected to the non-linear regression analysis using the software from Beckman/MicroCal to obtain the best fit for the molecular weight (M) of the solute by equation (1):

$$A_r = A_0 \exp[M \times (1 - \underline{v}\rho) \times (r^2 - r_0^2) \times (\omega^2 / 2RT)] \quad (1)$$

where A_r and A_0 are the absorbance at radius r and at the reference radius r_0 , \underline{v} is the partial specific volume, ρ is the buffer density, ω is the angular velocity, R is the gas constant, and T is the temperature.

Circular Dichroism (CD) Spectroscopy. CD spectra were recorded on a JASCO J810 spectropolarimeter (Tokyo, Japan) at 20 °C using a quartz optical cell with a 10 mm

pathlength. The spectra were recorded from 190 nm to 250 nm at a scanning rate of 100 nm/min with a step resolution of 0.1 nm and bandwidth of 1 nm. Each set of CD data was obtained from an average of eight scans. Samples were dissolved in water or 5 mM HEPES (pH 7.0). The observed ellipticity (θ) was converted to mean residue ellipticity $[\theta]$ to allow direct comparison among peptides by the following equation:

$$[\theta] = \theta / (l \times c \times N) \quad (2)$$

where l is the cell length in mm, c is the molar concentration of the sample, and N is the number of amino acid residues in the peptide.

Lipid Mixing Assay for Membrane Fusion. The resonance energy transfer assay of Struck, *et al.* was used to monitor membrane fusion⁶. Two types of LUV's were prepared. One set contained 2 mole percent of the fluorescent lipid *N*-NBD-PE and 2 mole percent of the quenching lipid *N*-Rh-PE while the other set contained only the unlabeled lipids. Fluorescently labeled and unlabeled vesicles were mixed in a 1:9 ratio. Following addition of the peptide, lipid mixing between labeled and unlabeled vesicles caused dilution of the labeled lipids with a resulting increase of fluorescence. Fluorescence was recorded using 4 nm bandwidth on a Instruments S. A. Fluoromax-2 spectrofluorimeter operating at excitation and emission wavelengths of 465 nm and 530 nm, respectively. A siliconized glass cuvette was used with continuous stirring in a thermostated cuvette holder. Measurements were carried out at 37 °C with 2 ml of 150 μ M LUV in 5 mM HEPES (pH 7.0). A small quantity of peptide solution was added to achieve the desired peptide:lipid molar ratio, and the fluorescence of the sample (F_t) was monitored as a function of time following this addition. The initial residual fluorescence intensity was recorded as F_0 . The maximum fluorescence intensity, F_{max} , was obtained following

addition of 20 μ l of 10% Triton X-100. F_t and F_{\max} were corrected for the small fluorophore dilution resulting from the added volumes of peptide and Triton X-100. Percent lipid mixing at time t (M_t) was given by $[(F_t - F_o)/(F_{\max} - F_o)] \times 100\%$. With sufficient time, M_t reaches a constant value which is denoted as M_f , the final extent of lipid mixing. For a given set of labeled and unlabeled vesicles, M_f had $\pm 2\%$ reproducibility between different assay trials. In this study, M_f is used as a measure of peptide fusogenicity.

Leakage Studies. Aqueous content leakage from liposomes was monitored by the ANTS/DPX assay⁷. LUV was prepared in 5 mM HEPES (pH 7.0) solutions which contained the fluorescent molecule ANTS and quenching molecule DPX at 12.5 mM and 45 mM, respectively. ANTS and DPX were then removed from the extravesicular medium by dialysis against 65 mM HEPES solution. After addition of a small quantity of peptide solution to achieve the desired peptide:lipid molar ratio, vesicle leakage was monitored by the increase in ANTS fluorescence. Fluorescence measurements were performed at excitation and emission wavelengths of 355 nm and 520 nm, respectively. Measurements were made at 37 °C using 2 ml of 80 μ M LUV in 65 mM HEPES (pH 7.0). Percent leakage was defined in the same way as was used for the lipid mixing assay.

RESULTS AND DISCUSSION

Peptide Aggregation in Aqueous Solution. Fusion peptide has been studied in aqueous solution at acidic condition⁸. However, in neutral pH PBS or saline buffered D₂O where the fusion of HIV virion takes place, at least two groups has reported the formation of large fibrillar fusion peptide aggregates by electron microscopy^{9,10}.

Furthermore, the fusion activity of the peptide was significantly reduced due to the aggregation¹⁰. To alleviate this problem, fusion peptide was often prepared in an organic solvent such as dimethyl sulfoxide (DMSO) or trifluoroethanol and then transferred into the aqueous media for further studies. Although control experiments generally showed that the organic solvent by itself did not cause fusion in the functional assays, it was not clear whether the peptide molecules collide and form aggregates before they bind to membranes. In order to find non-aggregating conditions without introducing organic component into the sample environment, we carried out a systematic investigation on wild type 23-residue FP peptide in the absence of membrane.

Soluble peptide was separated from aggregated peptide through centrifugation. The concentration of the soluble peptide was measured using the highly sensitive Micro BCA protein assay. Results from these studies are presented in Table 1, with uncertainties of $\pm 10\%$ in the peptide concentration measurements. In unbuffered solution, the fusion peptide formed a clear solution, even at mM concentrations. After addition of phosphate buffer or NaCl, the solution became cloudy. Formation of large aggregates was confirmed by significant loss of peptide concentration after centrifugation. Large aggregates were not formed in 100 mM acetate buffer pH 4.5 or in 5 mM HEPES buffer pH 7.0. Thus, there appear to be pH and ionic strength effects on aggregation. The differences in aggregation between HEPES and phosphate or NaCl may be a result of the differences in their molecular sizes. Based on these results, most solid-state NMR samples were made using 15 – 150 μM peptide concentration in 5 mM pH 7.0 HEPES buffer, which is close to the physiological pH of 7.4 for HIV-1/host cell fusion. Although physiological solutions contain ~ 140 mM NaCl, it was omitted from the

sample preparation because it causes aggregation. It would be possible to add NaCl after the peptide has bound to the membrane.

A more soluble fusion peptide construct was introduced based on the study of influenza fusion peptide by Tamm and coworkers. In this study, addition of a lysine-rich “host sequence” at the C-terminus of the peptide greatly improves the peptide solubility in aqueous solution¹¹. For some of our studies, a similar modification was made for the HIV-1 fusion peptide (FPK3 and FPK3W).

The oligomerization of viral envelope proteins is well known and there is some evidence that fusion peptide oligomerization is a structural requirement for membrane fusion¹². Fusion peptide oligomers might be pre-formed in solution and bind as a unit to the membrane or oligomers might only form during interaction with the membrane. Using a simplified model for ultracentrifugation, our data for the 15 μ M peptide concentration in 5 mM pH 7.0 HEPES demonstrate that the solution contains no more than ~900 FP molecules in any aggregate¹³.

Table 1. FP Peptide Aggregation in Different Aqueous Buffer Solutions.

Initial Conc. (μM)	Solution Conditions	% Soluble Peptide ^{a,b}
6200	Unbuffered H ₂ O	90
210	100 mM acetate, pH 4.5	>90
1300	5 mM HEPES, pH 7.0	88
1100	5 mM HEPES, pH 7.0, sitting for 2 days	80
15	5 mM HEPES, pH 7.0, sitting for 1 day	>90
30	10 mM phosphate, pH 7.0	16
22	10 mM phosphate, pH 6.0	60
1100	5 mM HEPES, pH 7.0, 20 mM NaCl	18

^a In rows 1-4 and 6-9, the concentration was measured after centrifugation at $14,000 \times g$ for 90 min. In row 5, the concentration was measured after centrifugation at $100,000 \times g$ for 120 min.

^b Estimated error: $\pm 10\%$.

Solution NMR linewidths also provide some information about aggregate size. At all pH, there is a molecular tumbling contribution to the observed linewidth that is proportional to molecular weight¹⁴. Figure 3 displays the amide region of the 600 MHz solution ¹H NMR spectra of 80 μM FP and FPK3 solution at acidic and neutral pH. The narrowest linewidths for the neutral pH FP and FPK3 spectra are ~ 16 Hz, which correspond to ~ 25 KD molecular weight or ~ 10 -12 peptide molecules. In these neutral pH spectra, signals from individual amide proton are not completely resolved and it is possible that the true linewidths and oligomer sizes are less than these estimates. In addition, in the amide region, exchange with the solvent may broaden the observed lines¹⁵. The exchange rate is significantly reduced at lower pH, which is consistent with

the observation of narrower linewidths of ~ 5 Hz in both spectra at pH 3.7. This linewidth is consistent with a monomer or oligomer of two or three molecules. Since both fusion peptide sequences have no acidic residues and their C-termini are amidated, they should have similar type of charge in both pHs and it's not clear that lower pH should alter oligomerization. The exchange rate at different pH is likely the reason of different linewidths. Further study to observe the linewidth of non-exchangeable C α protons at different pHs would give a better understanding of the oligomerization dependence on pH change.

A better way to estimate the molecular weight of solute in solution is through the sedimentation equilibrium experiment by analytical ultracentrifugation. In the experiment, when sedimentation and diffusion come to equilibrium, no apparent movement of solute occurs and its molecular weight can be derived from the equilibrium concentration distribution¹⁶. Because of background absorbance at 220 nm from the buffer, the initial experiments with 50 μ M of both FP and FPK3 peptide in unbuffered water or under acidic conditions did not provide useful information, so we added a Trp residue at the C-terminus of the peptide to introduce a chromophore that allowed us to measure absorbance at 280 nm with less interference. Figure 4a displays the results of the sedimentation equilibrium experiment at 20 °C for a sample made with 80 μ M FPK3W peptide in 5 mM HEPES pH 7 buffer. A total of 4 such data sets at both 45,000 and 52,000 rpm were included into the data analysis. Each data set gave random variations of the residuals similar to the one shown, which indicates that the global fit matched the model for a single species. With a partial specific volume of 0.763 ml/g that was calculated by the method of Durschschlag¹⁷ and a solvent density of 1.0 g/ml, the optimal

fit to all 4 data sets, determined by a non-linear least-squares method, was a molecular weight of 2610 (2570 – 2650), where the values in parentheses are the 95% confidence limits from this fitting routine. Since the molar mass of the FPK3W peptide is ~2690, this result indicates that the peptide is a monomer in the buffer. The experiments were repeated in another instrument and a similar result was obtained, showing that the FPK3W peptide is truly a monomeric peptide in the buffer.

Figure 4b displays the data with 80 μ M FPW peptide in the buffer solution. Peptide pellets were observed at speed above 15,000 rpm, so the displayed data were obtained at 5,000 rpm. A mean value of $M \sim 230,000$ was estimated from the fitting which corresponds to ~ 100 peptide molecules. However, the experimental data has substantial curvature, which indicates that there is a significant distribution of oligomer sizes.

In terms of their overall solubility and the rates with which they dissolve in buffer, the peptides can be ordered $FPW < FP < FPK3W, FPK3$. This order together with the sedimentation equilibrium data and previous linewidth analysis in solution NMR experiments suggest that FPW is predominantly associated as large oligomers, and FP is mainly associated as small oligomers. Because FPK3 contains the same number of charged residues as FPK3W, we expect that FPK3 is the same as FPK3W and is predominantly a monomer in the buffer solution.

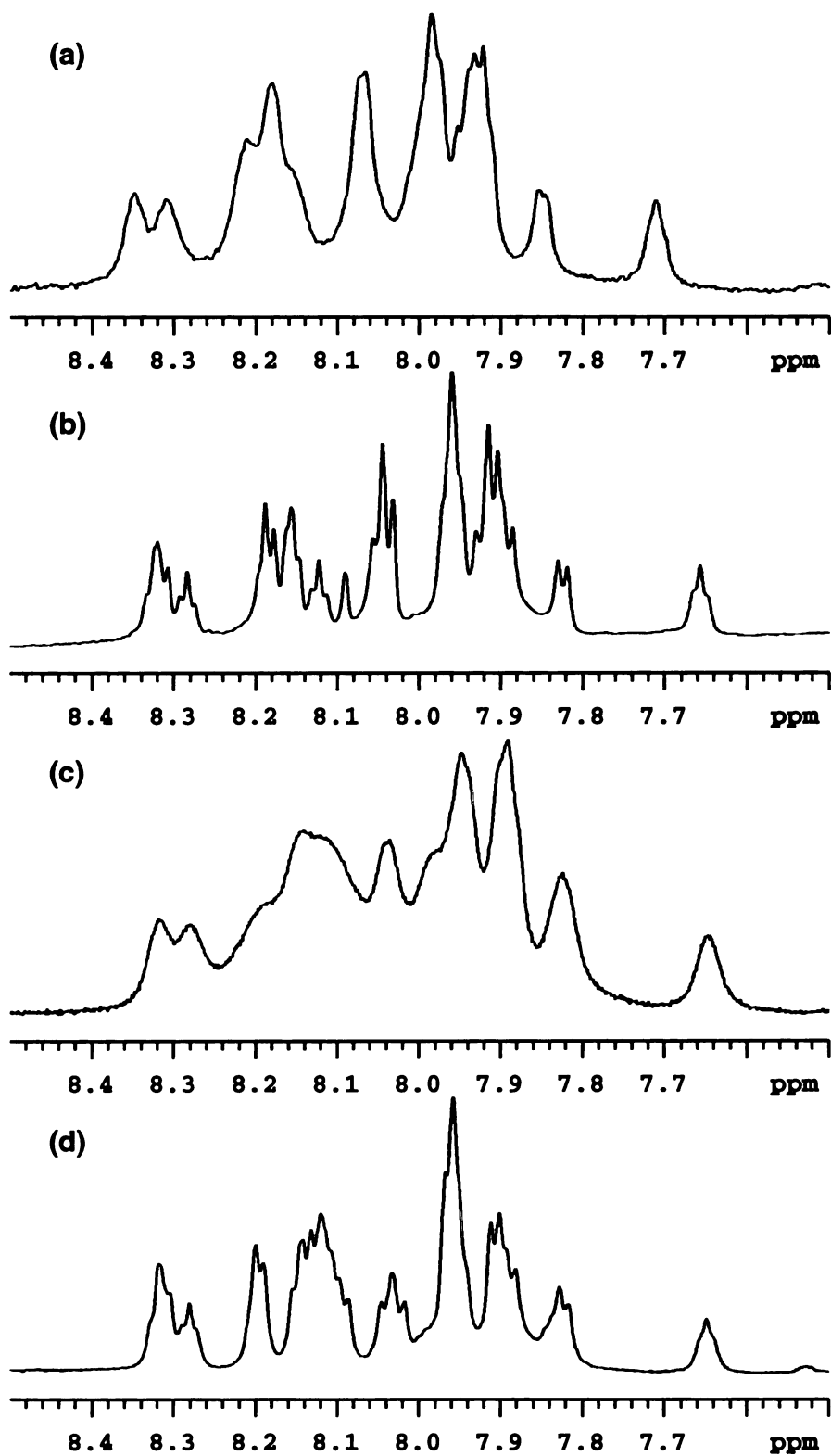


Figure 3. Solution amide ^1H NMR spectra of (a) FP at pH 6.7, (b) FP at pH 3.7, (c) FPK3 at pH 6.4, and (d) FPK3 at pH 3.7.

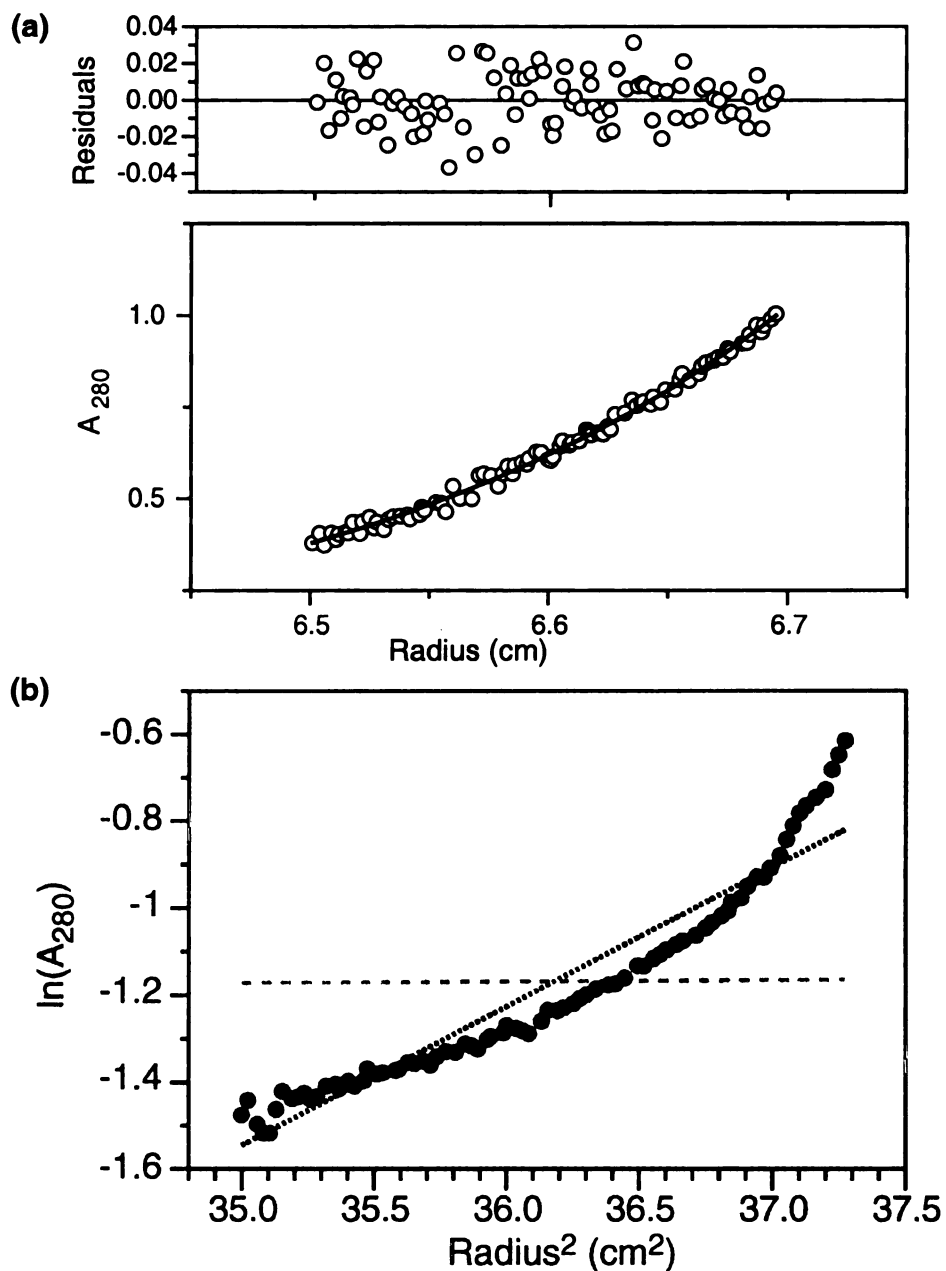


Figure 4. Sedimentation equilibrium experiments of (a) 80 μM FPK3W and (b) 80 μM FPW in buffer. In (a), the main panel shows the absorbance at 280 nm as a function of the centrifugal radius after reaching the equilibrium in 20 hours at 52,000 rpm. The best fit to the model for a single species was obtained with a molecular weight of ~ 2630 (shown as a solid line through the experimental points). The upper panel shows the residuals between the data and the fit. In (b), the logarithm of 280 nm absorbance is plotted as a function of $(\text{radius})^2$ at 5,000 rpm. The data are represented as dark circles and the dark dotted and light-dashed lines represent the expected results for FPW 100-mers and monomers, respectively.

Peptide Overall Structure in Solution. The overall secondary structures of the peptides prior to associating with membrane were evaluated from their CD spectra. Figure 5 displays the results of four 20 μM fusion peptide constructs in water and 5 mM HEPES pH 7 buffer. In unbuffered water, both FP and FPK3 peptides form random coil structures as indicated by their characteristic negative molar ellipticity at wavelengths below 210 nm¹⁸. The results of FPW and FPK3W peptides are less clear and may be a mixture of several different secondary structures. In 5 mM HEPES buffer, the CD spectra of all four peptides change to more or less the same shape except for their intensities. Also there is greater noise in the spectra. Efforts to deconvolute each spectrum into individual secondary structure components (i.e. α -helix, β -sheet, random coil, etc.) were not successful, which may indicate that there is no overall secondary structure through the entire peptide.

Since we observed a better-resolved solution NMR spectrum at low pH, we also examined whether low pH also leads to a better structure elucidation. A series of FP peptide CD spectra at different pH were obtained by gradually adding small amount of 30 mM HCl solution into the unbuffered 20 μM solution. Figure 6 shows the result and demonstrates that the overall structure is insensitive to changes in pH to 3.1.

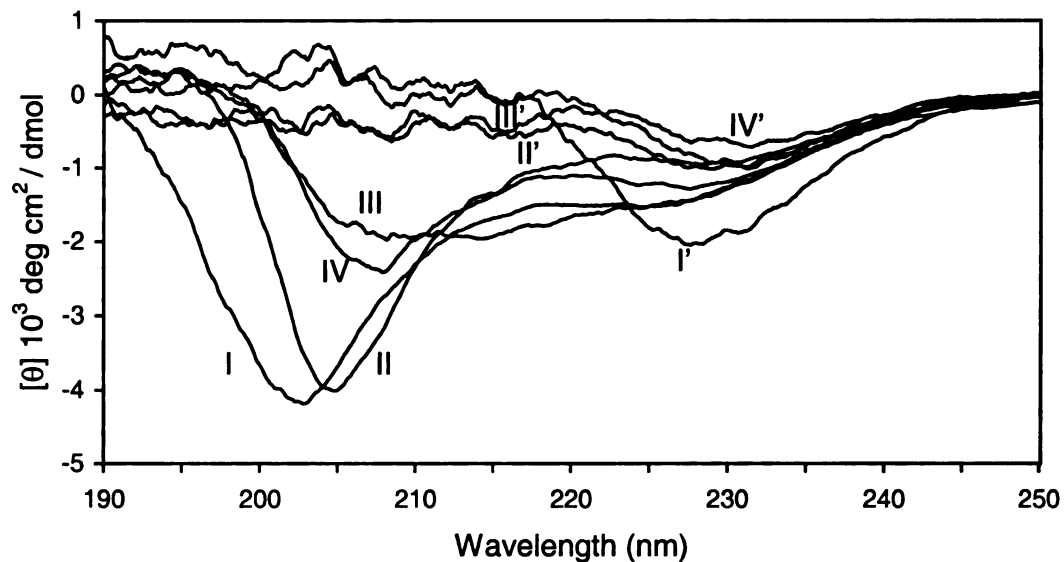


Figure 5. CD spectra of four 20 μM fusion peptide constructs in unbuffered water: FP (I), FPK3 (II), FPW (III), and FPK3W (IV); and in 5 mM HEPES buffer: FP (I'), FPK3 (II'), FPW (III'), and FPK3W (IV').

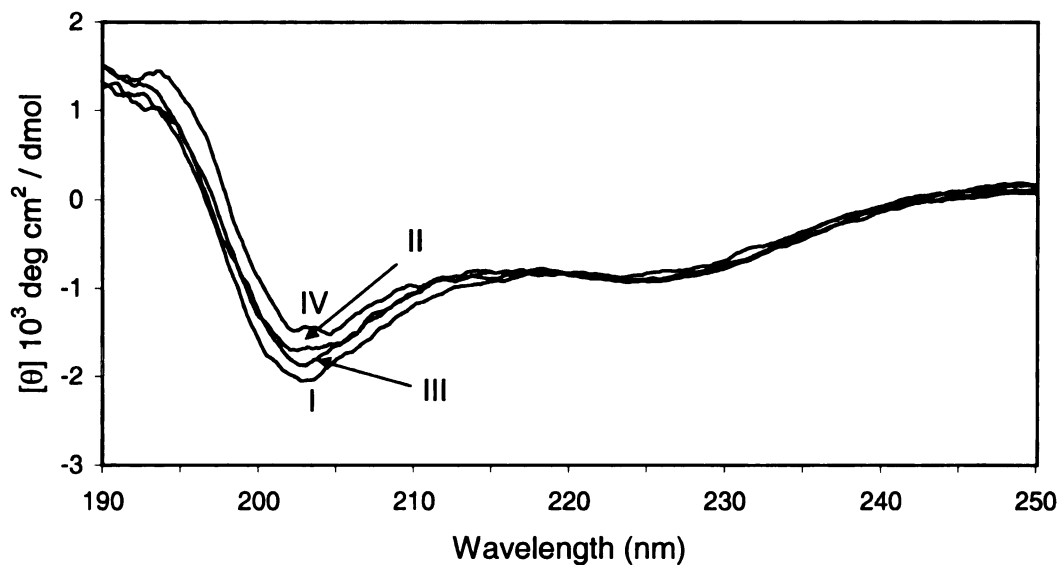
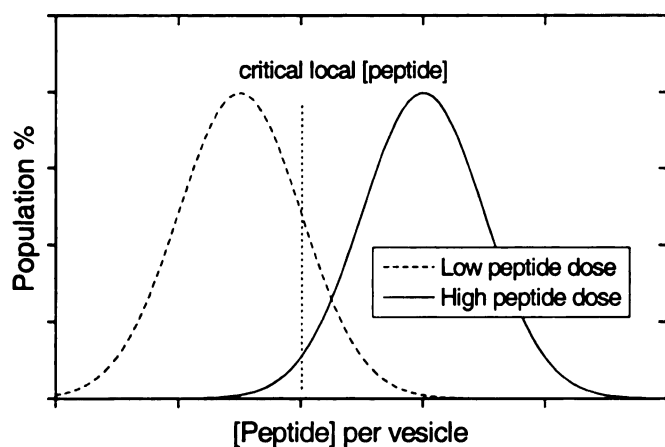


Figure 6. CD spectra of 20 μM FP peptide in unbuffered water (I), and a series of acidified water solutions at pH 5.0 (II), pH 4.1 (III), and pH 3.1 (IV). The pH is adjusted by adding a small amount of 30 mM HCl solution.

Peptide-Induced Fusion of LM Vesicles. In order to test whether the peptide is fusogenic, measurements were first made on the FP peptide-induced lipid mixing between vesicles, and aqueous contents leakage from vesicles. Figure 7 demonstrates both effects and gives results comparable to those obtained by other investigators^{10, 19}. At low peptide:lipid molar ratios ($\leq 1:80$), lipid mixing and leakage only proceed to $\sim 10\%$ of their maximal values. At a peptide:lipid molar ratio of 1:20, fusion and leakage are much more efficient, which suggests that a vesicle's fusogenicity is related to the number of incorporated peptide molecules. This is consistent with the "all-or-none" hypothesis that fusion requires a critical number of fusion peptides per vesicle²⁰. A model is demonstrated below and a normal distribution of the number of peptide molecules per vesicle is assumed. According to the hypothesis, only those vesicles that have the same



number or more than the critical number of peptide per vesicle (the dotted line) would promote fusion; i.e., the amount of fusion is proportional to the area to the right of the dotted line. At low peptide dose, this area is rather

small; at high peptide dose, the area increases significantly and significantly more fusion will be observed. This hypothesis also predicts that at constant peptide:lipid molar ratio, fusion will be greater for larger vesicles because the population of vesicles that have the required number of fusion peptides increases with larger vesicle size. However, we observed that at low peptide:lipid molar ratios, the percentage of lipid mixing is

independent of vesicle size between 100 nm and 400 nm. This result suggests that instead of local number, it may be the local concentration of membrane-associated peptide which is the critical factor. This concentration is constant with respect to vesicle size.

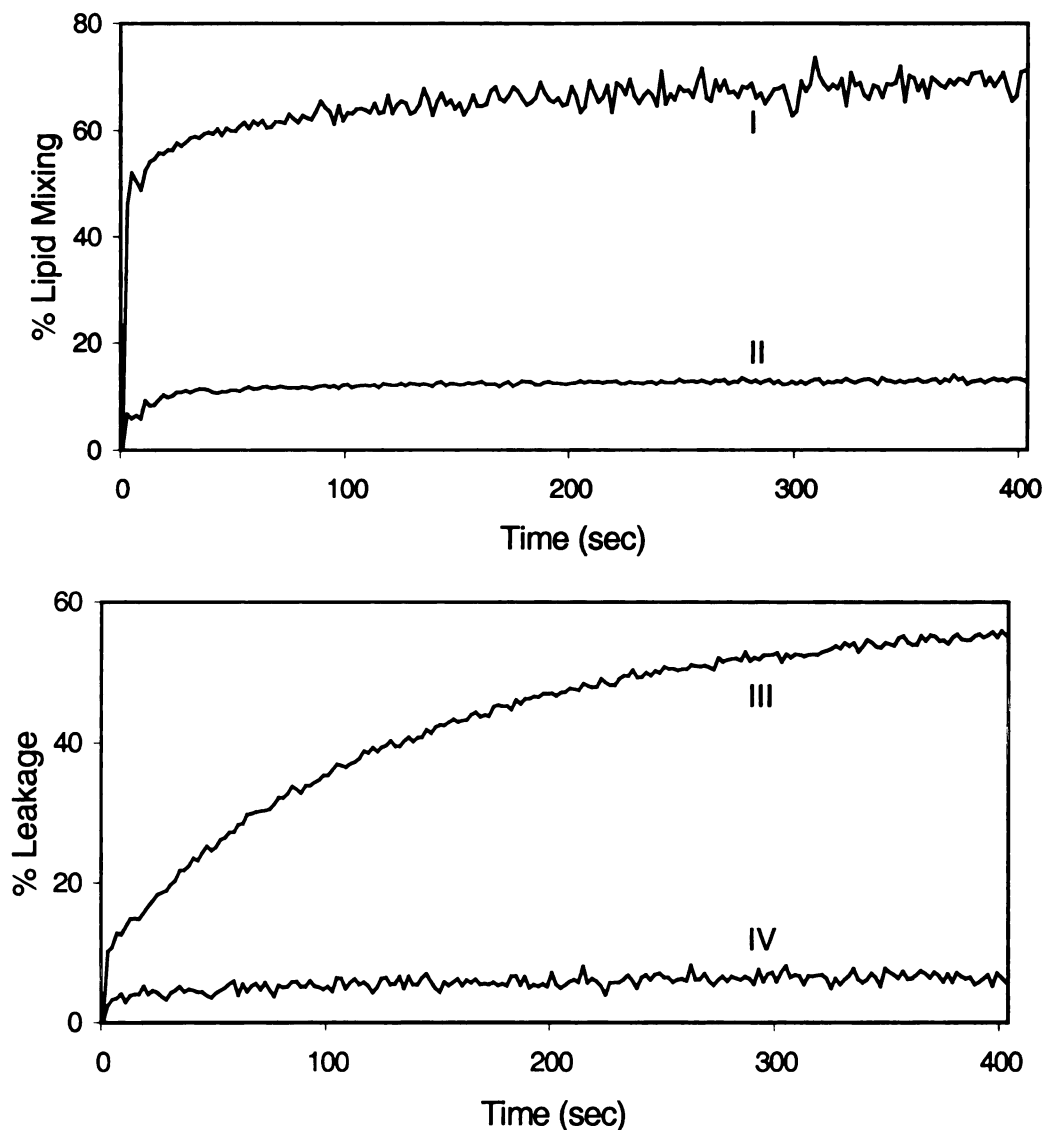


Figure 7. FP-induced lipid mixing (top) and FP-promoted aqueous contents leakage (bottom) as observed by fluorescence assays at 37 °C. For the lipid-mixing assay, 150 μM LM-3 lipid was extruded into 100 nm diameter vesicles. Lipid mixing was induced with (I) 7.5 μM and (II) 1.5 μM FP. For the aqueous contents leakage assay, 80 μM LM-3 lipid was extruded into 100 nm diameter vesicles loaded with ANTS/DPX. Leakage was promoted by FP at (III) 4 μM and (IV) 1 μM concentrations.

Lipid mixing assays were also carried out to assess the fusogenicities of the four fusion peptide constructs. Figure 8 displays plots of M_t vs. time for each of the constructs with peptide:lipid molar ratios of 1:100 and 1:50. All peptides induce significant lipid mixing. At a peptide:lipid molar ratio of 1:100, the ordering of M_f values for the different peptides is $FPW < FPK3$, $FPK3W < FP$ while at a peptide:lipid molar ratio of 1:50, the ordering is $FPW < FPK3W < FP$, $FPK3$. Overall, FPW appears to be the least fusogenic while FP is the most fusogenic. As discussed in peptide aggregation section, the likely solution oligomerization states of the peptides are: $FPK3W$, $FPK3$ - monomeric; FP - mixture of small and large oligomers; and FPW - large oligomers. Thus, there does not appear to be a linear relationship between solution oligomerization state and fusogenicity, although it may be that small oligomers (FP) promote lipid mixing more efficiently than monomers ($FPK3W$, $FPK3$) or large oligomers (FPW).

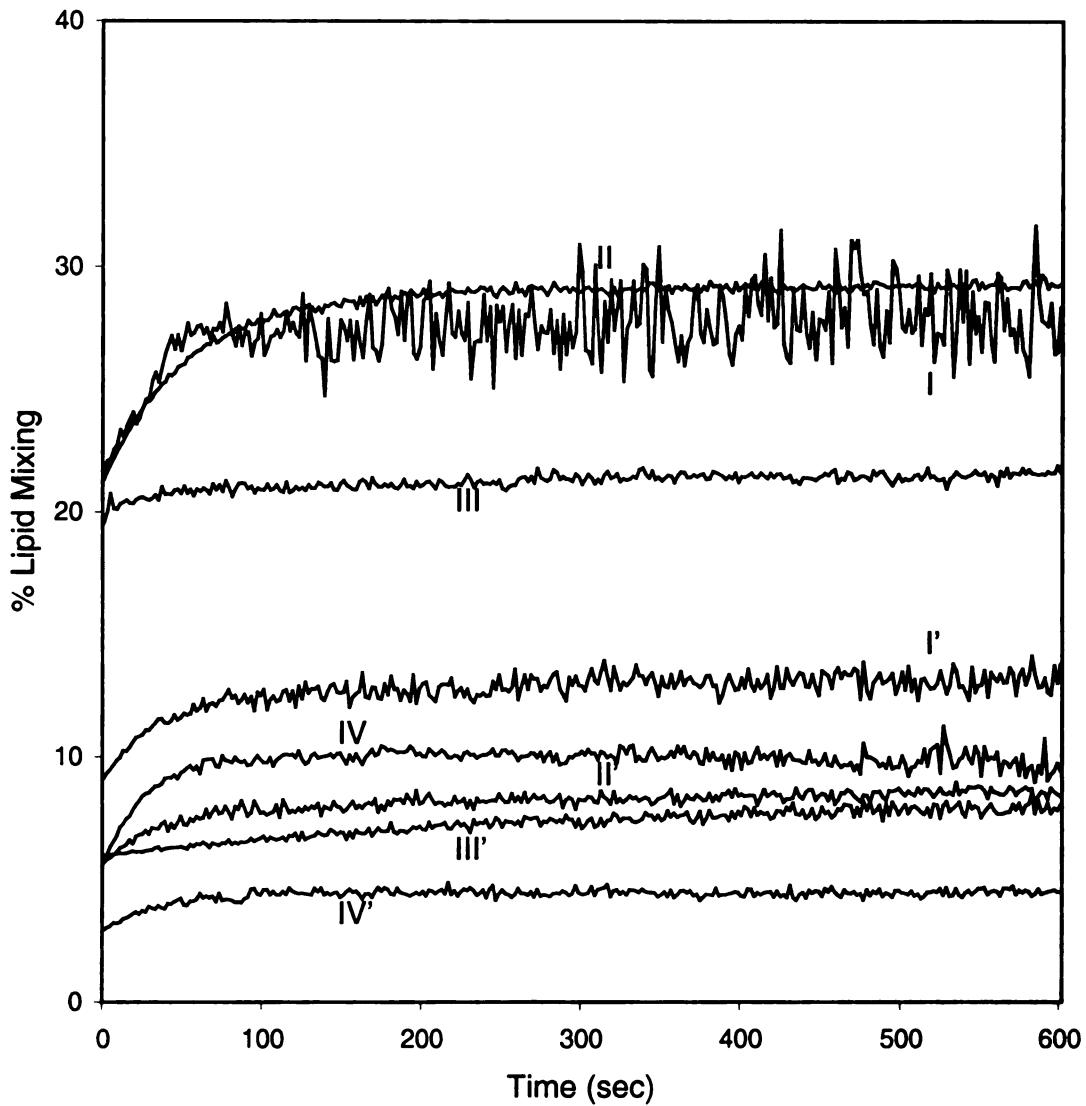


Figure 8. Lipid mixing induced by four fusion peptide constructs. In the assay, 150 μM LM3 was extruded into 100 nm diameter vesicles and mixing was induced by (I) 3 μM and (I') 1.5 μM FP; (II) 3 μM and (II') 1.5 μM FPK3; (III) 3 μM and (III') 1.5 μM FPK3W; and (IV) 3 μM and (IV') 1.5 μM FPW.

CONCLUSION

The fusion peptide is derived from the fusogenic region of the HIV-1 viral envelope protein gp41. Numerous studies have shown that the free peptide has an integral role in the fusion process. Hence the study of the free fusion peptide provides a good model to understand the mechanism of HIV-1 viral fusion with the host cells.

Before we investigate the peptide structure in the membrane environment using solid-state NMR, we need to ensure that the system that we examine is biologically relevant. This is important because the conflicting structural results of fusion peptide studies from other groups suggest that the sample preparation may have a significant effect on the experimental observations. In this study, we conducted a series of experiments to verify the validity of our measurements.

The oligomerization of fusion peptide in aqueous solution was the first issue we considered. There was evidence that in neutral pH phosphate buffer the peptide forms large fibrillar aggregates that reduce the fusion activity. After testing a series neutral buffer solutions, we found that 5 mM HEPES buffer at pH 7 was a good choice since >90% of peptide was soluble at the concentration used for solid-state NMR samples. Later, a more soluble construct was utilized by adding a lysine-rich “host sequence” at the C-terminus of the peptide. The oligomerization status of the peptides was estimated by solution NMR and sedimentation equilibrium experiments. The results show that most of the fusion peptide constructs are monomeric or form small oligomers of 10 ~ 20 molecules, except for FPW which forms oligomers over 100 molecules. CD measurements suggest that there is no global structure for the entire peptide in the absence of membrane.

The fusion activity of the peptide was the next issue we examined. The results of FP-induced lipid-mixing and aqueous contents leakage assays were comparable to those obtained by other investigators. We also compared the fusogenicities among the four fusion peptide constructs. While FP, FPK3 and FPK3W have about the same fusion activity, there was significantly less lipid mixing induced by FPW peptide. Considering the sizes of the peptides in solution, FPK3W and FPK3 are monomeric, FP forms small oligomers, and FPW forms large oligomers, there is not a linear relationship between the solution oligomerization state and fusogenicity, although it appears that the small oligomers (FP) promote lipid mixing more efficiently than monomers (FPK3, FPK3W) or large oligomers (FPW).

In summary, a series of experiments confirm that we can prepare and examine biologically relevant samples and that the peptide structure we obtain should reflect at least the final stage of the fusion process.

REFERENCE

1. Chang, C. D., Waki, M., Ahmad, M., Meienhofer, J., Lundell, E. O., and Haug, J. D. (1980) Preparation and properties of N-9-fluorenylmethyloxycarbonylamino acids bearing tert-Butyl side chain protection. *Int. J. Pept. Protein Res.* 15, 59-66.
2. Lapatsanis, L., Miliadis, G., Froussios, K., and Kolovos, M. (1983) Synthesis of N-2,2,2-(trichloroethoxycarbonyl)-L-amino acids and N-(9-fluorenylmethoxycarbonyl)-L-amino acids involving succinimidoxycarboxylate anion as a leaving group in amino-acid protection. *Synthesis* 8, 671-673.
3. Aloia, R. C., Tian, H., and Jensen, F. C. (1993) Lipid composition and fluidity of the human immunodeficiency virus envelope and host cell plasma membranes. *Proc Natl Acad Sci U S A* 90, 5181-5185.
4. Hope, M. J., Bally, M. B., Webb, G., and Cullis, P. R. (1985) Production of large unilamellar vesicles by a rapid extrusion procedure - characterization of size distribution, trapped volume and ability to maintain a membrane-potential. *Biochim. Biophys. Acta* 812, 55-65.
5. Hore, P. J. (1983) Solvent suppression in fourier-transform nuclear magnetic resonance. *J. Magn. Reson.* 55, 283-300.
6. Struck, D. K., Hoekstra, D., and Pagano, R. E. (1981) Use of resonance energy transfer to monitor membrane fusion. *Biochemistry* 20, 4093-4099.
7. Ellens, H., Bentz, J., and Szoka, F. C. (1985) H⁺- and Ca²⁺-induced fusion and destabilization of liposomes. *Biochemistry* 24, 3099-3106.
8. Chang, D. K., Chien, W. J., and Cheng, S. F. (1997) The FLG motif in the N-terminal region of glucoprotein 41 of human immunodeficiency virus type 1 adopts a type-I beta turn in aqueous solution and serves as the initiation site for helix formation. *Eur J Biochem* 247, 896-905.
9. Slepishkin, V. A., Andreev, S. M., Sidorova, M. V., Melikyan, G. B., Grigoriev, V. B., Chumakov, V. M., Grinfeldt, A. E., Manukyan, R. A., and Karamov, E. V. (1992) Investigation of human immunodeficiency virus fusion peptides. Analysis of interrelations between their structure and function. *AIDS Res Hum Retroviruses* 8, 9-18.
10. Pereira, F. B., Goni, F. M., Muga, A., and Nieva, J. L. (1997) Permeabilization and fusion of uncharged lipid vesicles induced by the HIV-1 fusion peptide adopting an extended conformation: dose and sequence effects. *Biophys. J.* 73, 1977-1986.

11. Han, X., and Tamm, L. K. (2000) A host-guest system to study structure-function relationships of membrane fusion peptides. *Proc. Natl. Acad. Sci. U. S. A.* 97, 13097-13102.
12. Kliger, Y., Aharoni, A., Rapaport, D., Jones, P., Blumenthal, R., and Shai, Y. (1997) Fusion peptides derived from the HIV type 1 glycoprotein 41 associate within phospholipid membranes and inhibit cell-cell Fusion. Structure- function study. *J. Biol. Chem.* 272, 13496-13505.
13. Yang, J., Gabrys, C. M., and Weliky, D. P. (2001) Solid-state nuclear magnetic resonance evidence for an extended beta strand conformation of the membrane-bound HIV-1 fusion peptide. *Biochemistry* 40, 8126-8137.
14. Cavanaugh, J., Fairbrother, W. J., Palmer, A. G., and Skelton, N. J. (1996) *Protein NMR Spectroscopy Principles and Practice*, Academic Press, San Diego.
15. Connelly, G. P., Bai, Y., Jeng, M. F., and Englander, S. W. (1993) Isotope effects in peptide group hydrogen exchange. *Proteins: Struct. Funct. Genet.* 17, 87-92.
16. Bowen, T. J. (1970) *An Introduction To Ultracentrifugation*, John Wiley and Son, London.
17. Durschschlag, H. (1986) *Specific volumes of biological macromolecules and some other molecules of biological interest*, Springer-Verlag, Berlin.
18. Cantor, C. R., and Shimmel, P. R. (1980) *Biophysical Chemistry*, W. H. Freeman, New York.
19. Peisajovich, S. G., Epanand, R. F., Pritsker, M., Shai, Y., and Epanand, R. M. (2000) The polar region consecutive to the HIV fusion peptide participates in membrane fusion. *Biochemistry* 39, 1826-1833.
20. Nieva, J. L., Nir, S., and Wilschut, J. (1998) Destabilization and fusion of zwitterionic large unilamellar lipid vesicles induced by a beta-type structure of the HIV-1 fusion peptide. *J. Liposome Res.* 8, 165-182.

CHAPTER III

CONFORMATIONAL STUDIES OF THE MEMBRANE-ASSOCIATED FUSION PEPTIDE BY SOLID-STATE ONE-DIMENTIONAL NMR MEASUREMENTS

BACKGROUND

For biophysical studies, including solid state NMR spectroscopy, it is often easier to work with smaller systems than the full envelope proteins. In this project, we work with peptides containing the ~ 20-residue N-terminal fusion peptide domain of the gp41 envelope protein. There is body of biochemical and biophysical evidence which demonstrate that the free ~ 20-residue fusion peptide by itself has biological relevance in a similar manner as the intact protein, and therefore provides important information about the mechanism of viral envelope protein induced membrane fusion.

In the previous chapter, we examined the biological activity of the synthetic fusion peptide. In this chapter, we first verified that the structure we would probed with solid-state NMR techniques is indeed the membrane-associated structure. Furthermore, since we prepared our sample in the similar way as we conducted the fusion assay, the structure probed would also represent the one at least at the end stage of fusion.

Because of the low natural abundance of interesting nuclei such as ^{13}C and ^{15}N , we generally need specific isotopic labeling to obtain adequate signal-to-noise. Isotopic labeling is in fact advantageous because the signals from the isotopic labels dominate the spectrum and allow us to focus on the structure in the vicinity of the labeled nuclei, which makes solid-state NMR a powerful structural approach for residue-specific structural studies.

It is well known that the useful information contained in an NMR spectrum comes from the different local field experienced by each nuclear spin. In solution NMR, because of the rapid molecular tumbling, the nucleus experiences a homogenous local field and a very sharp peak is observed. In solid state, this molecular tumbling is significantly

slower, and the orientation dependence is not averaged out. The local field is dominated by the chemical shift anisotropy (CSA) and by the dipole-dipole coupling between spatial-nearby nuclei. The CSA is the dependence of chemical shift on the relative orientation between the functional group and the external magnetic field. These two factors will significantly broaden the linewidth. Fortunately, we can apply magic angle spinning (MAS) to improve the resolution by spinning the sample about an axis tilted at 54.7° relative to the external magnetic field direction. As a result, instead of a broad peak, the spectrum will contain a much narrower isotropic peak and a series of spinning sidebands separated by the spinning frequency. By examining the linewidth and chemical shift of the isotropic peak, we can obtain information about the structural heterogeneity and the secondary structure near the labeled nuclei in the peptide.

METHODS

Solid-State NMR Sample Preparation. Samples were typically prepared using 0.01% (w/v) NaN_3 in either unbuffered water or 5 mM HEPES buffer (pH 7.0). Samples were prepared by three different methods. Method 1: Mixtures of peptide (15 - 150 μM) and either a lipid dispersion or vesicles (1 - 30 mM) in 4 ml or 30 ml total volume were kept at room temperature overnight to ensure maximum peptide/lipid binding. Subsequent centrifugation of the peptide/lipid complex, typically at 100,000 - 150,000 \times g for two to four hours, pelleted down the complex and left unbound peptide in the supernatant. The peptide/lipid pellet formed after ultracentrifugation was transferred by spatula to a 7 mm or 6 mm diameter MAS NMR rotor. Method 2: Mixtures of peptide (1 - 10 mM) and lipid dispersion (200 - 400 mM) were mixed to form ~ 200 μl total

volume. The mixtures were transferred directly to the MAS rotor. Method 3: Peptide and lipid were codissolved in 6 ml mixture of chloroform:trifluoroethanol:hexafluoropropanol (3:2:2 v/v). The solvent was removed under a stream of nitrogen and dried in vacuum overnight. The mixture of peptide and lipid was then hydrated with 5 mM pH 7.0 HEPES buffer followed by homogenization with ten freeze-thaw cycles. The sample was diluted with buffer to ~ 35 ml total volume and kept at room temperature overnight. Subsequent centrifugation of the peptide/lipid complex at $100,000 \times g$ for four hours pelleted down the complex and left unbound peptide in the supernatant. The peptide/lipid pellet formed after ultracentrifugation was transferred by spatula to a 6 mm diameter MAS rotor.

Measurement of Peptide/Lipid Binding. For solid-state NMR preparation method 1, peptide/lipid binding was determined through BCA assay of the peptide solution prior to addition of lipid and after ultracentrifugation. After ultracentrifugation, all lipid was pelleted and there was no interference from unpelleted lipid in the BCA assay. Controls were run with peptide-only samples to ensure that the peptide alone did not pellet.

For solid-state NMR preparation method 2, ~ 800 μ l water was added to the peptide/lipid dispersion, the sample vortexed, and the peptide/lipid mixtures were spun down at $10,000 - 14,000 \times g$. The unbound peptide concentration in the supernatant was measured by BCA assay. Under these centrifugation conditions, the entire lipid was pelleted, and there was no interference from unpelleted lipid in the BCA assay.

One-Dimensional (1D) Solid-State NMR Experiments. Measurements were made on two 9.4 T spectrometers, Varian VXR and Varian Infinity Plus (Palo Alto, CA). For the Varian VXR spectrometer, a double resonance MAS probe was used with 7 mm diameter rotors. The NMR detection channel was tuned to ^{13}C and the decoupling

channel was tuned to ^1H . Experiments were carried out using a spinning speed between 3.5 and 4.0 kHz. Application of 1 ms of cross-polarization (CP) at 47 kHz was followed by signal detection with decoupling at 75 kHz. The recycle delay was 0.5 s. For typical samples containing $\sim 0.5 \mu\text{mole}$ of labeled peptide, a single spectrum was the average of 80,000 - 160,000 scans. All chemical shifts were externally referenced to the methylene carbon resonance of adamantane (38.2 ppm). Spectra were processed with 25 Hz line broadening and all refer to the isotropic carbonyl regions.

Samples were cooled to $-50 \text{ }^\circ\text{C}$ either slowly in the NMR probe or by fast freezing in liquid nitrogen. Both freezing techniques gave comparable spectra. Although physiological fusion occurs at $37 \text{ }^\circ\text{C}$, we chose this low temperature because relative to room temperature, there is about three times greater signal per ^{13}C at the lower temperature. This is likely due in part to more efficient cross-polarization (CP) because of reduced motion at lower temperature. ^{13}C backbone chemical shifts were similar at both temperatures which suggests that cooling the sample does not cause significant peptide structural changes¹.

In most cases, the samples contained one or two ^{13}C peptide carbonyl backbone labels and the NMR signals from these labeled sites were of the greatest interest. The labeled site signals were often unresolved from large natural abundance signals from lipid carbonyls and from unlabeled peptide carbonyls. To uniquely observe the labeled site signals, spectra were also taken of unlabeled peptide/lipid samples that were prepared in the same manner as those with labeled peptide. Subtraction of the natural abundance spectra from the labeled spectra yielded the difference spectrum of the labeled site(s). For

most samples, subtraction was considered to be optimal when natural abundance lipid glycerol signal at ~ 130 ppm was minimized in the difference spectrum.

A more efficient approach of filtering out the natural abundance signals involves the synthesis of directly bonded ^{13}C carbonyl and ^{15}N amide labeled peptides and utilizes the technique of rotational-echo double-resonance spectroscopy (REDOR). The details of this technique will be discussed in chapter five. In general, REDOR filtering has several advantages including: (1) better filtering of natural abundance signals; (2) requiring one rather than two samples; and (3) better compensation for spectrometer and probe drifts².

The REDOR filtering measurements were taken on the Varian Infinity Plus spectrometer using a triple resonance MAS probe equipped with 6 mm diameter rotors. The NMR detection channel was tuned to ^{13}C , the decoupling channel was tuned to ^1H , and the third channel was tuned to ^{15}N . ^{13}C and ^{15}N chemical shifts were externally referenced to the resonance of methylene carbon in adamantane at 38.2 ppm and $(\text{NH}_4)_2\text{SO}_4$ at 20 ppm, respectively. Experiments used a MAS frequency of 8.000 ± 0.002 Hz. In REDOR experiments, application of 1 ~ 2 ms of CP at 50 kHz was followed by a 1.0 ms dephasing period and then direct ^{13}C detection. A single 50 kHz ^{13}C refocusing π pulse was placed at the center of the dephasing period and ^1H TPPM decoupling of 65 kHz was applied during both dephasing and detection³. The ^{13}C transmitter was set to 155 ppm and the ^{15}N transmitter was set to 115 ppm. For the S_1 acquisition, the dephasing period contained a 40 kHz ^{15}N π pulse at the middle and end of each rotor cycle, while the S_0 acquisition did not contain these pulses. XY-8 phase cycling was used for the ^{15}N pulses^{4,5}. The REDOR filtered spectrum was processed with 50 Hz line broadening of the difference FID ($S_0 - S_1$).

RESULTS AND DISCUSSION

Peptide binding to Lipids. Since we can prepare fusogenic fusion peptide solutions that do not pellet under ultracentrifugation, it is possible to examine the binding strength of peptide to lipid. This is an important issue because the NMR signals are observed for fusion peptide in all types of environment, i.e. membrane-bound, aggregated or free. Since we are particularly interested in the membrane-bound peptide, the contribution from the other two sources must be eliminated. The aggregated peptide can be avoided by selecting an optimal buffer solution as described in the previous chapter. The unbound free peptide can be separated by centrifugation after mixing peptide and lipid since the membrane-bound peptide will stay in the pellet with the lipid. We can then estimate the percentage of binding by comparing the initial peptide concentration to that found after addition of lipid and subsequent centrifugation.

Table 2 clearly illustrates that there is strong binding between fusion peptide and membrane lipids. Binding to LM is quantitative and binding to pure neutral or negatively charged lipids is 75 – 90%. Therefore we can use centrifugation to ensure that we are examining only membrane-bound fusion peptides.

Table 2. Fusion Peptides Binding to Membranes.

Lipid	Peptide (mM): Lipid (mM) ratio ^a	% Binding ^b
DTPC	0.50:100	75
DMPC	0.50:100	80
POPG	0.50:100	90
DTPC	0.125:25	80
LM-1	0.125:25	99
LM-2	0.125:12.5	95
LM-3	0.125:10	97
LM-3 ^c	0.125:10	96
LM-3	0.014:1.1	88
LM-3 ^d	0.014:1.1	88

^a The binding percentage for the first three samples were estimated by method 2 and those of the rest of the samples were estimated by method 1.

^b Estimated error: $\pm 10\%$.

^c Measurements were made with lipid dispersion samples except for these last three entries which was made with 100 nm diameter vesicles.

^d Measurements were made with FP peptide except for this entry which was made with FPK3 peptide.

Dependence of 1D NMR Spectra on Sample Conditions. Figure 9 displays the 1D MAS spectra of different ^{13}C carbonyl labeled peptides. Generally, the carbonyl linewidth is a marker of the structural heterogeneity in the vicinity of the labeled nucleus or nuclei. For example, Figure 9a displays the spectrum of polycrystalline AGG-(A1G2)_C while Figure 9b displays the spectrum for an unstructured singly ^{13}C carbonyl labeled epitope peptide HGRVGIYFGMK in frozen solution. The observed full-width-at-half-maximum (FWHM) linewidths of ~ 1 ppm and ~ 6 ppm mark the two extrema of highly structured and unstructured residues, respectively.

Figures 9c and 9d respectively display the 1D spectra of FP-(L7F8)_C in 7.5 mM frozen solution and hydrated lipid DTPC environments (1:20 peptide:lipid molar ratio). The lipid sample in 9d was prepared by method 2 using 100 μl of the 9c solution. DTPC was initially chosen for these studies because it is ether- rather than ester-linked and hence has no natural abundance carbonyl background. Thus, in Figure 9c and 9d the labeled carbonyl carbons contributed 90% of the observed intensity. The signals from the two ^{13}C labeled carbonyls were unresolved. In the presence of DTPC, the linewidth is ~ 2 ppm FWHM and is narrower than that found in frozen solution. These data indicate that: (1) the L7F8 region of FP interacts with lipid; and (2) in the presence of lipid, the L7F8 region is reasonably well structured, although not crystalline.

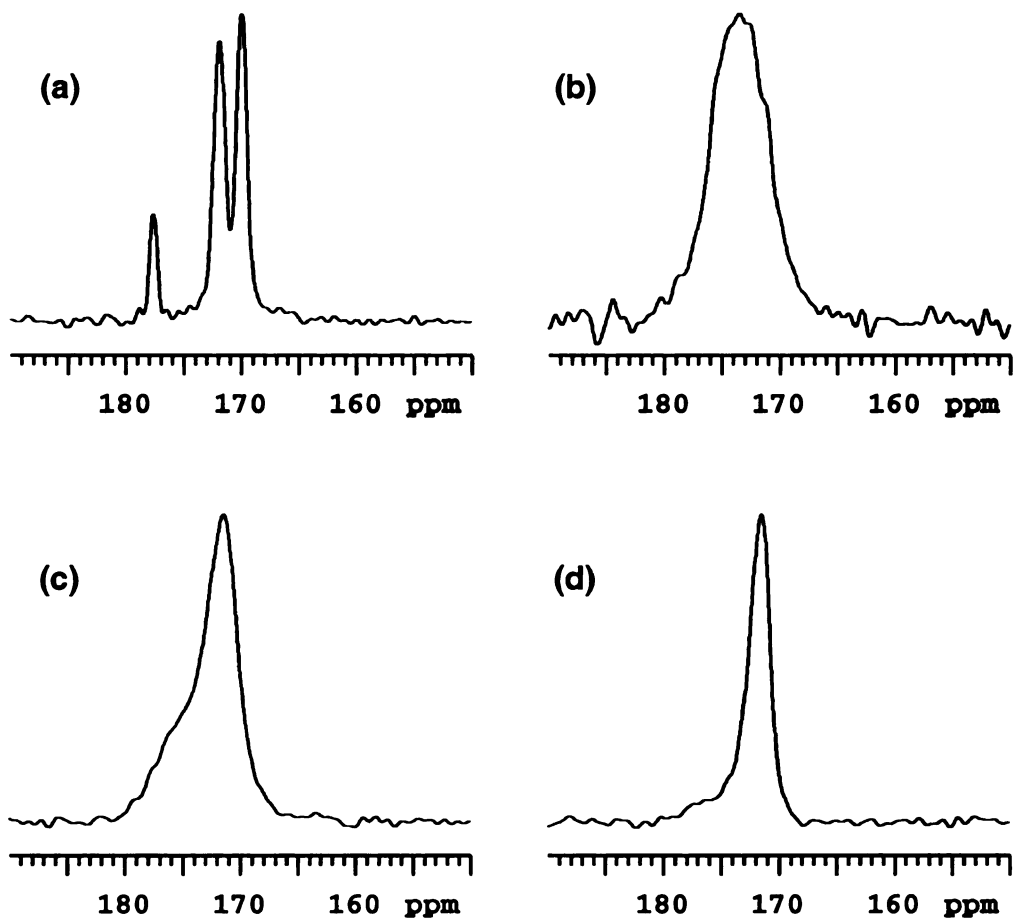


Figure 9. ^{13}C solid-state NMR spectra of (a) 5% polycrystalline AGG-(A1G2)_C peptide; (b) 20 mM frozen aqueous solution of HGRVGIYFGMK-F8_C epitope peptide; (c) 7.5 mM frozen aqueous solution of FP-(L7F8)_C; and (d) FP-(L7F8)_C/DTPC made by preparation method (2) at 1:20 peptide:lipid molar ratio. The AGG spectrum was taken at room temperature and the other spectra were taken at $-50\text{ }^{\circ}\text{C}$.

The dependence of the 1D spectrum on lipid composition was also investigated. As displayed in Figure 10, significantly different spectra were obtained for FP-F8_C for samples made either with (a) pure DTPC or with (b) LM-1 dispersions. The 10a and 10b samples were made using preparation method 1 at 1:200 peptide:lipid molar ratio. In 10a, the raw spectrum is displayed while in 10b, a difference spectrum between the FP-F8_C/LM-1 sample and a pure LM-1 sample is displayed. Figure 10b is best described by a single component with FWHM linewidth ~ 2.7 ppm, and reflects a relatively structured F8 residue. In Figure 10a, the spectrum is best described by two partially resolved components which likely correspond to at least two distributions of structures, each with significant population. It is unlikely that either component in 10a has a large contribution from the $\sim 20\%$ natural abundance peptide carbonyl signal because an unlabeled FP/DTPC sample at 1:80 peptide:lipid molar ratio generated a broad carbonyl absorption which ranged from 167 ppm to 174 ppm.

The different spectral lineshapes in Figure 10a and 10b demonstrate that there is some dependence of peptide structure on lipid composition. Although we have not yet understood the precise lipid compositional factors which cause the structural differences reflected in the two spectra, we have observed spectra similar to 10b at $\sim 1:100$ peptide:lipid molar ratio for samples made with LM-2 and LM-3. These mixtures differ from LM-1 only through addition of sphingomyelin, and sphingomyelin and PI, respectively. Two representative FP-F8_C/LM-3 difference spectra are displayed in Figure 10c and 10d, and were obtained from 1:80 peptide:lipid molar ratio samples made with preparation method 1 using respectively LM-3 lipid dispersion or 100 nm diameter

LM-3 vesicles. These difference spectra were obtained from subtraction between FP-F8_C and unlabeled FP samples and thus are nearly pure F8 signals.

The spectra from LM samples appear to be fairly independent of initial peptide concentration in the range of 12 - 120 μ M and also independent of the peptide:lipid molar ratio in the range of 1:200 to 1:20. For example, little difference was found between Figure 10b and 10c in which the samples were respectively made with 120 μ M and 12 μ M initial peptide concentrations and 1:200 and 1:80 peptide:lipid molar ratios. Spectra from samples made with FP-(G10F11)_C/LM-3 at 1:100 (Figure 10e) and 1:20 (Figure 10f) peptide:lipid molar ratio are also comparable. Although all samples were made with pH 7.0 HEPES, similar spectra were also obtained when unbuffered water (pH \sim 6) was used.

Spectra of samples made with DTPC also had little dependence on initial peptide concentration but had some dependence on peptide:lipid molar ratio. For example, with both 1:200 peptide:lipid molar ratio, the two-component spectrum in Figure 10a is similar in appearance to the one in Figure 11a from FP-(L7F8)_C/DTPC sample. For this latter sample, the initial peptide concentration was 2.5 mM, which is more than an order-of-magnitude greater than the 120 μ M concentration used for sample 10a. However, as displayed in Figure 9d, a sample made with DTPC, 7.5 mM initial peptide concentration and 1:20 peptide:lipid molar ratio gives a significantly different spectrum than that in Figure 10a. The single-component 9d spectrum closely resembles the Figure 10b-d spectra of samples made with LM.

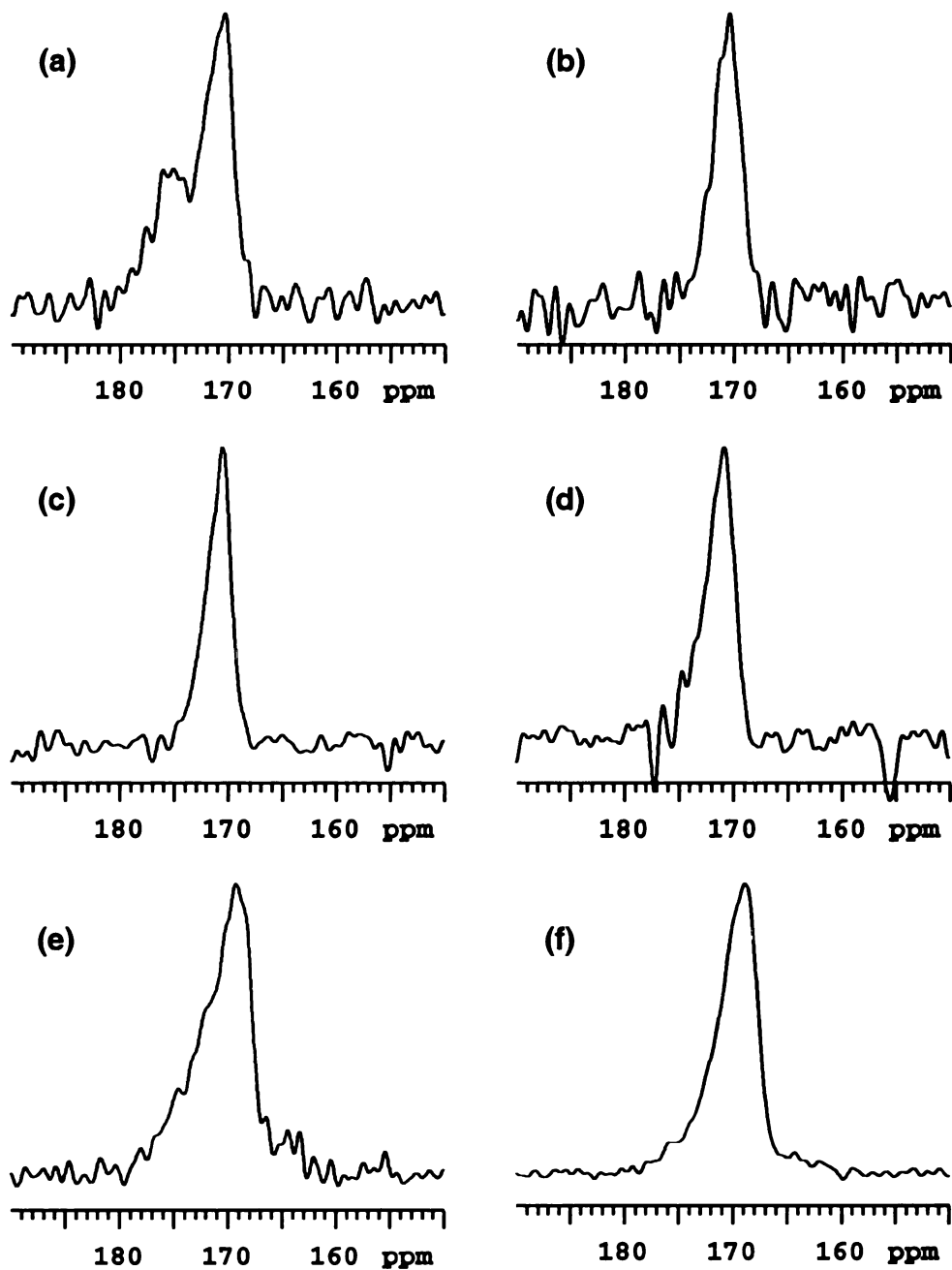


Figure 10. ^{13}C solid-state NMR spectra of samples made from FP-F8_C bound to (a) DTPC dispersion, (b) LM-1 dispersion, (c) LM-3 dispersion, and (d) 100 nm diameter LM-3 vesicles with a peptide:lipid molar ratio of (a), (b) 1:200 and (c), (d) 1:80; and spectra of samples made from FP-(G10F11)_C bound to LM-3 with a peptide:lipid molar ratio of (e) 1:100 and (f) 1:20.

In addition, spectra showed little dependence on how the samples were prepared. Figure 11 compares results using the three preparation methods. As discussed in the description of peptide binding strength measurements, methods 1 and 2 differ in that 1 allows us to eliminate the contribution from unbound peptide. However, if the peptide binds strongly to the membrane and the amount of unbound peptide can be neglected, there will be little difference between these two methods. This is indeed what we found when we compared the spectra of samples made with FP-(L7F8)_C/DTPC at 1:200 peptide:lipid molar ratio using method 1 (Figure 11a) and method 2 (Figure 11b). The similarity of the two spectra is consistent with our binding measurements (cf. Table 2) and therefore suggests that the spectra we collected from samples prepared by method 2 are also dominated by the membrane-associated peptide structure. Method 3 examines whether pre-mixing the peptide and lipid in organic solvent has any impact on the final structure of the membrane-associated peptide. Figures 11c and 11b are the REDOR filtered spectra of samples made with FPK3-F8_CL9_N/LM-3 at a 1:100 peptide:lipid molar ratio, and show that as long as the organic solvent is removed and the peptide/lipid mixture is hydrated, the membrane-associated peptide prepared by method 3 will adopt a similar structure as obtained by method 1. Besides sample preparation methods, little difference was found whether samples were slowly cooled during ~ 1 minute while spinning in the NMR probe or were frozen in ~ 1 sec by immersion of the sample rotor in liquid nitrogen. Similar spectra were also obtained after freeze/thaw cycling and after incubation of the sample at 37 °C for 1.5 hours (data not shown). All these results indicate that the observed membrane-associated peptide structure is very stable and likely represents the thermal-equilibrium favored structure.

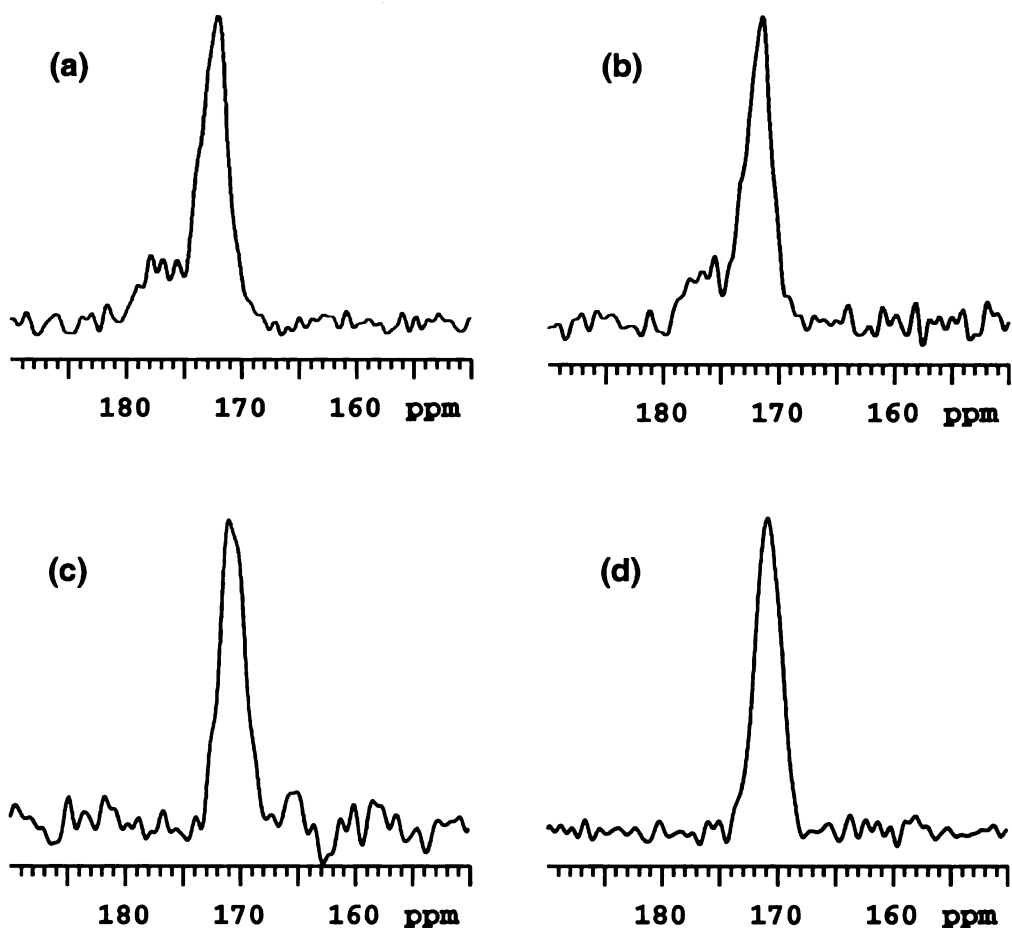


Figure 11. ^{13}C solid-state NMR spectra of samples made from FP-(L7F8)_C/DTPC with a peptide:lipid molar ratio of 1:200 by (a) method 1 and (b) method 2; and spectra of sample made from FPK3-F8_CL9_N/LM-3 with a peptide:lipid molar ratio of 1:100 by (c) method 1 and (d) method 3.

In summary, our 1D spectral data suggest: (1) there is some dependence of peptide structure on lipid composition; (2) little dependence of structural distributions on initial peptide concentration for either LM or DTPC samples; (2) little dependence of structural distributions on peptide:lipid molar ratio for samples made with LM; (3) significant dependence of structural distributions on peptide:lipid molar ratio for samples made with DTPC; and (4) once the peptide binds to the membrane, the peptide structure is the same with different preparation methods and is stable under various thermal

conditions. These data strongly suggest that fusion peptide/lipid samples should be prepared with LM rather than single lipids.

1D NMR Spectral Scanning down the FP23 Backbone. Difference spectra for LM-bound FP peptide are displayed in Figure 12a-h and are composed of carbonyl signals from labeled Ala-1, Val-2, Phe-8, Gly-10, Phe-11, Ala-14, Ala-15, and Ala-21, respectively. The samples were made by preparation method 1 with a peptide:lipid molar ratio of 1:100. The Val-2, Phe-8, Phe-11, Ala-15, and Ala-21 spectra are from samples made with LM-2 while the Ala-1, Gly-10, and Ala-14 spectra are from samples made with LM-3. Signals for labels between Ala-1 and Ala-15 all contained a relatively sharp feature with linewidth of 2 - 3.5 ppm, which suggests that a large population of membrane-bound peptide molecules share a common structure at each labeled site. The approximately symmetric lineshapes for Phe-8, Gly-10, Phe-11, and Ala-14 suggest that the peptide center has a high degree of structural order in a membrane environment. By contrast, the ~ 5 ppm linewidth of FP-A21_C indicates a higher degree of structural disorder at this site. Overall, these data are consistent with a model of insertion of the N-terminal and central residues of the peptide into the membrane and the C-terminus outside the membrane. In this model, there is greater structure for the residues within the membrane than outside the membrane. This is a reasonable premise because within the membrane, hydrogen bonding must be either inter- or intra-peptide, whereas outside the membrane, peptide-H₂O hydrogen bonds may be present and can allow for greater structural disorder.

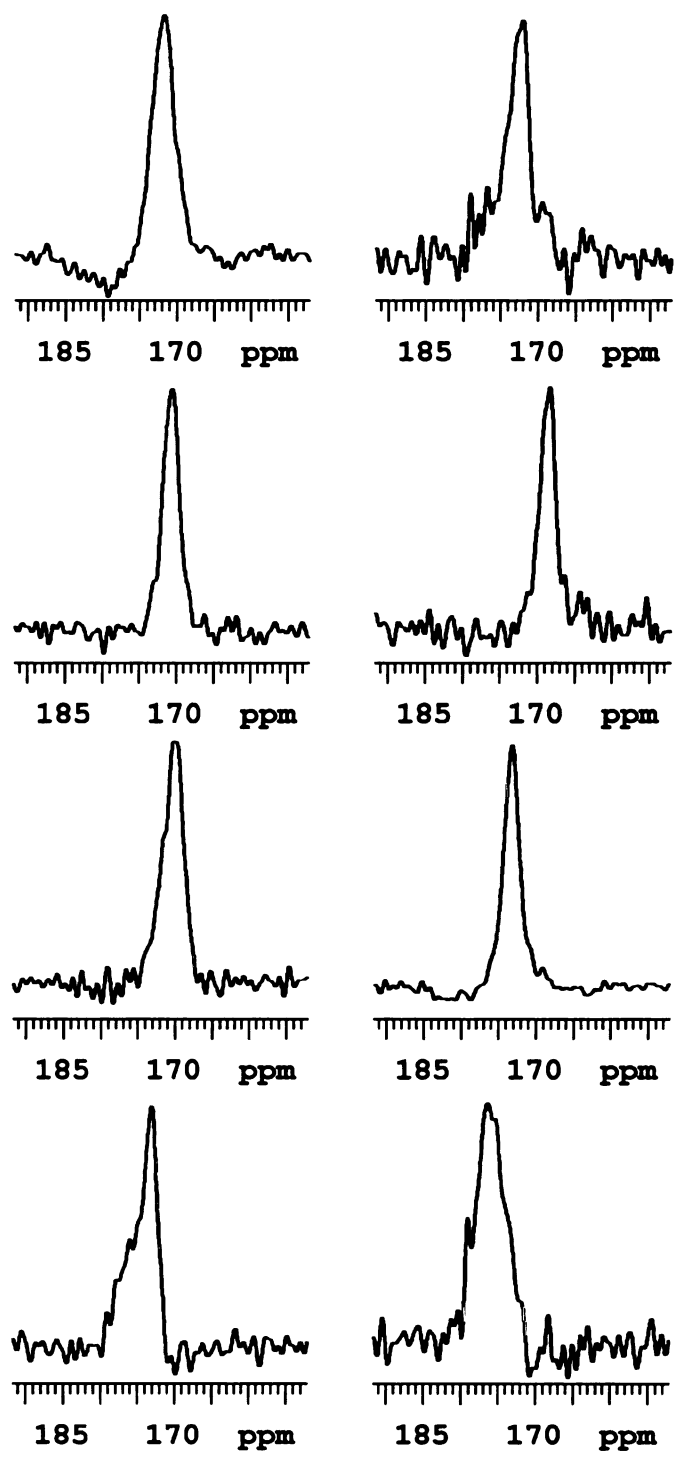


Figure 12. ^{13}C solid-state NMR difference spectra of LM-bound (a) FP-A1_C, (b) FP-V2_C, (c) FP-F8_C, (d) FP-G10_C, (e) FP-F11_C, (f) FP-A14_C, (g) FP-A15_C, and (h) FP-A21_C. Samples were prepared by method 1 with a peptide:lipid molar ratio of 1:100.

Correlation of Carbonyl Chemical Shifts with Secondary Structure. Secondary structure at the different labeled carbonyl carbons in the membrane-bound fusion peptide was characterized using the known experimental correlation between secondary structure and NMR chemical shift⁶. For peptide or protein carbonyl carbons, helical secondary structure generally correlates with downfield (to higher ppm) chemical shift while strand structure correlates with upfield (to lower ppm) chemical shift. Table 3 lists the peak experimental shifts for different carbonyl nuclei in the more structured N-terminal and central regions of the LM-bound fusion peptide, the typical ranges of chemical shifts observed for different secondary structures for that residue type, and the assignment of the local secondary structure based on these data. All of the peak chemical shifts are most consistent with a β strand structure.

Table 3. Structural Correlations from Carbonyl Chemical Shift Analysis.

Labeled Residue ^a	Experimental CS (ppm)	α Helical CS Range (ppm) ^b	β Strand CS Range (ppm) ^b	CS Predicted Structure
Ala-1	171.9	175.78 – 178.42	172.28 – 175.30	β strand
Val-2	172.2	173.97 – 176.73	171.11 – 173.89	β strand
Phe-8	170.6	173.45 – 176.21	170.32 – 173.58	β strand
Gly-10	168.4	171.98 – 174.44	168.67 – 171.83	β strand
Phe-11	170.3	173.45 – 176.21	170.32 – 173.58	β strand
Ala-14	173.4	175.78 – 178.42	172.28 – 175.30	β strand
Ala-15	173.2	175.78 – 178.42	172.28 – 175.30	β strand

^a The membrane-associated FP was ¹³C carbonyl labeled with a peptide:lipid molar ratio of 1:100.

^b Each range corresponds to about 90% of the residues found in that conformation.

Structure Similarity of Membrane-Associated FP, FPK3, FPW, and FPK3W. The previous chapter has demonstrated the impact on biological function of different peptide oligomer sizes in aqueous buffer. The results from the four fusion peptide constructs showed that FP, FPK3 and FPK3W have comparable fusogenicity while FPW has much less fusogenicity probably due to the large aggregates it forms in aqueous solution. It is therefore interesting to see whether their membrane-associated structures are comparable. Figure 13 displays the REDOR-filtered difference spectra of sample made with LM-3 associated (a) FP-F8_CL9_N, (b) FPK3-F8_CL9_N, (c) FPW-F8_CL9_N, and (d) FPK3W-F8_CL9_N at ~ 1:80 peptide:lipid molar ratio. Because of the directly bonded ¹³C-¹⁵N spin pairs in the peptides, the Phe-8 carbonyl signals dominate the displayed REDOR-filtered difference spectra, with quantitative attenuation of the natural abundance ¹³C signals from lipid and peptide. In all spectra, the FWHM linewidths are ~ 2.5 ppm, which is consistent with a relatively narrow conformational distribution at Phe-8, and the peak chemical shifts are ~ 171 ppm, which is consistent with non-helical local structure⁶. The overall similarity of the lipid mixing data and NMR spectra for the FP, FPK3 and FPK3W peptides suggests comparable interactions with LM-3 membranes, and the possibility that FPK3 and FPK3W can be used in place of FP in later experiments.

The soluble oligomerization state varies substantially among the four peptides, so the similarity of the spectra indicates that the membrane-associated peptide secondary structure is approximately independent of this oligomerization state. In addition, the similar spectra indicate that the differences in M_f values among the different peptides are not due to large variations in secondary structure near Phe-8, i.e. non-helical vs. helical structure.

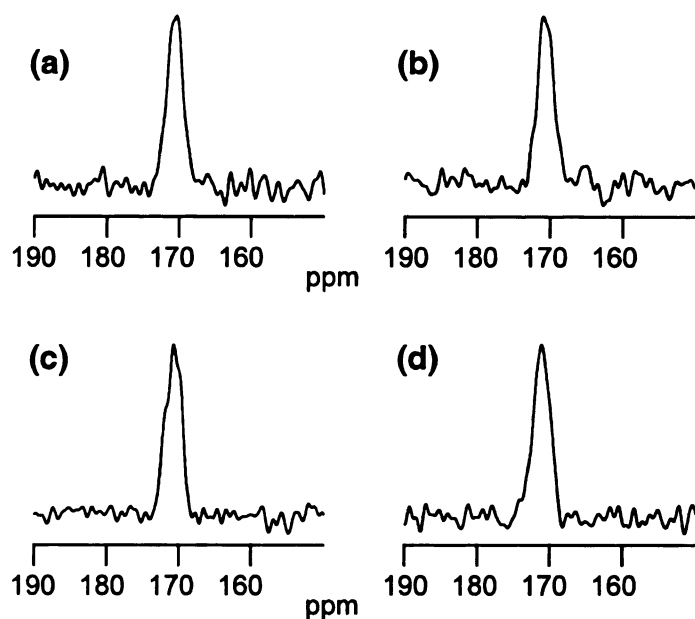


Figure 13. ^{13}C solid-state NMR spectra of membrane-associated fusion peptide samples with (a) FP-F $_{8\text{C}}\text{L}_{9\text{N}}$, (b) FPK3-F $_{8\text{C}}\text{L}_{9\text{N}}$, (c) FPW-F $_{8\text{C}}\text{L}_{9\text{N}}$, and (d) FPK3W-F $_{8\text{C}}\text{L}_{9\text{N}}$. Each sample contained $\sim 0.3 \mu\text{mol}$ peptide and $40 \mu\text{mol}$ LM3. The displayed REDOR-filtered difference spectra are dominated by the Phe-8 carbonyl signals.

CONCLUSION

In this chapter we examined the binding strength of the fusion peptide and membrane lipid. These results allow us to use ultracentrifugation to separate membrane-associated peptide from unbound peptide so that we only observe the structure of peptide in the membrane environment. In general, when the peptide binds to the lipid, the structure is stable and insensitive to various preparation methods and thermal conditions. There is some dependence on lipid composition. Peptide binding to DTPC is weaker than to a lipid mixture whose composition is close to that of HIV-1 virus infected host cells. The peptide also has greater structural homogeneity with LM, and peptide structure was invariant over a ~1:20-200 peptide:lipid molar ratio range. This strongly suggests that future fusion peptide studies should incorporate these kinds of lipid mixtures. Investigation of peptide structure across the backbone shows that the N-terminal and central regions of the peptide are well structured while the C-terminus is more flexible. Furthermore, correlating the carbonyl chemical shifts with secondary structure suggests that the N-terminal and central regions have a β strand secondary structure. A more precise secondary structure measurement will be discussed in next chapter using two-dimensional exchange spectroscopy.

REFERENCE

1. Bodner, M. L., Gabrys, C. M., Parkanzky, P. D., Yang, J., Duskin, C. A., and Weliky, D. P. Temperature dependence and resonance assignment of ^{13}C NMR spectra of selectively and uniformly labeled fusion peptides associated with membranes. *Magn. Reson. Chem.*, in press.
2. Yang, J., Parkanzky, P. D., Bodner, M. L., Duskin, C. G., and Weliky, D. P. (2002) Application of REDOR subtraction for filtered MAS observation of labeled backbone carbons of membrane-bound fusion peptides. *J. Magn. Reson.* 159, 101-110.
3. Bennett, A. E., Rienstra, C. M., Auger, M., Lakshmi, K. V., and Griffin, R. G. (1995) Heteronuclear decoupling in rotating solids. *J. Chem. Phys.* 103, 6951-6958.
4. Gullion, T., Baker, D. B., and Conradi, M. S. (1990) New, compensated Carr-Purcell sequences. *J. Magn. Reson.* 89, 479-484.
5. Gullion, T., and Schaefer, J. (1991) Elimination of resonance offset effects in rotational-echo, double-resonance NMR. *J. Magn. Reson.* 92, 439-442.
6. Zhang, H. Y., Neal, S., and Wishart, D. S. (2003) RefDB: A database of uniformly referenced protein chemical shifts. *J. Biomol. NMR* 25, 173-195.

CHAPTER IV

CONFORMATIONAL STUDIES OF THE MEMBRANE-ASSOCIATED FUSION PEPTIDE BY SOLID-STATE TWO-DIMENSIONAL EXCHANGE NMR MEASUREMENTS

BACKGROUND

For unoriented static samples, 2D exchange spectroscopy can determine the relative orientations of two nearby functional groups that are specifically labeled at the same kind of nuclei (^{13}C carbonyls in our case). In the experiment, the magnetization evolves under the anisotropic chemical shift (which is simply the dependence of chemical shift on the relative orientation between the functional group and the external magnetic field) of one of the labeled sites during t_1 , diffuses to the second site during the exchange period τ , and evolves under the anisotropic chemical shift of the second site during t_2 . If all of the molecules in the sample have the same local structure near the two labeled sites, then the chemical shift anisotropy (CSA) tensors of the two sites will have a well-defined relative orientation which will be manifested as correlation between the anisotropic chemical shifts of the two nuclei. This correlation will produce an off-diagonal intensity pattern in the 2D exchange spectrum which is distinctively characteristic of the relative CSA tensor orientation and the particular local structure. Because of the low probability of nearby natural abundance $^{13}\text{C}/^{13}\text{C}$ spin pairs, the off-diagonal intensity will be dominated by these labeled-site signals. In order to relate the off-diagonal pattern to local structure, simulated 2D spectra must be generated as a function of local structure and comparison made between the simulated and experimental spectra. The simulations require knowledge of the CSA principal values of each of the labeled sites as well as the orientation of the CSA principal axis system of each labeled site relative to its chemical bonds. In many cases, the principal values can be directly measured from 1D spectra and the principal axis system orientations are approximately known from studies of model compounds.

2D exchange spectroscopy has been used to investigate the structures of molecular solids, synthetic polymers and peptide in the manner described above¹⁻⁴. However, in systems where sample quantities are limited and the spectra of the two sites are not resolved, the application of this measurement may encounter the problems of low sensitivity and complex data analysis. These problems can be alleviated to a large extent by applying MAS, which periodically modulates the anisotropic interactions and narrows the broad peaks to comparatively sharp peaks at the isotropic and spinning sideband frequencies of the two labeled sites; therefore, it significantly improves the sensitivity and resolution. These frequencies for site $n = 1$ or 2 can be calculated as $\nu_M^n = \nu_{\text{iso}}^n + M\nu_r$, where ν_{iso}^n and ν_r are the isotropic and MAS frequencies, and $M = 0, \pm 1, \pm 2, \dots$. If the shift tensors of the two sites are not colinear, then the 2D exchange spectrum will contain off-diagonal crosspeaks which have frequency ν_M^n in one dimension and frequency $\nu_{M'}^{n'}$ ($M \neq M', n \neq n'$) in the second dimension. If the CSA principal values and principal axis orientations of each labeled site are known, then the relative off-diagonal crosspeak intensities can be simulated as a function of local structure as shown by Veeman *et al.*⁵, Spiess *et al.*^{6,7}, and Tycko *et al.*^{8,9}

In a peptide, the backbone is comprised of a series of planer peptide bond units with relative orientation specified by the dihedral angles ϕ and φ . In a peptide sample with ¹³C labeling at two carbonyl carbons on adjacent residues, the orientation of the CSA tensor for each carbonyl ¹³C is well-established¹⁰. Therefore, the local secondary structure dihedral angles (ϕ, ψ) are the main unknown parameters which determine the relative orientation of the carbonyl CSA tensors and hence the off-diagonal crosspeak intensities in a 2D exchange spectrum. Using the known bond geometry in peptides and

Co

excha

exper

and c

best

of th

ME

oba

wit

rote

cro

pu

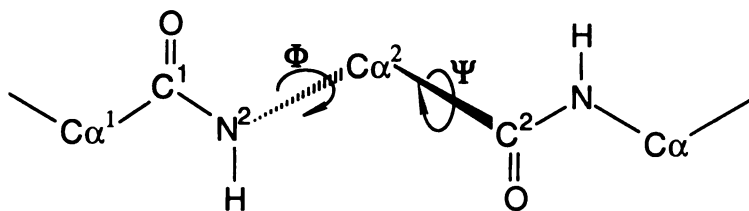
ty

fo

hr

(3

10



the known orientation of the carbonyl CSA tensor relative to its local bonding, formulas have been derived for the 2D

exchange crosspeak intensities as a function of $(\phi, \psi)^{8, 9}$. With the additional input of experimental CSA principal values, the simulated crosspeak intensities can be calculated and compared to the experimental intensities. The dihedral angle set corresponding to the best agreement between experiment and simulation will then be the most likely (ϕ, ψ) set of the more C-terminal residue.

METHODS

Two-Dimensional (2D) Exchange Experiments. 2D exchange spectra were obtained on the Varian VXR spectrometer at 2.5 kHz spinning frequency and $-50\text{ }^{\circ}\text{C}$ with doubly ^{13}C carbonyl labeled peptide/lipid samples. Spectra were acquired using the rotor-synchronized pulse sequence $(\text{CP} - t_1 - \pi/2 - \tau - \pi/2 - t_2)$, in which (CP) represents cross-polarization from ^1H to ^{13}C , t_1 is the evolution period, $(\pi/2)$ represents a ^{13}C $\pi/2$ pulse, τ (500 ms) is the spin diffusion period, and t_2 is the ^{13}C detection period. Samples typically contained 2 μmole of labeled peptide. The experiment was run under the following conditions: (1) 800 μs CP was made with ^{13}C RF radiation at 47 kHz and a linear ramp on ^1H between 42 kHz and 52 kHz; (2) 47 kHz ^{13}C $\pi/2$ pulses were applied; (3) 72 t_1 points were taken with an increment of 40 μs ; (4) signals were acquired for 10 ms during t_2 ; (5) decoupling at 75 kHz was applied during t_1 and t_2 but not during τ ;

and (6) the recycle delay was 0.5 s. Complete data sets were collected in twelve-hour blocks and then summed together, with 10-15 blocks in a final data set.

Spectra were processed using NMRPipe software¹¹ with 150 Hz line broadening in the t_1 and the t_2 dimensions. In the 2D spectrum, structural information is contained in the relative intensities of the off-diagonal crosspeaks between the spinning sidebands of the labeled carbonyl sites. These intensities depend on the relative orientations of the two labeled carbonyls' chemical shift anisotropy (CSA) tensors and can be directly related to the dihedral angles ϕ and ψ of the more C-terminal labeled residue^{8, 12}.

Integrated experimental crosspeak intensities were calculated by summing the intensities of points in a 1 ppm \times 1 ppm area. To determine the most likely values for ϕ and ψ , experimental crosspeak intensities were compared to simulated crosspeak intensities calculated for a grid of ϕ and ψ values. This grid was made in 5° increments for $-180^\circ \leq \phi \leq 0^\circ$ and $-180^\circ \leq \psi \leq 180^\circ$. The simulated crosspeak intensities were calculated from a computer program supplied by R. Tycko (NIH) and included a small contribution (< 20%) from longitudinal ^{14}N relaxation, whose characteristic time is shorter than the 500 ms exchange time. The simulated crosspeak intensity pattern for a (ϕ, ψ) pair is the same as that for $(-\phi, -\psi)$. In addition to their dependence on ϕ and ψ , the simulated intensities depend on the orientation of the carbonyl CSA principal axes relative to the peptide group and on the carbonyl CSA principal values. The former were taken from the literature¹⁰ while the latter were experimentally determined from measurements of the 1D peak spinning sideband intensities measured at a few different spinning frequencies between 2 kHz and 4 kHz¹³. In the FP-(L7F8)_C/DTPC sample, the sideband intensities were measured from raw 1D spectra and contained a small

contribution (< 10%) from natural abundance signals of unlabeled peptide carbonyls. For the LM-3 samples, the sideband intensities were measured from 1D difference spectra and only contained contributions from the labeled carbonyl nuclei. In all samples, the chemical shifts of the two labeled carbonyl nuclei were not resolved so the same set of principal values was assumed for both nuclei.

In the 2D analysis, the total squared deviation $\chi^2(\phi, \psi)$ between experiment and simulation was evaluated as:

$$\chi^2(\phi, \psi) = \sum_i [E_i - \lambda(\phi, \psi) \times S_i(\phi, \psi)]^2 / \sigma^2, \quad i = 1 \text{ to } N. \quad (3)$$

where E_i and $S_i(\phi, \psi)$ are experimental and simulated off-diagonal crosspeak intensities, σ^2 is the mean-squared noise per data point, $\lambda(\phi, \psi)$ is a scaling factor calculated to minimize χ^2 at each (ϕ, ψ) pair, and N is the total number of data points. Because mirror image (across-the-diagonal) crosspeaks always have the same simulated intensity, the experimental mirror image crosspeak intensities were summed, and the twenty off-diagonal crosspeak intensities (from a 5×5 2D spectral array of spinning sidebands) were reduced to ten data points¹⁴.

RESULTS AND DISCUSSION

Model Studies. 2D exchange measurement was tested by measuring the dihedral angles of Gly-2 in the polycrystalline tripeptide Ala-Gly-Gly. Figure 14a displays the 2D exchange spectrum, and the arrow indicates an off-diagonal crosspeak. The experimental data were fitted with simulations which yield a goodness-of-fit parameter χ^2 for each possible set of dihedral angles as shown in the contour plot of Figure 14b. The best fit

secondary structure is given by the smallest χ^2 . This region is coincident with the crystallographically determined (ϕ , ψ) values of (-83° , 170°).

A more realistic test was made in membrane-bound melittin, a 26-residue peptide that is the major protein component of the European honey bee *Apis mellifera* venom. X-ray diffraction data shows that soluble melittin is predominantly helical^{15, 16}. ¹H NMR studies^{17, 18} as well as CD and Raman spectroscopic studies^{17, 19, 20} also showed a helical conformation when melittin binds to membranes. Figures 14c and 14d are the 2D solid-state spectrum and χ^2 fitting result for membrane-bound melittin having the carbonyls of Gly-3 and Ala-4 ¹³C labelled. The minima – around the (-40° , -45°) dihedral angle set – again agree with the typical helix conformation.

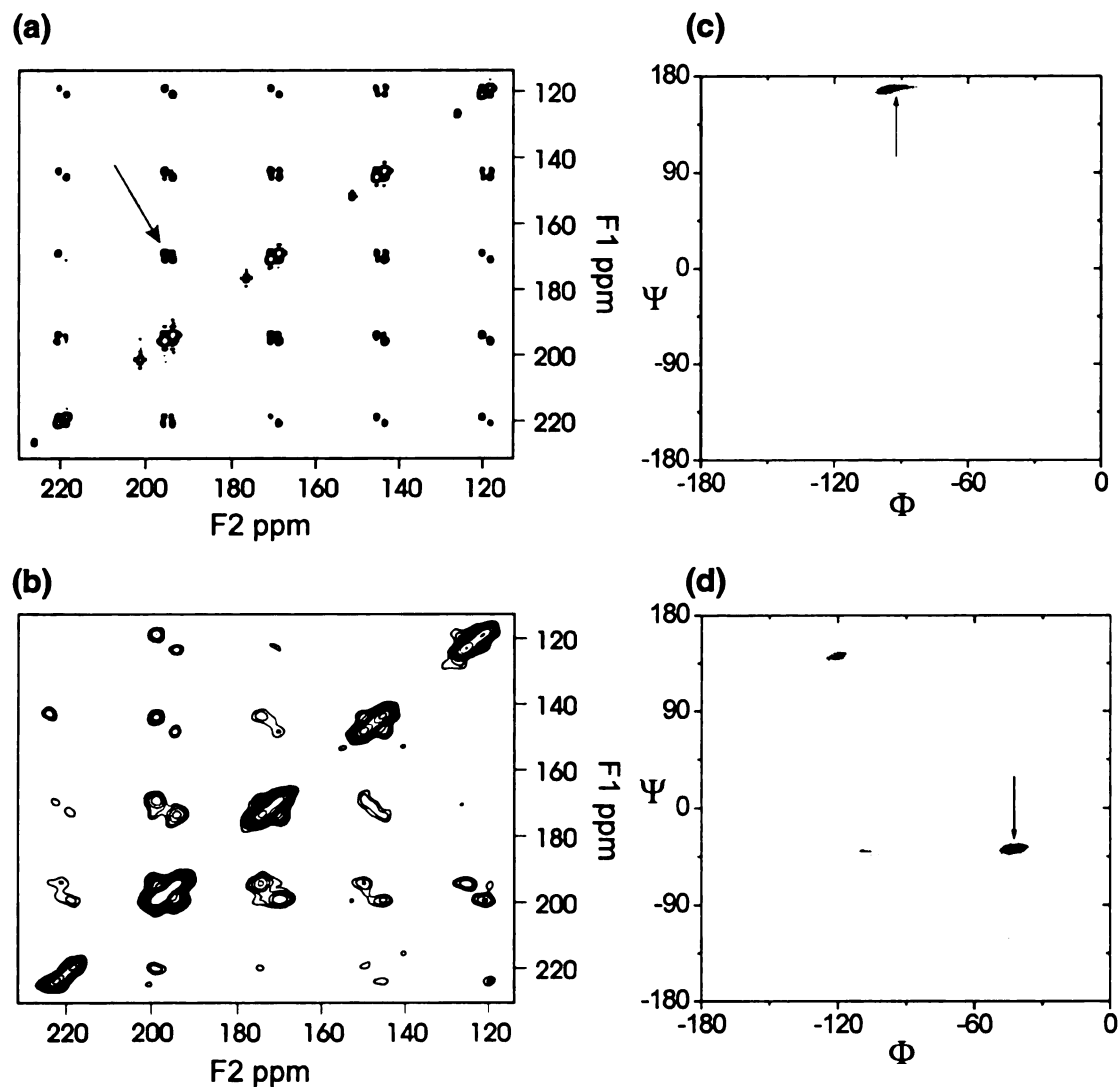


Figure 14. 2D ^{13}C solid-state NMR exchange spectra of (a) 5% polycrystalline AGG-(A1G2)_C peptide, and (b) Melittin-(G3A4)_C/DTPC with a peptide:lipid molar ratio of 1:20. The corresponding secondary structure analyses are shown in (c) and (d), respectively. These analyses are displayed as contour plots of the total squared deviation χ^2 (normalized to spectral noise) between experimental and calculated off-diagonal crosspeak intensities for a grid of dihedral angles. The darkest region in each plot represents the best global fitting.

2D Exchange Measurements for Refined Secondary Structure Determination of Membrane-Associated Fusion Peptide. Because chemical shifts only give a general indication of secondary structure (helix vs. strand), more precise measurements were made using 2D exchange spectroscopy on samples containing doubly carbonyl labeled peptides. These measurements typically provide dihedral angles with $\pm 20^\circ$ accuracy and can hence distinguish between various types of helical, turn, and sheet conformations. In addition, consistency between chemical shift and 2D exchange measurements provides much greater confidence in both types of measurements.

Figure 15a-d respectively displays 2D exchange spectra for FP-(A1V2)_C/LM-3, FP-(L7F8)_C/DTPC, FP-(G10F11)_C/LM-3, and FP-(A14A15)_C/LM-3, all made with 1:20 peptide:lipid molar ratio. The first, third, and fourth samples were prepared with method 1 and the second sample was prepared with method 2. Phosphate buffer (50 mM, pH 7.0) had been added to the FP-(L7F8)_C/DTPC sample after initial peptide/lipid binding, but this had little effect on the 1D spectrum and presumably the membrane-associated peptide structure. The 1D lineshapes of the LM-3 samples at 1:20 peptide:lipid ratio are comparable to their respective lineshapes at 1:100 peptide:lipid ratio with 2 - 3 ppm FWHM linewidths from each labeled carbonyl nucleus. The 1D lineshape of the FP-(L7F8)_C/DTPC sample (prior to phosphate addition) is displayed in Figure 9d with ~ 2 ppm linewidth from both nuclei. Thus, in all samples, it is reasonable to conclude that the labeled nuclei of interest are in a well-structured region of the peptide.

The experimentally determined carbonyl CSA principal values were: FP-(A1V2)_C/LM-3, 246 ppm, 180 ppm, 92 ppm; FP-(L7F8)_C/DTPC, 241 ppm, 179 ppm, 93 ppm; FP-(G10F11)_C/LM-3, 240 ppm, 174 ppm, 93 ppm; and FP-(A14A15)_C/LM-3,

241 ppm, 186 ppm, 94 ppm. The experimental uncertainty in each principal value determination was typically ± 2 ppm. These principal values are comparable to those measured in rigid solids^{12, 21} which indicates that large peptide backbone motions have been frozen out at the -50 °C measurement temperature.

The analyses for FP-(A1V2)_C/LM-3, FP-(L7F8)_C/DTPC, FP-(G10F11)_C/LM-3, and FP-(A14A15)_C/LM-3 are displayed in Figure 15e-h, respectively, and represent contour plots of the χ^2 difference between the experimental crosspeak intensities and the simulated intensities calculated for a grid of (ϕ , ψ) values. In the contour plots, black shading represents the lowest (best-fit) χ^2 , increasing lighter shades of gray represent increasing intervals of two units of χ^2 , and white shading represents all χ^2 greater than some value specified in the Figure 15 legend. One unit of χ^2 corresponds to about one confidence level²². Only negative values of ϕ are displayed because the simulated crosspeak intensities for any (ϕ , ψ) are the same as those for the corresponding ($-\phi$, $-\psi$). For Figure 15e, 15g, and 15h, the non-displayed dihedral angle regions of $-90^\circ < \phi < 0^\circ$ and $-180^\circ < \psi < 90^\circ$ would all be represented by white. Table 4 presents the best-fit (ϕ , ψ) for the Val-2, Phe-8, Phe-11, and Ala-15 residues of membrane-associated FP. In all four cases, the best-fit values correspond to the β strand region, which is consistent with the non-helical chemical shifts presented in Table 3. The corresponding ($-\phi$, $-\psi$) values are sterically disfavored for these non-glycine residues²³. Comparison of analyses using different NMR processing parameters (e.g. line broadening) suggests that each dihedral angle can be determined with a precision of about $\pm 20^\circ$.

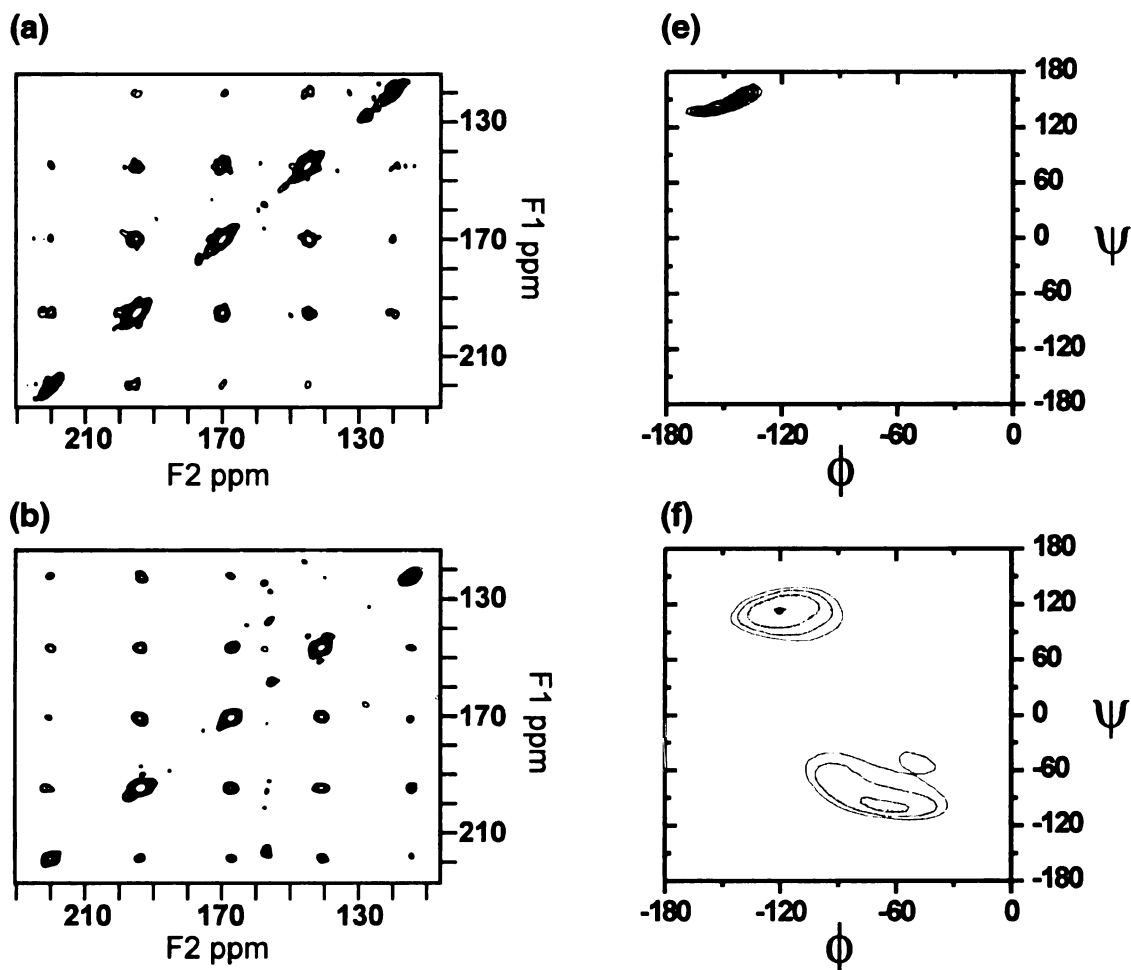


Figure 15. 2D ^{13}C solid-state NMR exchange spectra of (a) FP-(A1V2)_C/LM-3, (b) FP-(L7F8)_C/DTPC, (c) FP-(G10F11)_C/LM-3, and (d) FP-(A14A15)_C/LM-3. Each spectrum represents the summation of 10-15 twelve-hour data blocks. Secondary structure analyses for (a)-(d) are shown respectively in (e)-(h). These analyses are displayed as contour plots of the total squared deviation χ^2 (normalized to spectral noise) between the experimental and calculated off-diagonal crosspeak intensities for a grid of dihedral angles. The darkest regions represent values of χ^2 less than 6, 9, 12, and 12 for (e)-(h), respectively. Each lighter contour level represents an increase of two units in χ^2 .

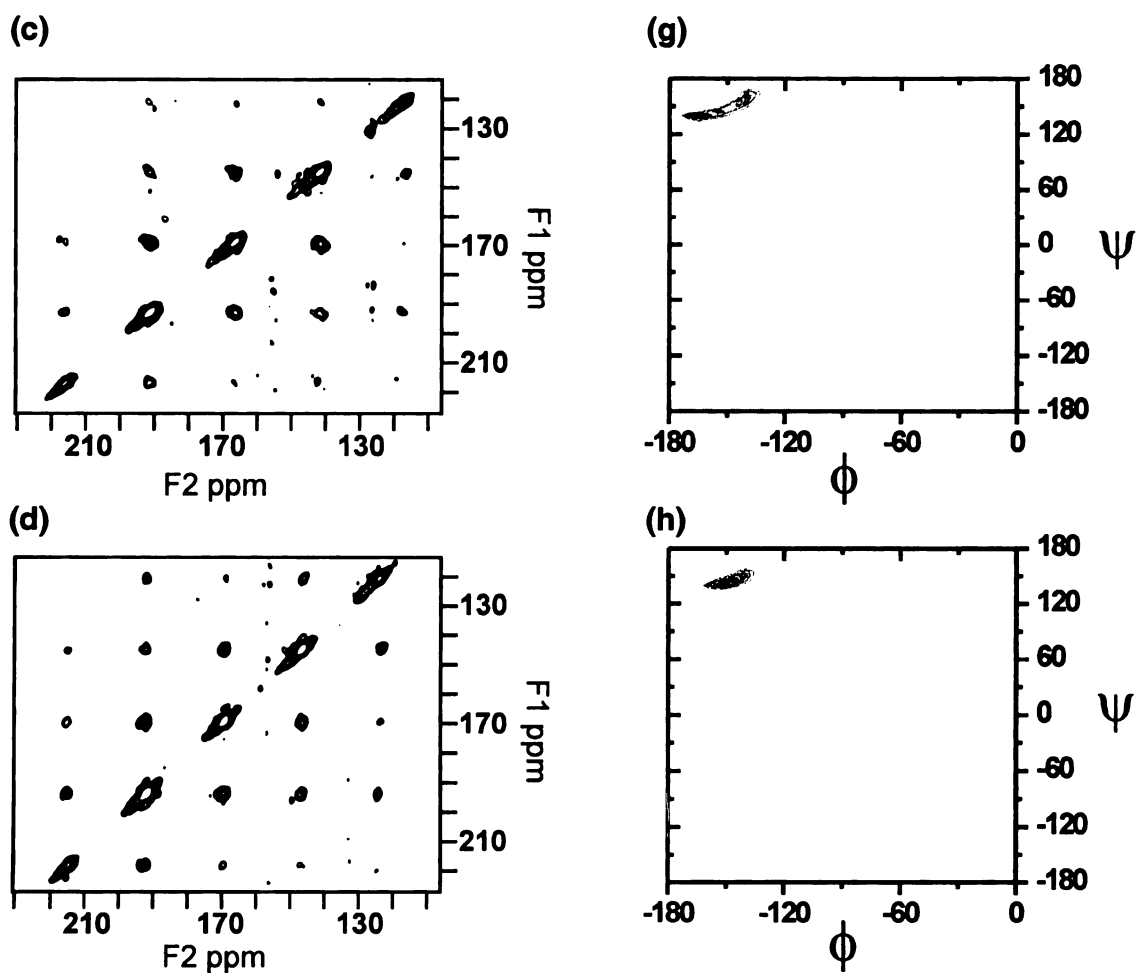


Figure 15 (cont'd).

Table 4. Structural Correlations from 2D Exchange Measurements.

Residue Determined	Best Fit ϕ, ψ	Predicted Structure
Val-2	$-160^\circ, 140^\circ$	β strand
Phe-8	$-120^\circ, 115^\circ$	β strand
Phe-11	$-165^\circ, 140^\circ$	β strand
Ala-15	$-145^\circ, 140^\circ$	β strand

CONCLUSION

The refined secondary structure determination by 2D exchange measurements is consistent with the β -strand structure predicted from the chemical shifts analysis. All these results provide strong evidence for the presence of an extended β -strand conformation in the N-terminal and central regions of the membrane-associated peptide. The C-terminus is more disordered. We interpret these data with a model of insertion of the N-terminal and central residues of the peptide into the membrane and the C-terminus outside the membrane. Within the membrane, there is greater peptide structure because hydrogen bonding must be either inter- or intra-peptide, whereas outside the membrane, greater conformational disorder is allowed because of the possibility of peptide-H₂O hydrogen bonds. N-terminal membrane insertion of the fusion peptide is an important element of biological fusion models and is biophysically reasonable because of the apolar character of the N-terminal residues and the polar/charged character of some of the C-terminal residues.

In the β -strand conformation, hydrogen bonding may be satisfied by a hairpin structure and/or by a parallel or antiparallel arrangement of peptide oligomers. One tertiary structure may be strongly preferred or there may be a mixture of populations of tertiary structures. Although none of our 2D exchange constraints are specifically consistent with a turn motif of a hairpin structure, none of the measurements have been made on any of the glycines that would likely be part of such a turn. In the next chapters, we will apply solid-state NMR REDOR technique to investigate possible formation of β sheet oligomer structures via detecting inter-peptide hydrogen bond patterns.

REFERENCE

1. Edzes, H. T., and Bernardis, J. P. C. (1984) Two-dimensional exchange NMR in static powders - interchain C-13 spin exchange in crystalline polyethylene. *J. Am. Chem. Soc.* *106*, 1515-1517.
2. Henrichs, P. M., and Linder, M. (1984) C-13 spin diffusion in the determination of intermolecular structure in solids. *J. Magn. Reson.* *58*, 458-461.
3. Tycko, R., and Dabbagh, G. (1991) Nuclear-Magnetic-Resonance crystallography - molecular orientational ordering in 3 Forms of solid methanol. *J. Am. Chem. Soc.* *113*, 3592-3593.
4. Dabbagh, G., Weliky, D. P., and Tycko, R. (1994) Determination of monomer conformations in noncrystalline solid polymers by 2-dimensional NMR exchange spectroscopy. *Macromolecules* *27*, 6183-6191.
5. Kentgens, A. P. M., Deboer, E., and Veeman, W. S. (1987) Ultraslow molecular motions in crystalline polyoxymethylene - a complete elucidation using two-dimensional solid-state NMR. *J. Chem. Phys.* *87*, 6859-6866.
6. Hagemeyer, A., Schmidt-Rohr, K., and Spiess, H. W. (1989) Two-dimensional nuclear magnetic resonance experiments for studying molecular order and dynamics in static and rotating solids. *Adv. Magn. Reson.* *13*, 85-130.
7. Luz, Z., Spiess, H. W., and Titman, J. J. (1992) Rotor synchronized MAS 2-dimensional exchange NMR in solids - principles and applications. *Isr. J. Chem.* *32*, 145-160.
8. Tycko, R., Weliky, D. P., and Berger, A. E. (1996) Investigation of molecular structure in solids by two-dimensional NMR exchange spectroscopy with magic angle spinning. *J. Chem. Phys.* *105*, 7915-7930.
9. Tycko, R., and Berger, A. E. (1999) Dual processing of two-dimensional exchange data in magic angle spinning NMR of solids. *J. Magn. Reson.* *141*, 141-147.
10. Oas, T. G., Hartzell, C. J., McMahon, T. J., Drobny, G. P., and Dahlquist, F. W. (1987) The carbonyl C-13 chemical-shift tensors of 5 peptides determined from N-15 dipole-coupled chemical-shift powder patterns. *J. Am. Chem. Soc.* *109*, 5956-5962.
11. Delaglio, F., Grzesiek, S., Vuister, G. W., Zhu, G., Pfeifer, J., and Bax, A. (1995) NMRPipe: a multidimensional spectral processing system based on UNIX pipes [see comments]. *J Biomol NMR* *6*, 277-293.

12. Weliky, D. P., and Tycko, R. (1996) Determination of peptide conformations by two-dimensional magic angle spinning NMR exchange spectroscopy with rotor synchronization. *J. Am. Chem. Soc.* 118, 8487-8488.
13. Herzfeld, J., and Berger, A. E. (1980) Sideband intensities in NMR - spectra of samples spinning at the magic angle. *J. Chem. Phys.* 73, 6021-6030.
14. Gabrys, C. M., Yang, J., and Weliky, D. P. (2003) Analysis of local conformation of membrane-bound and polycrystalline peptides by two-dimensional slow-spinning rotor-synchronized MAS exchange spectroscopy. *J. Biomol. NMR* 26, 49-68.
15. Terwilliger, T. C., Weissman, L., and Eisenberg, D. (1982) The structure of Melittin in the form-I crystals and its implication for Melittins lytic and surface-activities. *Biophys. J.* 37, 353-361.
16. Terwilliger, T. C., and Eisenberg, D. (1982) The structure of Melittin .1. structure determination and partial refinement. *J. Biol. Chem.* 257, 6010-6015.
17. Dawson, C. R., Drake, A. F., Helliwell, J., and Hider, R. C. (1978) Interaction of bee Melittin with lipid bilayer membranes. *Biochim. Biophys. Acta* 510, 75-86.
18. Knoppel, E., Eisenberg, D., and Wickner, W. (1979) Interactions of Melittin, a pre-protein model, with detergents. *Biochemistry* 18, 4177-4181.
19. Vogel, H. (1981) Incorporation of melittin into phosphatidylcholine bilayers - study of binding and conformational changes. *FEBS Lett.* 134, 37-42.
20. Vogel, H. (1987) Comparison of the conformation and orientation of Alamethicin and Melittin in lipid membranes. *Biochemistry* 26, 4562-4572.
21. Weliky, D. P., Bennett, A. E., Zvi, A., Anglister, J., Steinbach, P. J., and Tycko, R. (1999) Solid-state NMR evidence for an antibody-dependent conformation of the V3 loop of HIV-1 gp120. *Nat Struct Biol* 6, 141-145.
22. Bevington, P. R., and Robinson, D. K. (1992) *Data Reduction and Error Analysis for the Physical Sciences*, McGraw-Hill, Boston.
23. Cantor, C. R., and Shimmel, P. R. (1980) *Biophysical Chemistry*, W. H. Freeman, New York.

CHAPTER V

DESIGN AND OPTIMIZATION OF SOLID-STATE ROTATIONAL-ECHO DOUBLE-RESONANCE (REDOR) MEASUREMENTS TO PROBE DISTANCES BETWEEN CARBONYL CARBONS AND AMIDE NITROGENS

BACKGROUND

Due to the relative simplicity and robustness of the experiment and data analysis, rotational-echo double-resonance spectroscopy (REDOR) is one of the widely used MAS solid-state NMR techniques to analyze molecular structures by probing heteronuclear dipolar couplings and distances¹⁻⁷. Heteronuclear dipolar coupling is generally averaged out by MAS, but we can reintroduce the dipolar coupling by applying two π pulses in one rotor period and still take advantage of the better sensitivity and resolution from MAS. As the result of the reintroduced dipolar coupling, the magnetization of the observed nucleus will be reduced or “dephased” to S_1 as compared to S_0 from the sequence without the two π pulses in each rotor period. This reintroduced dipolar coupling can be accumulated over a long dephasing time which consists of many rotor periods. The amount of normalized reduction ratio, $(S_0 - S_1)/S_0$ or $\Delta S/S_0$, as a function of dephasing time, can be used to extract the heteronuclear dipolar coupling, and the corresponding heteronuclear distance can be obtained by its inversely proportional relationship to the cube root of the dipolar coupling (distance \propto (dipolar coupling)^{-1/3}).

REDOR experiments involve at least two channels, the detection channel that detects the NMR signal and the dephasing channel that reintroduces the heteronuclear dipolar coupling. In samples with a large number of protons, it is often necessary to include a third proton decoupling channel to minimize the strong proton dipolar coupling. For probing the dipolar coupling between ¹³C carbonyl carbons and ¹⁵N amide nitrogens, the detection channel is tuned to ¹³C and the dephasing channel is tuned to ¹⁵N.

In this study, REDOR was applied to identify inter-peptide hydrogen bonds through detection of the 40 ~ 45 Hz ¹³C-¹⁵N dipolar coupling arising from a ~ 4.1 Å ¹³C

carbonyl- ^{15}N amide distance. In the REDOR experiment, this is a rather weak coupling and requires a dephasing period of 10 ~ 30 ms duration and hundreds of NMR π pulses for detection. We therefore expended some effort in optimizing the REDOR experiment for detection of these hydrogen bonds. The compounds used for optimization was the lyophilized model helical peptide MB(i+4)EK-A $_9$ C $_{13}$ N, the lyophilized 5% 1- ^{13}C , ^{15}N L-leucine, the polycrystalline 10% 1- ^{13}C , ^{15}N Glycine and the lyophilized FP-F $_8$ C $_9$ L $_9$ N peptide.

The factors that we examined with model compounds include the quality of the pulses, ^1H decoupling sequence and strength, and REDOR sequence variant.

MATERIALS AND METHODS

Materials. A 17-residue acetylated peptide MB(i+4)EK-A $_9$ C $_{13}$ N (Ac-AEAAAKEAAAKEAAKA) was synthesized as a C-terminal amide with ^{13}C carbonyl labeling at Ala-9 and ^{15}N amide labeling at Ala-13. This peptide is predominantly (~85%) α helical in its lyophilized form so the two labeled nuclei should have a C-N internuclear distance of 3.9 ~ 4.2 Å⁸. A 1- ^{13}C , ^{15}N L-leucine sample was prepared by dissolving a 1:19 mixture of labeled:unlabeled leucine in water. After lyophilization, the two labeled nuclei should have a C-N internuclear distance of ~ 2.5 Å. A 1- ^{13}C , ^{15}N Glycine sample was prepared by dissolving a 1:9 mixture of labeled:unlabeled glycine followed by crystallization by slow evaporation of the water. The two labeled nuclei should also have a C-N internuclear distance of ~ 2.5 Å. A lyophilized FP-F $_8$ C $_9$ L $_9$ N dry peptide was used as a model compound that has directly bounded ^{13}C - ^{15}N pair with a distance of 1.3 ~ 1.4 Å.

Solid State NMR Spectroscopy. Experiments were done on the Varian Infinity Plus spectrometer using either a 4 mm triple resonance MAS probe or a 6 mm triple resonance MAS probe. The NMR detection channel was tuned to ^{13}C , the decoupling channel was tuned to ^1H , and the third channel was tuned to ^{15}N . ^{13}C and ^{15}N chemical shifts were externally referenced to the methylene resonance of adamantane at 38.2 ppm and $(\text{NH}_4)_2\text{SO}_4$ at 20 ppm, respectively. In our discussion of following results, “ ^{13}C ” and “ ^{15}N ” refer specifically to carbonyl carbon and amide nitrogen, respectively, and “intensity” refers to the integration of isotropic ^{13}C carbonyl peak.

In REDOR experiments two spectra were acquired: S_0 acquisition without a ^{13}C - ^{15}N recoupling sequence, and S_1 acquisition with such a sequence. The general REDOR sequence starts with 1 – 2 ms of CP at 50 kHz, followed by a few ms dephasing period and then direct ^{13}C detection¹. Optimization was performed using a variety of REDOR dephasing sequences, and different ^1H decoupling sequences and strengths during dephasing and acquisition. Unless noted otherwise, the XY-8 phase cycling scheme was used for the π pulses^{9, 10}. The ^{13}C transmitter was set close to the frequency of the labeled carbonyl or carboxyl carbon and the ^{15}N transmitter was set close to the frequency of the labeled amide or amine nitrogen. Calibration of the ^{13}C π pulse length was done with a “Z-filter” sequence (CP- $\pi/2$ - τ - π -acquire) in which ^1H decoupling was applied during the pulses and acquisition and for 10 μs at the beginning and end of the τ period. The ^{15}N π pulse was calibrated with minimization of the signal in S_1 spectrum at desired dephasing time. To obtain optimal compensation of B_0 , B_1 , and spinning frequency drifts, S_0 and S_1 FIDs were acquired alternately. The recycle delay was 1 s. The data were processed with 10 – 100 Hz line broadening and with fifth order polynomial baseline correction.

REDOR Data Analysis. The integrated signal intensities in the isotropic carbonyl regions of the S_0 and S_1 spectra are denoted as “ S_0 ” and “ S_1 ”. $\Delta S/S_0$ is a convenient normalized dephasing ratio for comparison of experiment and simulation and is defined:

$$\Delta S/S_0 = (S_0 - S_1)/S_0 = 1 - (S_1/S_0) \quad (4)$$

The corresponding dipolar coupling can then be extracted by fitting the experimental data with theoretical calculations, and related to the ^{13}C - ^{15}N distance r through the r^{-3} dependence of the dipolar coupling.

To estimate the real dephasing ratio from the specific labeled nuclear pair, the experimental $\Delta S/S_0$ values were multiplied by a correction factor of 1.23 for the 5% labeled L-Leucine sample and 1.10 for the 10% Glycine sample prior to fitting to eliminate the contribution of non-dephasing natural abundance carbonyls. For the model peptide MB(I+4)EK-A9 $_{\text{C}}$ A13 $_{\text{N}}$, the correction factor is about 1.2 ~ 1.3 which accounted for the ~ 15% population of random coil peptide in the sample, the small populations of labeled and natural abundance carbonyls which experience complete dephasing from neighboring natural abundance ^{15}N and labeled ^{15}N , respectively, and the remaining population of natural abundance carbonyls which do not dephase. For the FP-F8CL9N peptide, the correction factor is 1.25 and includes only the non-dephasing natural abundance carbonyls because the dephasing ratio from the directly bonded ^{13}C - ^{15}N pair dominates the overall results at the examined dephasing time.

The theoretical dephasing ratio was calculated using the formula^{1, 3}:

$$(\Delta S/S_0)_T = 1 - (1/2\pi) \int_0^\pi \int_0^\pi \{ \cos[2\sqrt{2} DT \times \sin(2\beta)\sin\alpha] \sin\beta \} d\beta d\alpha \quad (5)$$

where D is the heteronuclear dipolar coupling in Hz, T is the dephasing time, and (α, β) are the azimuthal and polar angles describing the orientation of internuclear vector in the rotor frame.

RESULTS AND DISCUSSION

Quality of REDOR π Pulses. The REDOR sequence mainly consists of π pulses, and the quality of these π pulses can directly affect the REDOR result. In general, there are several factors related to the quality of the π pulses: flip angle, homogeneity of the radiofrequency (RF) field along the sample, and pulse shape.

The pulse length tolerance of the REDOR experiment was examined with the MB(i+4)EK-A9_CA13_N peptide at 24 ms dephasing time where a few hundred pulses were applied. An array of pulse lengths was tested and the corresponding REDOR dephasing ratios were used to determine the optimal π pulse length range. The results (not shown) suggest that the REDOR experiment can tolerate pulse length errors of approximately $\pm 10\%$ from the ideal π pulse length. Experimentally it is possible to control the pulse length variation within this range.

The homogeneity of the RF coil along the rotor was estimated by dividing the volume of regular rotor into 6 segments (two outmost 1/6, two outer 1/6 and two central 1/6 positions), restricting sample into one of these segment and measuring the ¹³C and ¹⁵N π pulse length experienced by the sample. A 5% 1-¹³C, ¹⁵N L-leucine sample was used for the 4 mm rotor and a 10% 1-¹³C, ¹⁵N Glycine sample was used for the 6 mm rotor. The results are listed in Table 5 for the 4 mm rotor and Table 6 for the 6 mm rotor,

respectively. The corresponding REDOR dephasing curves are displayed in Figure 16 and Figure 17, respectively.

It is clear that in the NMR probe circuit, the RF field is not homogenous along the rotor. Samples placed at the edge of the rotor experienced a weaker field than samples placed at the center of the rotor. Therefore a longer pulse length is required to reach a certain flip angle as shown in Tables 5 and 6. Because the REDOR experiment employs many π pulses and the error due to incorrect pulse length setting can accumulate over the pulses, the inhomogeneity issue will have a significant impact on the result. Figures 16 and 17 displays the REDOR dephasing curves of samples placed at different positions in the 4 mm and 6 mm rotors, respectively. For comparison, the same settings optimized for samples placed at the central position were used in all other positions. For the 4 mm rotor, Figure 16 demonstrates that samples placed at the two central 1/6 positions gave the best results because the correct pulse length was applied. When samples were placed at the two outer 1/6 positions, the pulse length was too short enough to reach the desired flip angle and the results were worse. The pulse length experienced by samples placed at the two outmost 1/6 positions was so far from the correct value that the magnetization could not refocus, and no signal could be observed. Homogeneity is better in the 6 mm rotor than in the 4 mm rotor. Figure 17 shows only subtle differences between samples placed at the four 1/6 positions around the center of the rotor. Again, a significantly worse REDOR curve was observed when the sample was placed at the two outmost 1/6 positions of the 6 mm rotor.

Table 5. Pulse Length at Different Positions in the 4 mm Rotor.

Position in the Rotor (Top to Bottom)	¹³ C Pulse Length (μs) ^a		¹⁵ N Pulse Length (μs) ^a	
	π	2π	π	2π
Outmost 1/6	16.8	31.4	18.2	36.2
Outer 1/6	10.8	21.5	13.5	26.5
Central 1/6	10.0	19.7	12.6	25
Central 1/6	9.8	19.7	12.7	25.3
Outer 1/6	11.0	21.8	14.0	28.2
Outmost 1/6	14.4	28.5	18.6	37.4

^a The pulse lengths were measured with same RF field strength.

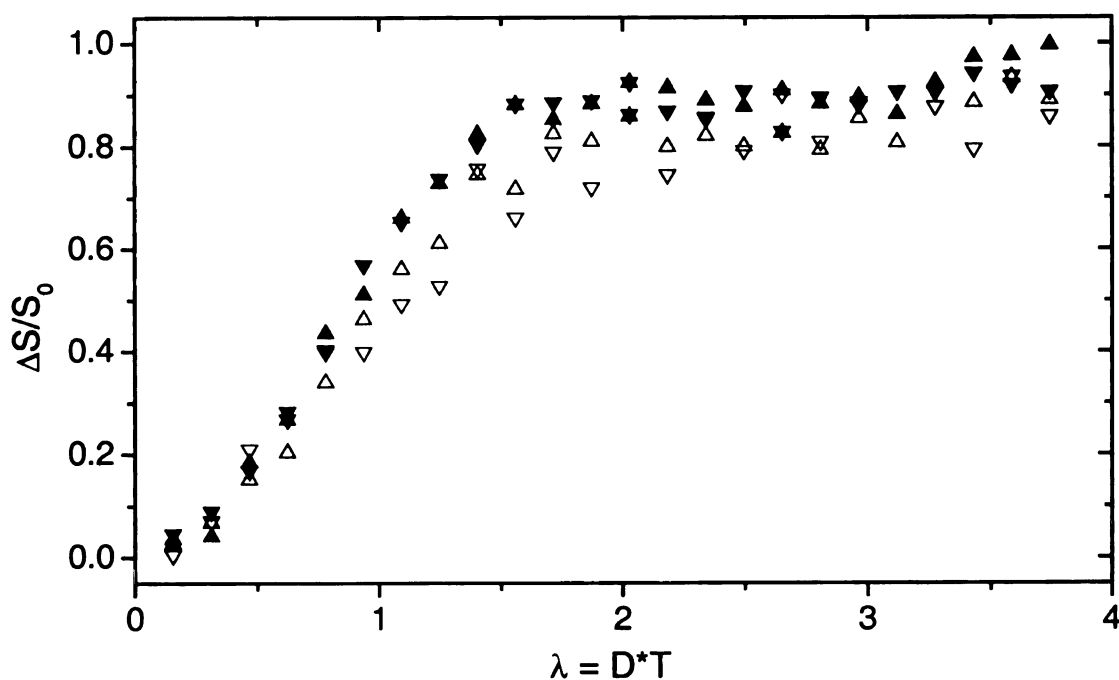


Figure 16. ¹³C-observed REDOR dephasing curve of calibrated $\Delta S/S_0$ for the 5% 1-¹³C, ¹⁵N L-leucine sample placed at different positions in the 4 mm rotor. λ is the product of dipolar coupling D (195 Hz, calculated from the 2.5 Å ¹³C-¹⁵N distance) and dephasing time T . All experiments used the pulse lengths from the central position. The filled triangles represent the results from two central 1/6 positions and the open triangles represent the results from two outer 1/6 positions. The results from the two outmost 1/6 positions are not shown because the signals are significantly attenuated.

Table 6. Pulse Length at Different Positions in the 6 mm Rotor.

Position in the Rotor (Top to Bottom)	¹³ C Pulse Length (μs) ^a		¹⁵ N Pulse Length (μs) ^a	
	π	2π	π	2π
Outmost 1/6	13.6	26.0	16.2	31.8
Outer 1/6	11.0	21.6	13.5	26.8
Central 1/6	10.0	19.9	12.5	24.8
Central 1/6	10.0	19.9	12.5	24.7
Outer 1/6	11.0	21.6	13.5	26.5
Outmost 1/6	13.0	25.2	15.8	31.2

^a The pulse lengths were measured with same RF field strength.

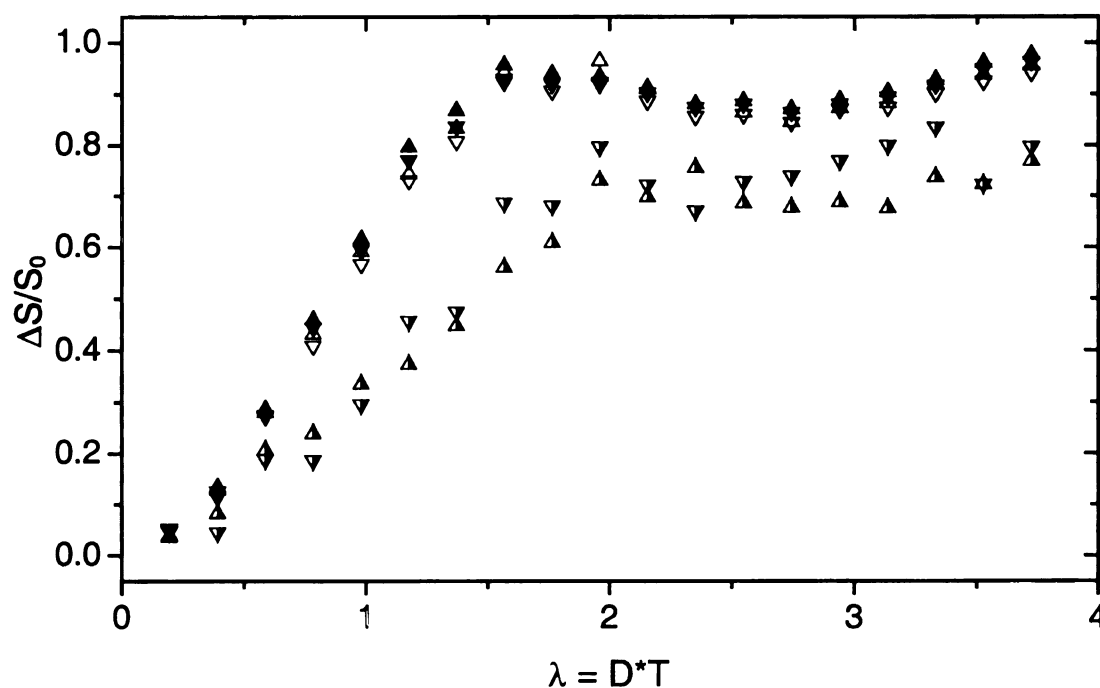


Figure 17. ¹³C-observed REDOR dephasing curve of calibrated $\Delta S/S_0$ for the 10% 1-¹³C, ¹⁵N glycine sample placed at different positions in the 6 mm rotor. A 195 Hz dipolar coupling D from 2.5 Å ¹³C-¹⁵N distance was applied. All experiments used the pulse lengths from the central position. The filled triangles represent the results from two central 1/6 positions and the open triangles represent the results from two outer 1/6 positions. The half-filled triangles represent the results from two outmost 1/6 positions.

It is of interest to compare the results between a full rotor and a 2/3 full rotor with the MB(i+4)EK-A9_CA13_N peptide, since it has the ¹³C–¹⁵N distance comparable to the real sample. Figure 18 displays the results of such comparison and suggests that for the 4 mm rotor, restricting the sample to 2/3 full volume significantly improves the REDOR results. For the 6 mm rotor, the results from the 2/3 full volume are only slightly better than for a full rotor. In summary, the RF homogeneity is uneven along the 4 mm and 6 mm rotors, and for practical reasons it is advantageous to restrict the sample volume to the central 2/3 of the rotor volume.

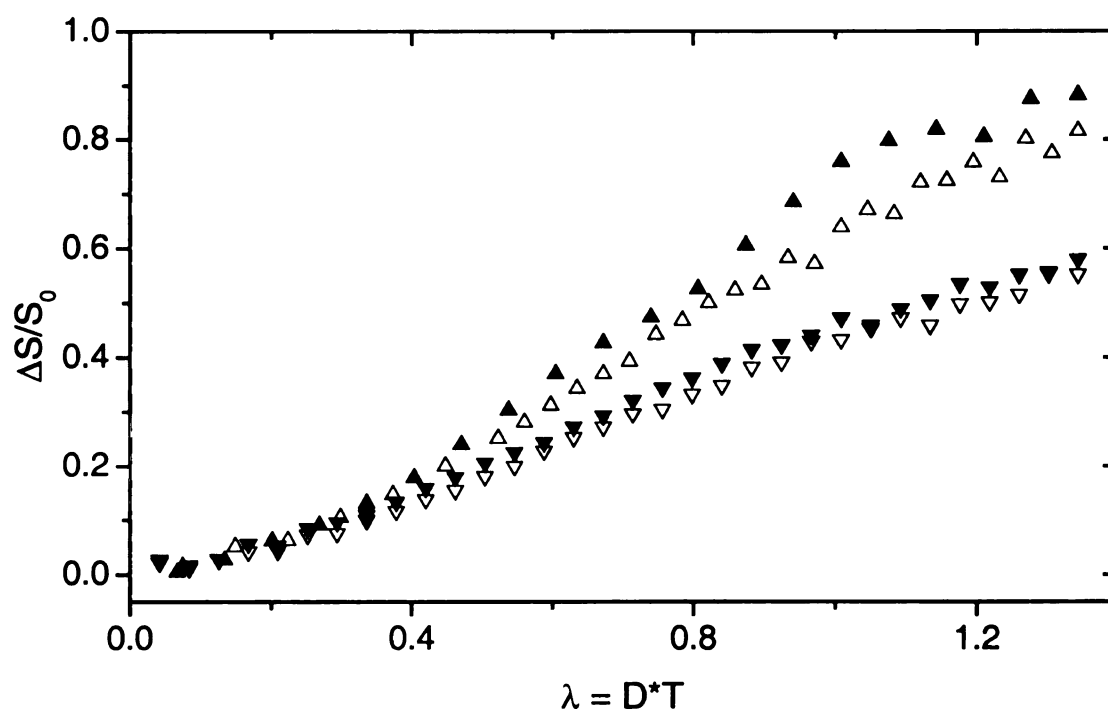
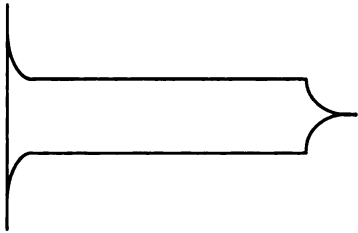
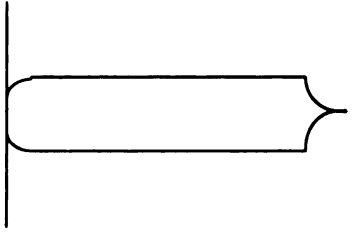
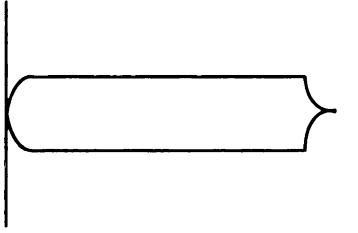
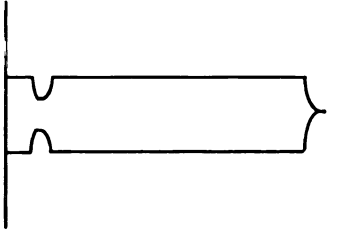


Figure 18. ¹³C-observed REDOR dephasing curve of calibrated $\Delta S/S_0$ for the MB(i+4)EK-A9_CA13_N peptide in full and 2/3 full 4 mm rotor (open and filled upper triangles “ Δ ”), and in full and 2/3 full 6 mm rotor (open and filled lower triangles “ ∇ ”). 100 kHz and 65 kHz TPPM decoupling were applied for the 4 mm and 6 mm rotors, respectively.

The pulse shape was observed on an oscilloscope. The carbon π pulse is almost a square wave while the nitrogen π pulse has significant ring-up and ring-down effects at the beginning and end of the pulse. An attempt to improve the pulse shape was made by inserting cables with different lengths in the circuit. Figure 19 shows that we can modify the pulse profile to nearly a square wave, but the corresponding REDOR ratio measured on the MB(i+4)EK-A₉C A₁₃N peptide at 24 ms dephasing time did not improve. This suggests that other properties (e.g. phase transients) associated with the pulse may also contribute to the imperfection.

Table 7. Pulse Profile Adjustment and Corresponding REDOR Dephasing Ratio.

Circuit Modification	Pulse Profile ^a	Experimental $\Delta S/S_0$ ^{b, c}
Original		0.41
Add 40 MHz $\lambda/4$ cable		0.41
Add 76 MHz $\lambda/4$ cable		0.42
Add 160 MHz $\lambda/4$ cable		0.39

^a The pulse profile was observed on an oscilloscope.

^b REDOR $\Delta S/S_0$ ratio was measured on the MB(i+4)EK-A9_CA13_N peptide at 24 ms dephasing time.

^c The uncertainty is 0.01.

¹H Decoupling Sequence and Strength in REDOR Experiments. After understanding the pulse imperfections in our spectrometer, we turned our focus to the ¹H decoupling sequence and strength during the dephasing and acquisition periods. In general, the proton decoupling sequence and strength affect the ¹³C transverse relaxation and residual coupling to protons. However, in the REDOR experiment these decoupling effects affect S_1 and S_0 similarly and cancel out in the dephasing ratio ($\Delta S/S$) calculation, so the REDOR results should be independent of proton decoupling as demonstrated by Schaefer and coworkers¹¹. However, there are also reports arguing that a strong proton decoupling field is essential in REDOR experiments to avoid cross-relaxation¹² and optimize the observed $\Delta S/S_0$ ratio¹³. Since most experiments use the 6 mm probe that has a relatively low decoupling field limit (~ 65 kHz), it is necessary to test the impact of limited decoupling in REDOR experiments.

The experiments were conducted on the MB(i+4)EK-A9_CA13_N peptide in the 2/3 volume restricted 4 mm rotor. Two kinds of proton decoupling sequences were used, regular continuous wave (CW) decoupling and two-pulse phase-modulation (TPPM) decoupling¹⁴. For each decoupling sequence, two fields (70 kHz and 100 kHz) were applied. Figure 19 shows the REDOR S_0 intensity and $\Delta S/S_0$ curve over a series of dephasing times. The results indicate that the TPPM decoupling can preserve the signal intensity better than regular decoupling. In Figure 19a, the S_0 intensities at the two fields with TPPM decoupling are almost the same and both are much higher than the one with regular decoupling. TPPM decoupling also improves the $\Delta S/S_0$ ratio as indicated in Figure 19b. At the same field strength, TPPM decoupling always gives a better result than regular CW decoupling. When comparing within the same decoupling sequence, we

found that higher decoupling field does lead to a better $\Delta S/S_0$ ratio. The abnormally high $\Delta S/S_0$ values with CW decoupling at long dephasing times are associated with a very large uncertainty due to small signal intensities.

Recently another experiment was conducted to test the existence of cross-relaxation in the REDOR experiments. Our main concern involves the nitrogen channel which employs many π pulses simultaneously with proton decoupling. Table 8 displays the results of applying different nitrogen π pulse fields with same proton decoupling at 65

Table 8. Dependence of REDOR $\Delta S/S_0$ on the ^1H Decoupling/ ^{15}N π Pulse Field Ratio.

Ratio of ^1H Decoupling and ^{15}N π Pulse Field ^a	1.6	2.1	2.6	3.3	3.9	4.6	5.2	6.5
Experimental $\Delta S/S_0$ ^b	0.38	0.44	0.47	0.49	0.50	0.47	0.45	0.38

^a The ^1H decoupling was fixed to 65 kHz and the ^{15}N π pulse field was varied from 40 kHz to 10 kHz.

^b The results were obtained at 24 ms dephasing time.

kHz. Ishii and coworker reported that the RF field intensity for proton decoupling should be set to around three times that of the dilute spin pulses to avoid cross-relaxation between protons and dilute spins when applying multiple pulses of the dilute spin simultaneously with proton decoupling¹². Although in the REDOR experiment, the ^{13}C - ^{15}N dipolar coupling does not depend on the status of nitrogen magnetization, we did observe a dependence of the REDOR $\Delta S/S_0$ ratio on the ratio of ^1H decoupling to ^{15}N π pulse field. The optimal ratios were found between 3.3 and 3.9, which suggests that the cross-relaxation can be important for designing optimal REDOR experiments.

To find out whether the dependence of the REDOR dephasing ratio on decoupling field relates to the probed ^{13}C - ^{15}N distance, i.e., the dipolar coupling strength, we obtained the dephasing curve for two model compounds, 10% $1\text{-}^{13}\text{C}$, ^{15}N Glycine and FP-F8_CL9_N peptide, which have shorter ^{13}C - ^{15}N distances and stronger dipolar coupling than the MB(i+4)EK-A9_CA13_N peptide. The results in Figure 20 indicate that for both samples, the $\Delta S/S_0$ ratio does not differ greatly for ^1H decoupling field between 100 kHz and 65 kHz. This can not be explained by the number of nitrogen π pulses involved as shown in Figure 21, which compares the difference of $\Delta S/S_0$ ratio at different spinning speed for all three samples. In these experiments, the low speed is half as fast as the high speed and the rotor period is twice longer. Therefore, at low speed the experiment contains only half the number of nitrogen π pulses. The results (cf. Figure 21) indicate only small differences among the samples, which argues against the sensitivity to the number of nitrogen π pulses. The difference also can not be ascribed to the dephasing time, because when we compared the $\Delta S/S_0$ difference for 10% $1\text{-}^{13}\text{C}$, ^{15}N Glycine and MB(i+4)EK-A9_CA13_N peptide at comparable dephasing times, we observed significantly less $\Delta S/S_0$ ratio difference for the first sample. Therefore, the different dependence of REDOR dephasing ratio on decoupling field must relate to the strength of ^{13}C - ^{15}N dipolar coupling examined in the system.

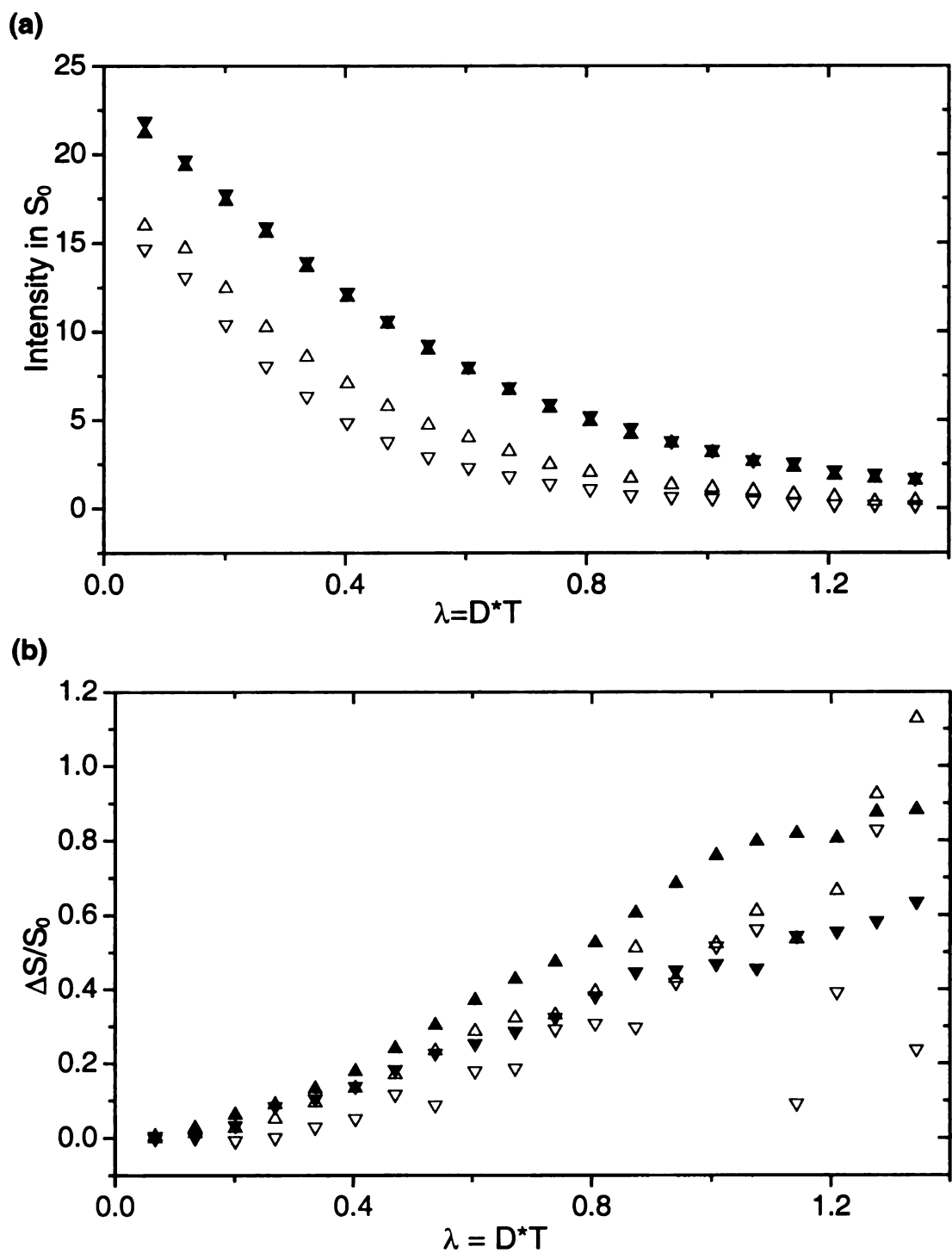


Figure 19. ^{13}C -observed REDOR (a) S_0 intensity and (b) calibrated $\Delta S/S_0$ for the MB(i+4)EK-A9 $_{\text{C}}$ A13 $_{\text{N}}$ peptide in the 4 mm rotor. A 42 Hz dipolar coupling D from a 4.2 Å ^{13}C - ^{15}N distance was applied. The filled and open triangles represent the results with TPPM and CW decoupling sequences, respectively. The upper (Δ) and lower (∇) triangles represent the results with 100 kHz and 70 kHz decoupling field, respectively.

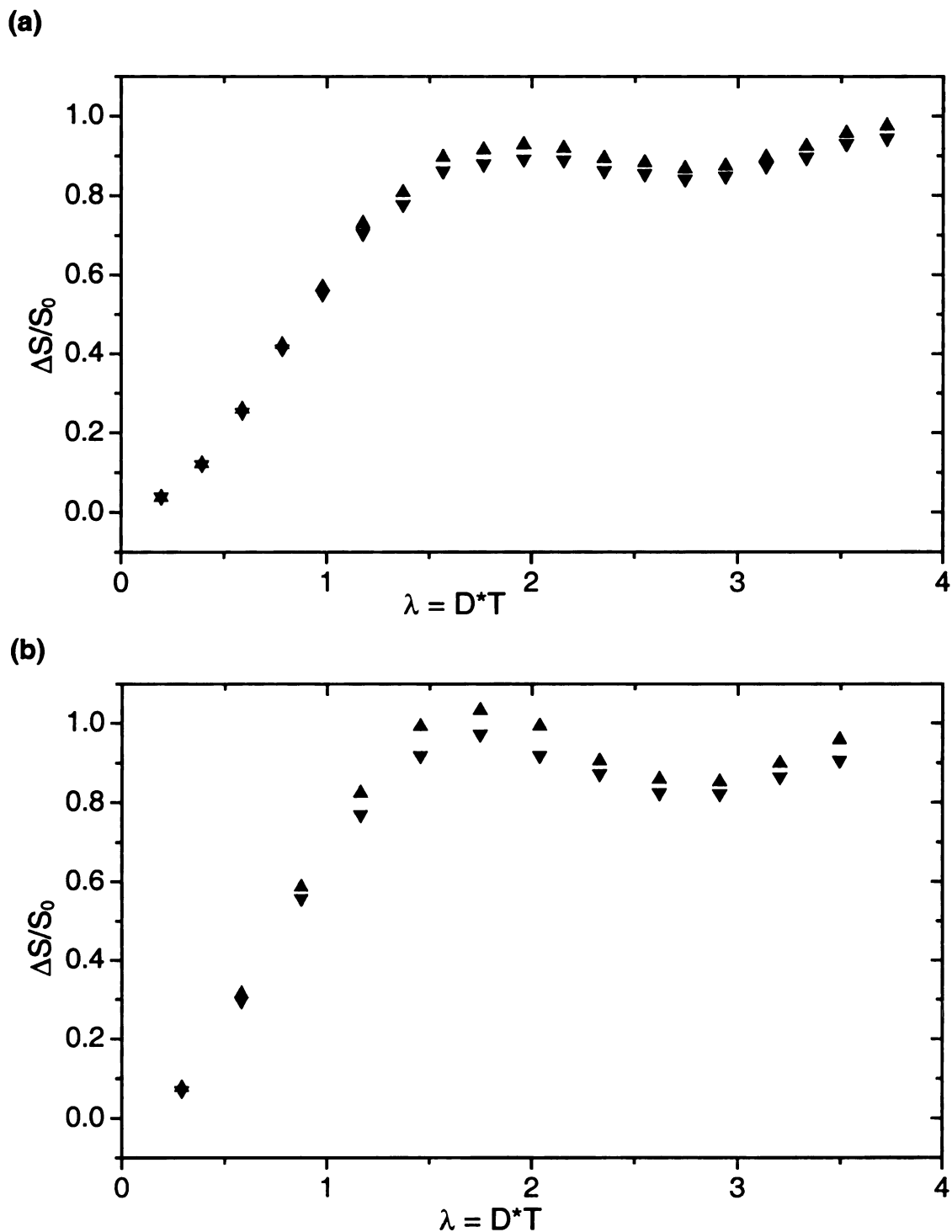


Figure 20. ^{13}C -observed REDOR calibrated $\Delta S/S_0$ for (a) 10% $1\text{-}^{13}\text{C}$, ^{15}N Glycine with 196 Hz dipolar coupling D (2.50 Å), and (b) FP-F8_CL9_N peptide with 1165 Hz dipolar coupling D (1.38 Å) in the 2/3 full 4 mm rotor. The upper (Δ) and lower (∇) triangles represent the results with 100 kHz and 65 kHz TPPM decoupling field, respectively.

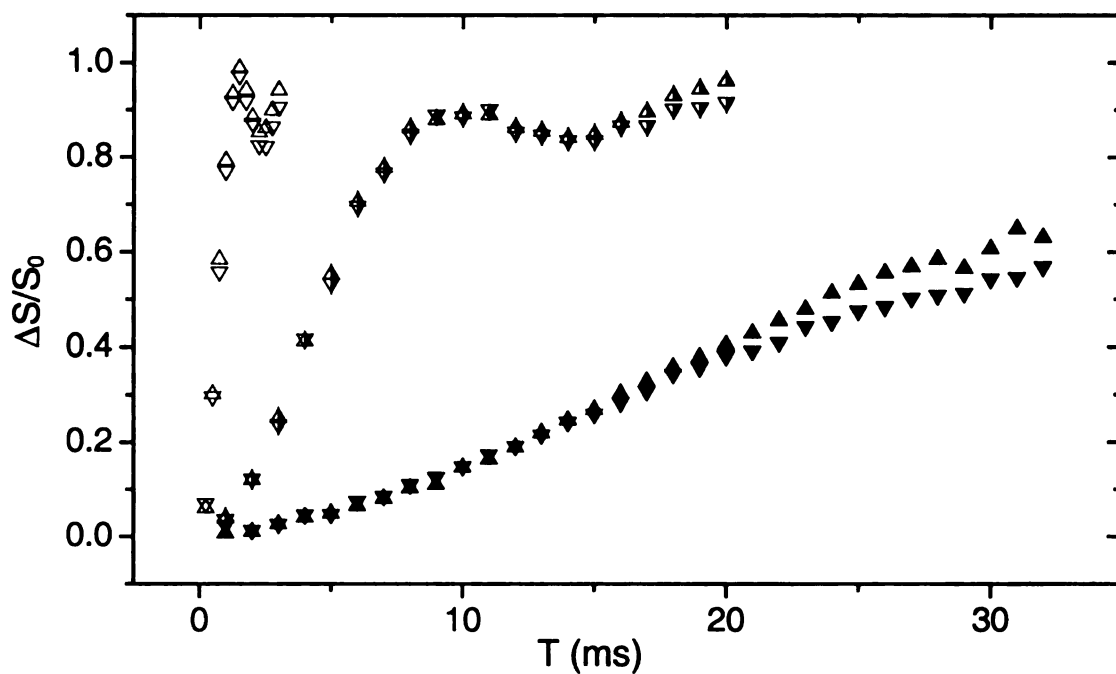


Figure 21. ^{13}C -observed REDOR calibrated $\Delta S/S_0$ for FP-F $_8\text{C}$ L $_9\text{N}$ peptide spinning at 16 kHz (open lower triangles) and 8 kHz (open upper triangles), 10% $1\text{-}^{13}\text{C}$, ^{15}N Glycine spinning at 16 kHz (half-filled lower triangles) and 8 kHz (half-filled upper triangles) (half-filled triangles), and MB(i+4)EK-A $_9\text{C}$ A $_{13}\text{N}$ peptide spinning at 8 kHz (filled lower triangles) and 4 kHz (filled upper triangles). All the experiments use 65 kHz TPPM decoupling. At each dephasing time for the same sample, the experiment running at lower speed contains half the amount of ^{15}N π pulses as the one at higher speed.

Selection of REDOR Sequences. Three commonly used REDOR pulse sequences are shown in Figure 22. All these REDOR experiments rely on application of two π pulses per rotor cycle and these could both be ^{15}N pulses (“all ^{15}N π pulse” version, Figure 22a)¹, one ^{15}N and one ^{13}C pulse (“alternating $^{15}\text{N}/^{13}\text{C}$ π pulse” version, Figure 22b)¹⁵ or both ^{13}C pulses (“all ^{13}C π pulse” version, Figure 22c)¹⁶. The all ^{15}N π pulse version is the original REDOR sequence. One of its potential problems is that the ^{13}C π pulse in the middle of the dephasing time is not only responsible for refocusing the ^{13}C magnetization, but also adds the dephasing from the second half of the dephasing time to the first half. If the pulse does not have the right length for a π pulse (e.g. a 170° or 190° pulse, instead), it will partially cancel the dephasing from the two halves. For example, a $\pi/2$ pulse will give only 50% of the dephasing as the π pulse. This problem can be significantly improved by the alternating $^{15}\text{N}/^{13}\text{C}$ π pulse version in which the central ^{13}C π pulse is replaced by a ^{13}C π pulse train using XY-8 phase-cycling scheme to compensate the possible width and phase errors of a single π pulse and eliminate off-resonance effects^{17, 18}. The all ^{13}C π pulse version is useful when the ^{15}N pulse imperfection can not be corrected easily, so putting all of the π pulses on the ^{13}C channel can improve the REDOR results. The problem with the latter two versions of REDOR is that the multiple ^{13}C π pulses may also refocus the homonuclear dipolar coupling and therefore reduce the overall intensity. The studies on 10% $1\text{-}^{13}\text{C}$, ^{15}N Glycine are good examples to illustrate the advantages and disadvantages of each REDOR version.

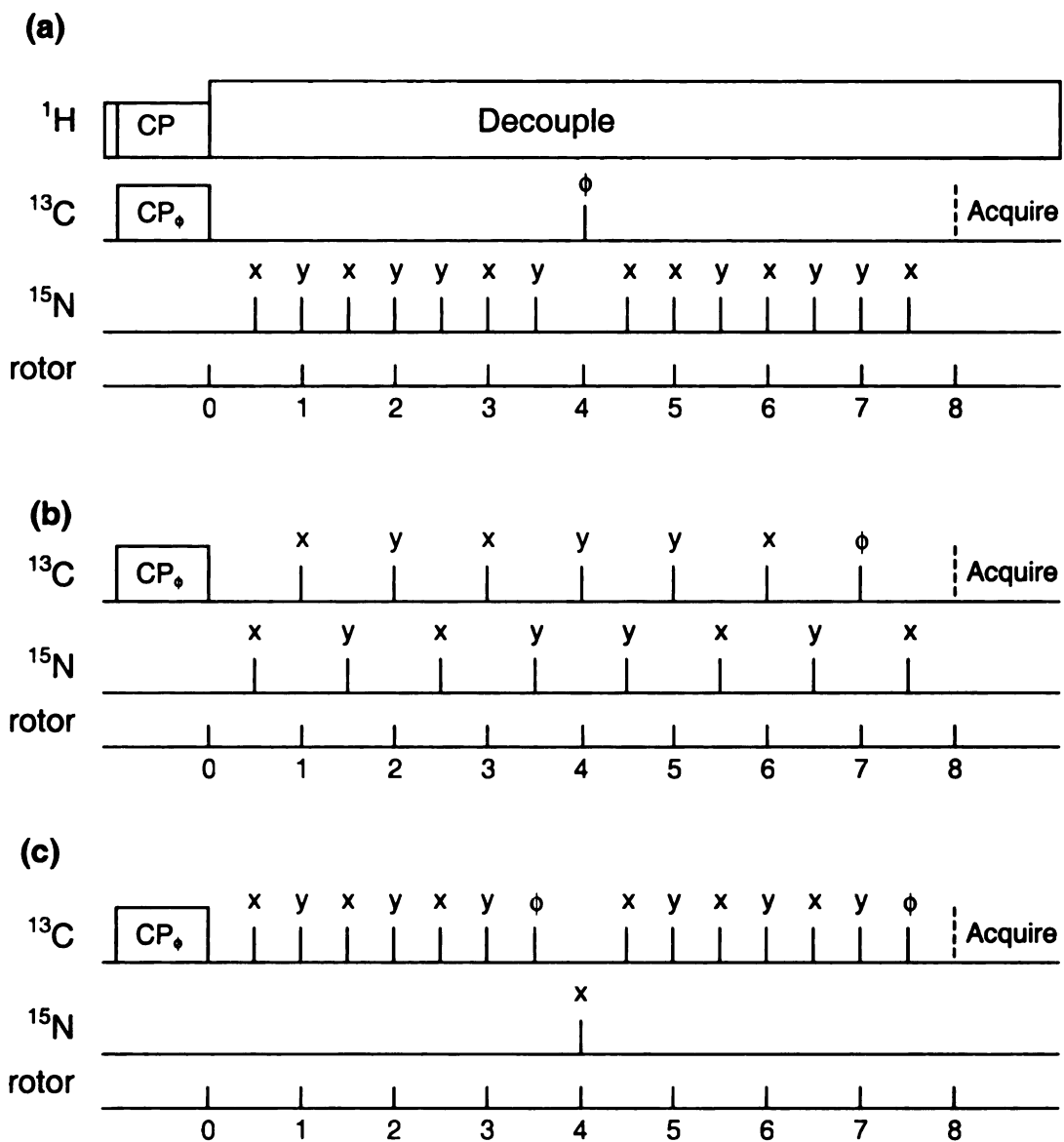


Figure 22. Three REDOR sequences with (a) “all ^{15}N π pulse” version, (b) “alternating $^{15}\text{N}/^{13}\text{C}$ π pulse” version, and (c) “all ^{13}C π pulse” version. XY-8 phase cycling is shown in (a) and (b) and XY-4 phase cycling is shown in (c).

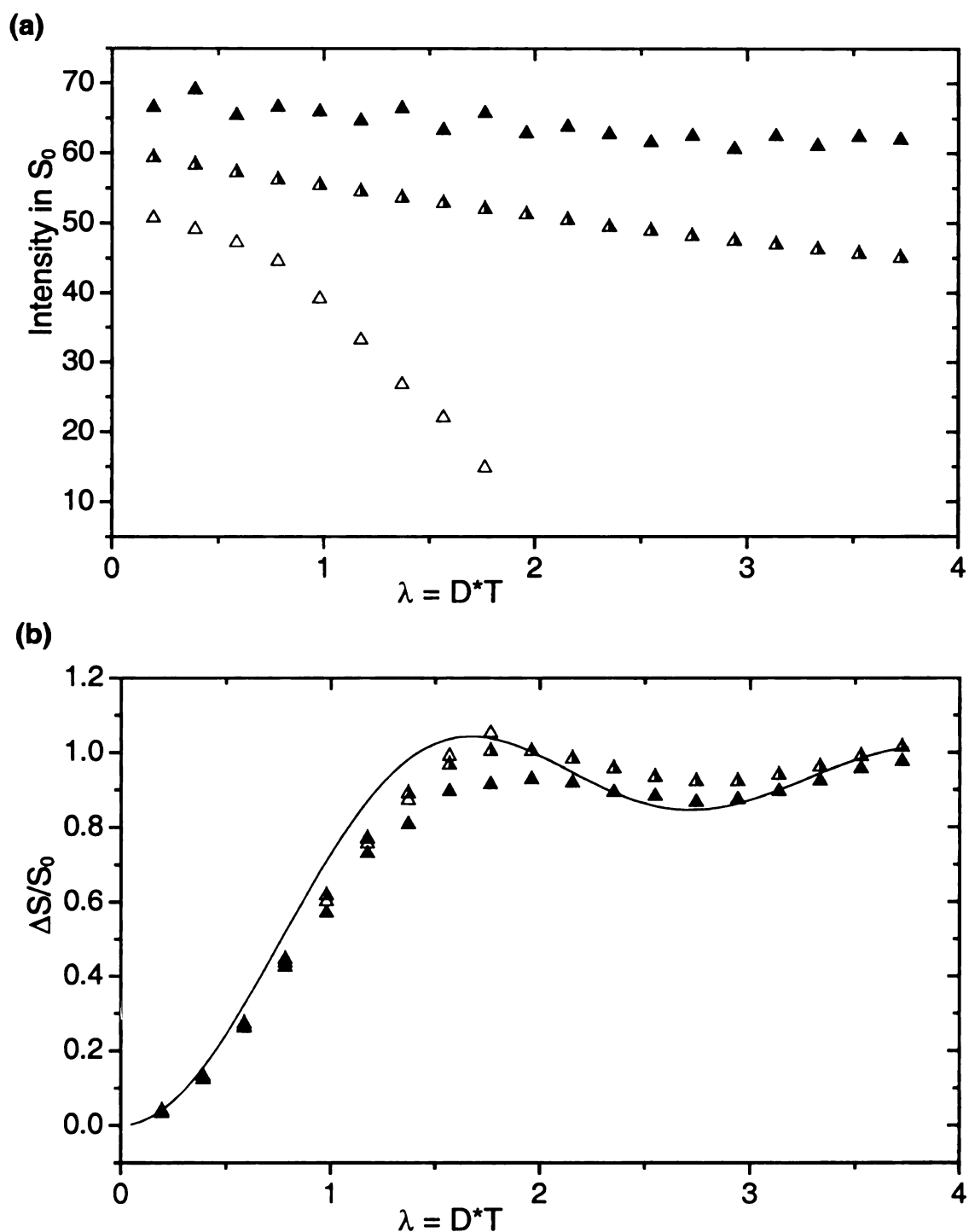


Figure 23. ^{13}C -observed REDOR (a) S_0 intensity and (b) calibrated $\Delta S/S_0$ for the 10% ^{13}C , ^{15}N Glycine in the 2/3 full 4 mm rotor with all ^{15}N π pulse version (filled triangles), alternating $^{15}\text{N}/^{13}\text{C}$ π pulse version (half-filled triangles), and all ^{13}C π pulse version (open triangles). All REDOR experiments use 100 kHz TPPM decoupling. In (b), a calculated REDOR dephasing curve based on 196 Hz dipolar coupling (2.50 Å ^{13}C - ^{15}N distance) is represented by the solid line.

Figure 23 compares the intensities in S_0 and calibrated $\Delta S/S_0$ using the three REDOR sequences. The decay of S_0 intensity as a function of dephasing time is governed by the spin-spin relaxation time T_2 , which can be different among different versions of REDOR sequences. In Figure 23a, the S_0 decays slowly with the all ^{15}N π pulse version because the T_2 time is longer, while in the other two versions, the magnetization decays faster because the T_2 time is significantly shorter presumably due to the reintroduction of ^{13}C - ^{13}C homonuclear dipolar coupling by the application of a π pulse train on the ^{13}C channel. In the all ^{13}C π pulse version, there is an additional factor that can reduce the intensity, the residual CSA that is not completely refocused due to the slight variation of spinning speed. In the first two REDOR sequences, the CSA is averaged out in each rotor period, so a little variation of the spinning speed is tolerable. In the all ^{13}C π pulse version, the CSA can be completely refocused only if the first half of the dephasing time is exactly the same length as the second half of the dephasing time, which requires a highly stable spinning speed. Obviously, the longer the dephasing time is, the harder it is to satisfy this requirement and thus the stronger the residual CSA. In experiments conducted at 8.000 ± 0.002 Hz, using the all ^{13}C π pulse version, the majority of the magnetization was lost after 10 ms dephasing time because of incomplete refocusing of the CSA. On the other hand, when we look at the REDOR $\Delta S/S_0$ ratio, the reduction of signal intensities due to residual CSA are cancelled in both S_0 and S_1 spectra and the advantage of applying XY-8 phase cycling on ^{13}C channel becomes dominant. The all ^{13}C π pulse version now gives the highest dephasing ratio. The significant improvement of the all ^{13}C π pulse over the all ^{15}N π pulse version is also consistent with the better ^{13}C pulse shape compared to the ^{15}N pulse shape.

The ultimate goal of REDOR studies on model compounds is to verify the validity of this technique. For this polycrystalline sample, we obtained a reasonably good fit when experimental results were compared with the theoretically calculated results based on data from its crystal structure. However, the polycrystalline morphology is not easily available for real samples, and the S_0 intensity in real samples may decay faster than Glycine which has an unusually long T_2 relaxation time probably due to the small number of protons in the molecule. It is therefore necessary to conduct studies on more realistic samples.

Using the all ^{15}N π pulse version, the REDOR results of the FP-F $_8\text{C}$ L $_9\text{N}$ peptide sample can be well fitted into a 1.38 Å ^{13}C - ^{15}N distance which matches the typical amide bond length (Figure 24). Since this short distance corresponds to a strong dipolar coupling (1165 Hz), the whole dephasing curve can be obtained with a small number of rotor periods and π pulses, the imperfection of pulses have minor effects, and the two decoupling fields show small differences.

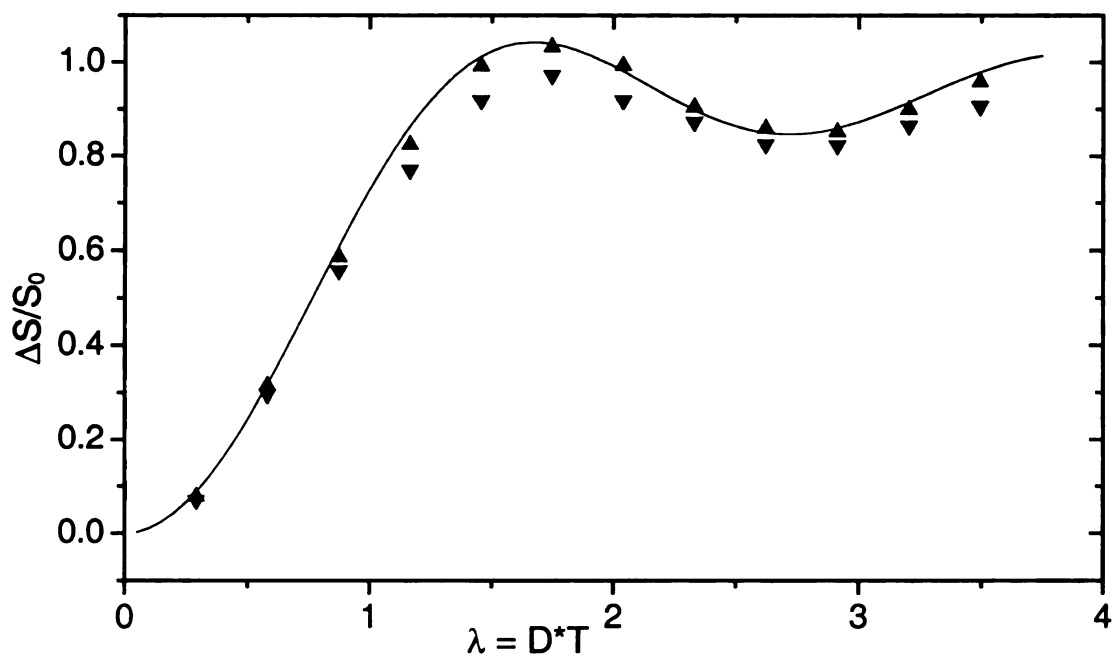


Figure 24. ^{13}C -observed REDOR calibrated $\Delta S/S_0$ for the FP-F8_CL9_N peptide in the 2/3 full 4 mm rotor using all ^{15}N π pulse version with 100 kHz (upper triangles) and 65 kHz (lower triangles) TPPM decoupling. The calculated REDOR dephasing curve based on 1165 Hz dipolar coupling (1.38 Å ^{13}C - ^{15}N distance) is represented by the solid line.

More challenging is the MB(i+4)EK-A9_CA13_N peptide that has a ¹³C-¹⁵N distance comparable to that of the real fusion peptide sample. The measurement of this sample is difficult in that the ¹³C-¹⁵N distance is longer (~ 4.2 Å) and the corresponding dipolar coupling is weaker (~ 42 Hz) and thus more π pulses are needed to build up the REDOR curve for quantitative analysis. Figure 25 displays the results of using the all ¹⁵N π pulse version at two TPPM decoupling fields (70 kHz and 100 kHz) and the alternating ¹⁵N/¹³C π pulse version at 65 kHz. Because of significant signal loss, the all ¹³C π pulse

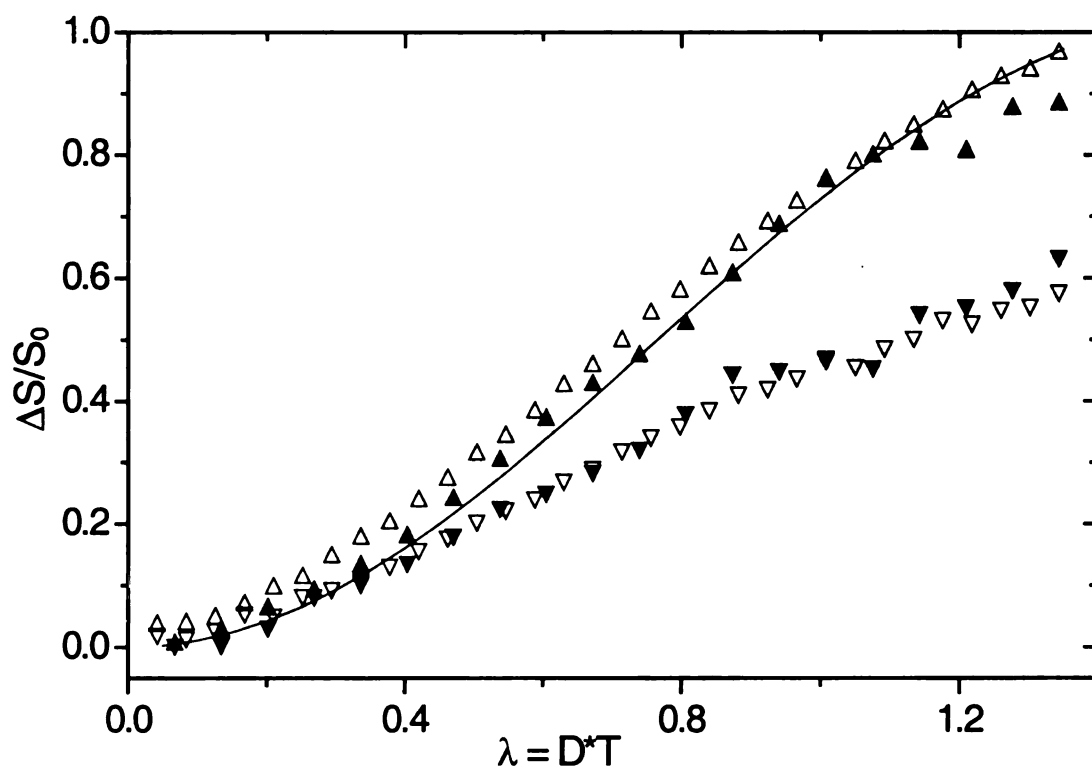
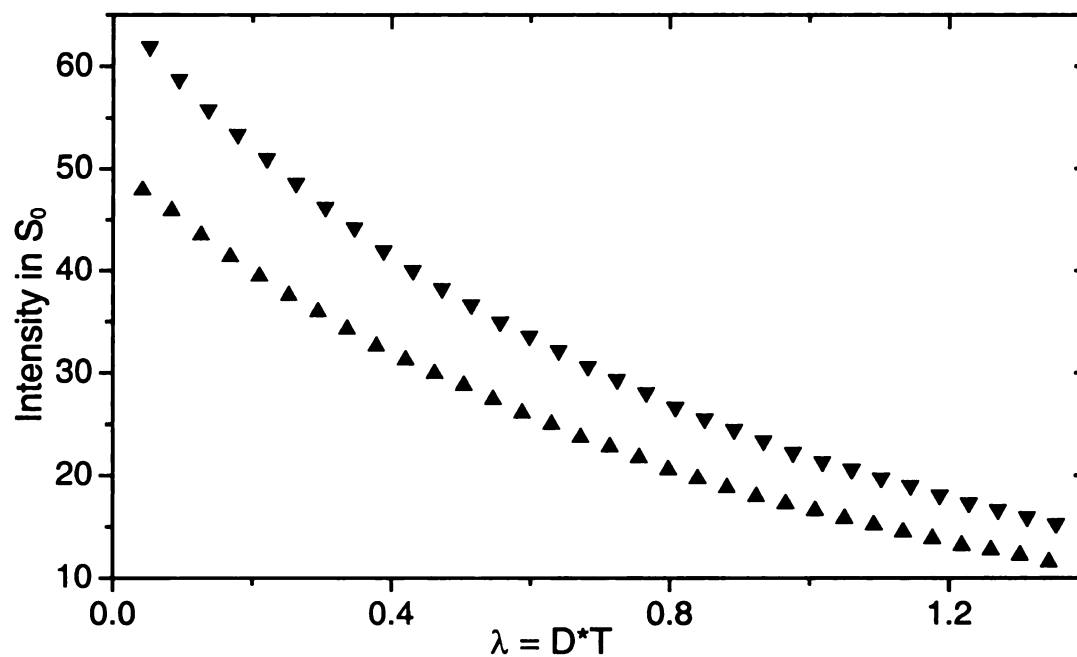


Figure 25. ¹³C-observed REDOR calibrated $\Delta S/S_0$ for the MB(i+4)EK-A9_CA13_N peptide in the 2/3 full 4 mm rotor (filled triangles) and 6 mm rotor (open triangles). All ¹⁵N π pulse version REDOR with 100 kHz (upper triangles) and 70 kHz (lower triangles) TPPM decoupling was used for the samples in the 4 mm rotor. All ¹⁵N π pulse version (lower triangles) and alternating ¹⁵N/¹³C π pulse version (upper triangles) REDOR with 65 kHz TPPM decoupling were used for the samples in the 6 mm rotor. The calculated REDOR dephasing curve based on 42 Hz dipolar coupling (4.20 Å ¹³C-¹⁵N distance) is represented by the solid line.

version can not be applied. These results demonstrate that we can obtain results close to the theoretical calculations with either high decoupling field or using the alternating $^{15}\text{N}/^{13}\text{C}$ π pulse REDOR sequence.

There is another interesting aspect associated with the alternating $^{15}\text{N}/^{13}\text{C}$ π pulse REDOR sequence when we use $8n$ or $8n + 2$ rotor periods (n is a natural number). The difference is that with $8n$ rotor periods we obtain a high $\Delta S/S_0$ ratio but with $8n + 2$ rotor periods we obtain high S_0 intensity as shown in Figure 26. The intuitive explanation is that this difference depends on whether the number of π pulses in a specific channel fulfills the complete XY-8 phase cycling. One would postulate that the phase cycling scheme in the ^{13}C channel determines the S_0 intensity while the phase cycling scheme in the ^{15}N channel determines the $\Delta S/S_0$ ratio. The XY-8 phase cycle was found to be a better choice than other phase cycles, e.g. XY-4 or XY-16. Therefore, the best result was obtained when an XY-8 phase cycle was completed in the channel. With $8n$ rotor periods, the ^{15}N channel has a complete XY-8 phase cycling so a better $\Delta S/S_0$ was obtained, while with $8n + 2$ rotor periods, the ^{13}C channel has a complete set of XY-8 phase cycling and a higher S_0 was observed. To verify this argument, we eliminated the first and last ^{15}N π pulses in the sequence so that when the rotor periods was set to $8n + 2$, both channels have completed the XY-8 phase cycling. However, similar results were observed when $8n$ or $8n + 2$ rotor periods were applied with this modified alternating $^{15}\text{N}/^{13}\text{C}$ π pulse REDOR sequence (data not shown). Therefore, the experimentally observed variations of the S_0 intensities and $\Delta S/S_0$ were not correlated with the completion of the XY-8 phase cycle scheme.

(a)



(b)

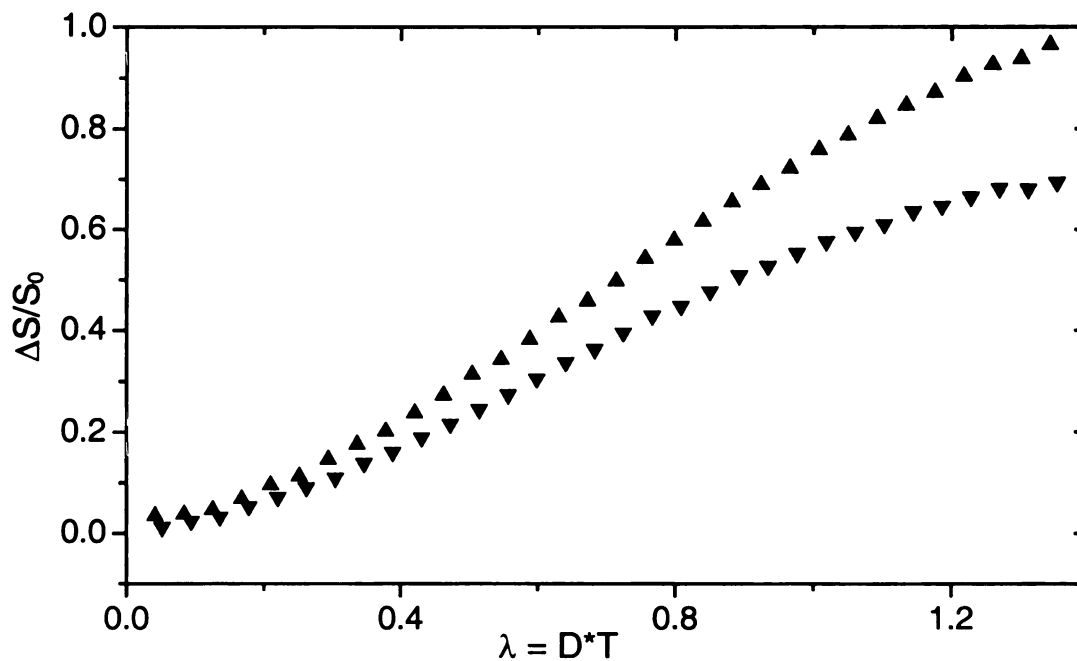


Figure 26. ^{13}C -observed REDOR (a) S_0 intensity and (b) calibrated $\Delta S/S_0$ MB(i+4)EK-A9 $_C$ A13 $_N$ peptide in the 2/3 full 6 mm rotor with alternating $^{15}\text{N}/^{13}\text{C}$ π pulse REDOR using $8n$ (upper triangles) and $8n + 2$ (lower triangles) rotor periods.

Although our results have verified that this technique can probe ^{13}C - ^{15}N distances comparable to hydrogen bonds (3.9 ~ 4.3 Å), it is not suitable for the sample system we probed. In practice, the 4 mm rotor can not hold enough sample to provide adequate signal-to-noise in reasonable amount of time. Also, in the real sample we have triply ^{13}C labeled peptide so that the strong homonuclear ^{13}C - ^{13}C coupling could reduce the intensity if the alternating $^{15}\text{N}/^{13}\text{C}$ π pulse REDOR sequence was used. Therefore analyses using the all ^{15}N π pulse REDOR with the 6 mm rotor are preferred. A fitting study was conducted to see whether the deviated REDOR curve can be fit into a single distance so that a calibration factor can be derived to reflect the real distance. Figure 27 displays the experimental results with 40 and 20 kHz ^{15}N π pulse fields, and obviously the latter gave better results. However, neither set yields a single distance, instead, they span a range of distances. The result of the lower ^{15}N π pulse field was collected after the measurements of membrane-associated fusion peptide samples, and to be consistent, we still focus on the result with the 40 kHz ^{15}N π pulse field. At ~ 24 ms dephasing time, the experimental results are best fitted with a 4.6 Å distance, which will be used to derive the calibration factor at the 24 ms dephasing time in the next chapter.

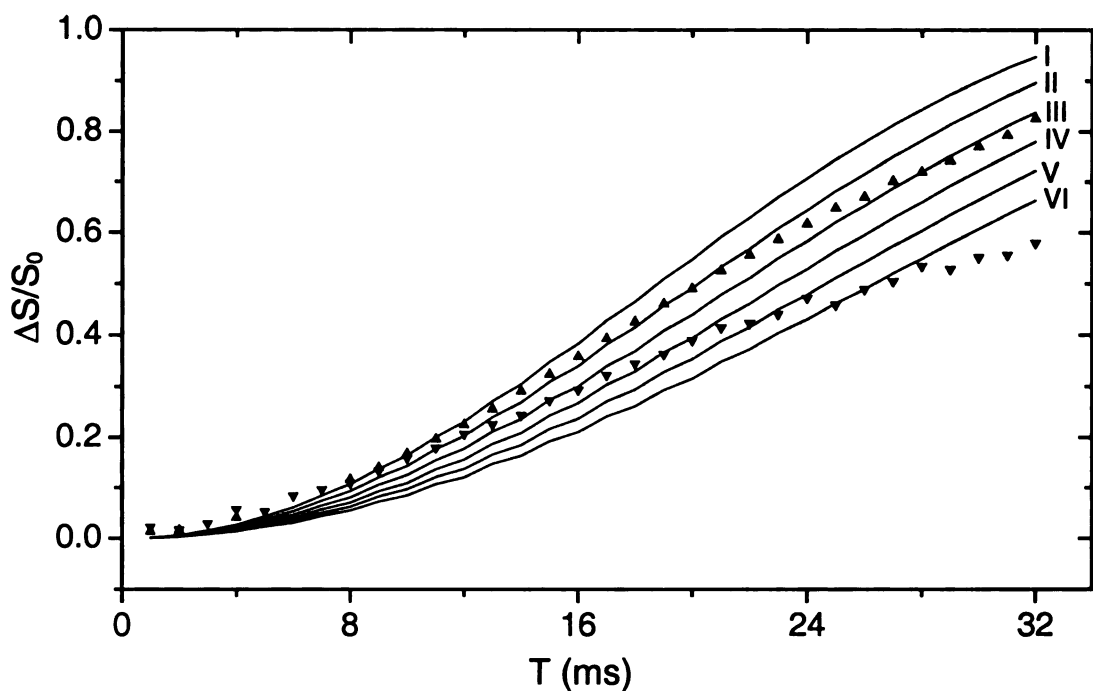


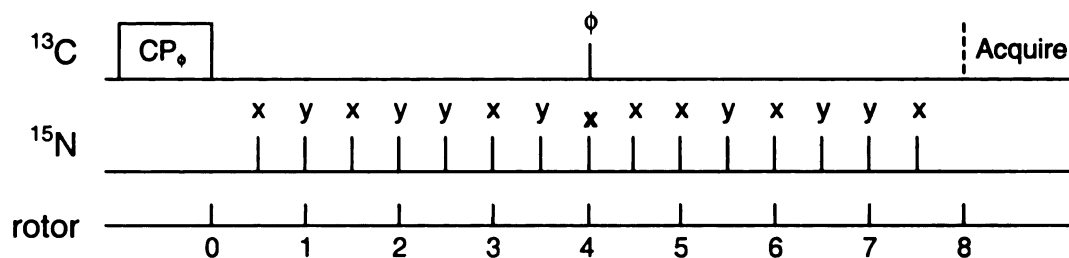
Figure 27. ^{13}C -observed REDOR calibrated $\Delta S/S_0$ for the MB(i+4)EK-A9C A13N peptide in the 2/3 full 6 mm rotor using 40 kHz ^{15}N π pulse field (lower triangles) and 20 kHz ^{15}N π pulse field (upper triangles). The all ^{15}N π pulse REDOR with 65 kHz TPPM decoupling was used. The calculated REDOR dephasing curves based on 4.2 Å (I), 4.3 Å (II), 4.4 Å (III), 4.5 Å (IV), 4.6 Å (V), and 4.7 Å (VI) ^{13}C - ^{15}N distances are represented by solid lines.



To find out whether we can combine the advantages of the first two versions of REDOR sequences, we designed a series of REDOR sequences in which the number of ^{15}N π pulses between ^{13}C π pulses was set to 1 (the alternating $^{15}\text{N}/^{13}\text{C}$ π pulse version), 3 and 47, respectively. The sequences were examined with a total of 192 rotor periods so that the corresponding numbers of additional ^{13}C π pulses to compensate pulse imperfection were 190, 94, and 6, respectively. The idea was to reduce the ^{13}C π pulses to a smaller number so that it would have less ^{13}C - ^{13}C recoupling than from the alternating $^{15}\text{N}/^{13}\text{C}$ π pulse version and still have better compensation of pulse imperfection than the single ^{13}C π pulse in the all ^{15}N π pulse version. As the results, with the 6 additional ^{13}C π pulses version we would expect higher S_0 intensity than that of the alternating $^{15}\text{N}/^{13}\text{C}$ π pulse version, and better $\Delta S/S_0$ than that of the all ^{15}N π pulse version. The experimental results showed that we did obtain an increase of the S_0 intensity with the 6 additional ^{13}C π pulses version, but the more important factor, $\Delta S/S_0$, was worse (0.34) than the result of the all ^{15}N π pulse version (~ 0.38). Therefore, the idea of reducing ^{13}C π pulses in the sequence does not give all the expected results. Other groups have reported using a total number of 8 π pulses in the observe channel (^{13}C channel in our case) to take advantage of both sequences^{19, 20}. We will conduct further studies to investigate this approach.

Considering that the all ^{15}N π pulse version has only one refocusing ^{13}C π pulse in S_0 and a large number of imperfect ^{15}N π pulses in S_1 , we wondered whether it is possible to compensate the ^{15}N pulse imperfection by incorporating these pulses in S_0 as shown below. Since the corresponding dephasing sequence S_1 is the same as the all ^{15}N π pulse

version, the new S_0 is different from S_1 only by the central ^{15}N π pulse which cancels the



accumulated ^{13}C - ^{15}N dipolar coupling from the first half of the dephasing period. Therefore the difference between S_0 and S_1 sequences is quite small as compared to the original all ^{15}N π pulse version where the numbers of ^{15}N π pulses are significantly different in the S_0 and S_1 sequences. However, further considerations suggest that this version should not give better results than the original one. The two versions have the same S_1 sequences and different S_0 sequences, so $\Delta S/S_0$ will only depend on the difference in S_0 between the two versions. In the modified S_0 sequence, only when the central ^{15}N π pulse is a perfect π pulse can the dipolar coupling be cancelled and give an S_0 intensity equals to the S_0 intensity in the original sequence where the dipolar coupling is not introduced at all. Any imperfection of the central ^{15}N π pulse will lead to the generation of residual dipolar coupling, which will reduce the S_0 intensity in the modified version, and thus reduce the $\Delta S/S_0$ ratio. This was indeed consistent with the experimental data. The result from the original sequence gave $\Delta S/S_0 = 0.38$, while the result from the modified sequence gave reduced S_0 and $\Delta S/S_0 = 0.28$.

The last thing we investigated was rotor synchronization. In the past we relied on the spinning controller to provide about 8.000 ± 0.002 kHz stability. The rotor period used in the experiment was calculated based on the speed setting, so the actual rotor

period can be slightly different from what was set. Active rotor synchronization detects the rotor spinning speed in real time and adjusts the rotor period accordingly so that the actual pulse timing matches better with the rotor timing. We implemented the active rotor synchronized version of all ^{15}N π pulse REDOR and alternating $^{15}\text{N}/^{13}\text{C}$ π pulse REDOR and compared with the corresponding original versions. Little difference was found regarding the $\Delta S/S_0$ ratio and S_0 intensity.

CONCLUSION

We conducted a series of REDOR experiments to verify the feasibility of this technique for measuring ^{13}C - ^{15}N distance in a peptide. The goal is to detect hydrogen bonded ^{13}C - ^{15}N pairs through a 40 Hz coupling which requires a dephasing period of 10 ~ 30 ms duration and hundreds of NMR π pulses in the REDOR experiment. We therefore expended some effort in optimizing the experiment settings including the quality of π pulse, ^1H decoupling sequence and strength, and selection of REDOR sequence.

Pulse imperfections were found in the ^{15}N channel that were not solely due to the pulse shape. Also, samples placed at outmost 1/3 layer of the rotor experience significantly less RF field as compared to that of the central 2/3 layer and give worse REDOR results. This situation is especially poor for a 4 mm rotor. For quantitative analysis, sample should be restricted into the central 2/3 layer of the rotor.

Although the REDOR experiment should in principle involves only two channels, adequate proton decoupling is essential to remove the strong proton dipolar coupling and preserve the ^{13}C magnetization during the dephasing time. To accomplish this goal, the

TPPM decoupling sequence was found to be superior relative to regular CW decoupling. A higher decoupling field also gives significantly better REDOR dephasing ratio, at least when a longer heteronuclear distance is probed. It is also important to make the proton decoupling field at least three times greater than the dilute spin field to avoid the cross-relaxation effect.

In general, the alternating $^{15}\text{N}/^{13}\text{C}$ π pulse REDOR with XY-8 phase cycling scheme in both channels provides a better way to suppress offset effects and compensate for pulse imperfections, and gives better results than the all ^{15}N π pulse REDOR. The all ^{13}C π pulse REDOR also gives better $\Delta S/S_0$ ratio than the all ^{15}N π pulse REDOR probably due to the better pulse perfection in ^{13}C than in ^{15}N . However, the oversensitivity to rotor spinning stability reduces the intensity rapidly with an increase in the dephasing time; thus, this REDOR version is of little use for probing weak dipolar coupling where a long dephasing time is necessary.

Considering the requirements of our real sample, it is preferable to use a 6 mm rotor to obtain adequate signal-to-noise in a reasonable amount of time and the decoupling field is restricted to 65 kHz. Also, since we have adjacent triply labeled ^{13}C carbonyls in the same peptide, the all ^{15}N π pulse REDOR was chosen over the alternating $^{15}\text{N}/^{13}\text{C}$ π pulse REDOR to avoid ^{13}C - ^{13}C homonuclear dipolar coupling that will attenuate the signal. Using these conditions, we obtained a REDOR dephasing curve smaller than theoretical calculation. In our study, REDOR was used as a semi-quantitative probe of extent of hydrogen bonding, and therefore the results with all ^{15}N π pulse REDOR and 65 kHz TPPM decoupling were used for calibration in the study of membrane-associated fusion peptide.

REFERENCE

1. Gullion, T., and Schaefer, J. (1989) Rotational-echo double-resonance NMR. *J. Magn. Reson.* *81*, 196-200.
2. Hing, A. W., Tjandra, N., Cottam, P. F., Schaefer, J., and Ho, C. (1994) An investigation of the ligand-binding site of the glutamine-binding protein of *Escherichia coli* using rotational-echo double-resonance NMR. *Biochemistry* *33*, 8651-8661.
3. Gullion, T. (1998) Introduction to rotational-echo, double-resonance NMR. *Concepts Magn. Reson.* *10*, 277-289.
4. Middleton, D. A., Ahmed, Z., Glaubitz, C., and Watts, A. (2000) REDOR NMR on a hydrophobic peptide in oriented membranes. *J. Magn. Reson.* *147*, 366-370.
5. Jaroniec, C. P., Tounge, B. A., Herzfeld, J., and Griffin, R. G. (2001) Frequency selective heteronuclear dipolar recoupling in rotating solids: Accurate C-13-N-15 distance measurements in uniformly C-13,N-15-labeled peptides. *J. Am. Chem. Soc.* *123*, 3507-3519.
6. Murphy, O. J., 3rd, Kovacs, F. A., Sicard, E. L., and Thompson, L. K. (2001) Site-directed solid-state NMR measurement of a ligand-induced conformational change in the serine bacterial chemoreceptor. *Biochemistry* *40*, 1358-1366.
7. Thompson, L. K. (2002) Solid-state NMR studies of the structure and mechanisms of proteins. *Curr. Opin. Struct. Biol.* *12*, 661-669.
8. Long, H. W., and Tycko, R. (1998) Biopolymer conformational distributions from solid-state NMR: alpha-helix and 3(10)-helix contents of a helical peptide. *J. Am. Chem. Soc.* *120*, 7039-7048.
9. Gullion, T., Baker, D. B., and Conradi, M. S. (1990) New, compensated Carr-Purcell sequences. *J. Magn. Reson.* *89*, 479-484.
10. Gullion, T., and Schaefer, J. (1991) Elimination of resonance offset effects in rotational-echo, double-resonance NMR. *J. Magn. Reson.* *92*, 439-442.
11. Mehta, A. K., Hirsh, D. J., Oyler, N., Drobny, G. P., and Schaefer, J. (2000) Carbon-proton dipolar decoupling in REDOR. *J. Magn. Reson.* *145*, 156-158.
12. Ishii, Y., Ashida, J., and Terao, T. (1995) ¹³C-¹H dipolar recoupling dynamics in ¹³C multiple-pulse solid-state NMR. *Chem. Phys. Lett* *246*, 439-445.

13. Mitchell, D. J., and Evans, J. N. S. (1998) Improved heteronuclear decoupling in REDOR with the use of TPPM. *Chem. Phys. Lett.* 292, 656-660.
14. Bennett, A. E., Rienstra, C. M., Auger, M., Lakshmi, K. V., and Griffin, R. G. (1995) Heteronuclear decoupling in rotating solids. *J. Chem. Phys.* 103, 6951-6958.
15. Anderson, R. C., Gullion, T., Joers, J. M., Shapiro, M., Villhauer, E. B., and Weber, H. P. (1995) Conformation of [1-C-13,N-15]Acetyl-L-Carnitine - rotational-echo, double-resonance nuclear-magnetic-resonance spectroscopy. *J. Am. Chem. Soc.* 117, 10546-10550.
16. Garbow, J. R., and Gullion, T. (1991) Improvements in REDOR NMR spectroscopy - minimizing resonance-offset effects. *J. Magn. Reson.* 95, 442-445.
17. Mehta, A. K., personal communication.
18. McDowell, L. M., Poliks, B., Studelska, D. R., O'Connor, R. D., Beusen, D. D., and Schaefer, J. Rotational-echo double-resonance NMR-restrained model of the ternary complex of 5-enolpyruvylshikimate-3-phosphate synthase. *J. Biomol. NMR*, in press.
19. O'Connor, R. D., and Schaefer, J. (2002) Relative CSA-dipolar orientation from REDOR sidebands. *J. Magn. Reson.* 154, 46-52.
20. O'Connor, R. D., Poliks, B., Bolton, D. H., Goetz, J. M., Byers, J. A., Wooley, K. L., and Schaefer, J. (2002) Chain packing in linear phenol-polycarbonate by C-13{H-2} REDOR. *Macromolecules* 35, 2608-2617.

CHAPTER VI

**OLIGOMERIZATION STUDIES OF THE MEMBRANE-ASSOCIATED FUSION
PEPTIDE BY REDOR MEASUREMENTS: PARALLEL VS. ANTI-PARALLEL
STRAND ARRANGEMENTS**

BACKGROUND

In the previous chapters, we demonstrated that the free HIV-1 fusion peptide can serve as a useful model system for understanding viral/target cell fusion, at least to the lipid mixing stage. Recent studies suggest that envelope protein regions other than the fusion peptide also interact with membranes and play a role in fusion¹⁻⁶.

For the HIV-1 gp41 envelope proteins, there are atomic-resolution structures of the “soluble ectodomains” which do not contain the fusion peptide⁷⁻¹¹ (cf. Figure 28). These structures are believed to correspond to the protein conformations after fusion has occurred and perhaps during fusion as well. In each of these soluble ectodomain structures, the protein is trimeric and its three N-termini (corresponding to about residue 30 in the whole envelope protein) are in close proximity at the end of an in-register helical coiled-coil. These structures end several residues C-terminal of the fusion peptide and it has therefore been hypothesized that during viral/target cell fusion, at least three

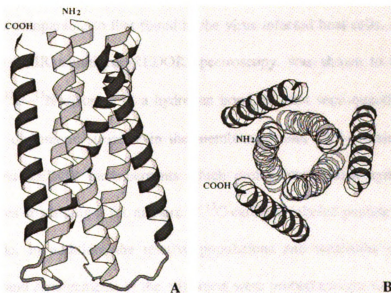


Figure 28. Structure of the gp41 soluble ectodomain trimer. (A) Ribbon drawing of the trimer. (B) An end-on view looking down the 3-fold axis of the trimer.

fusion peptides insert into the target cell membrane with their C-termini in close proximity.

There are fluorescence and ESR data suggesting that the fusion peptides form oligomeric structures¹²⁻¹⁴. The possible significance of fusion peptide oligomerization is suggested both by envelope protein trimerization and by experiments and modeling studies which indicate that the fusion site contains multiple trimers and a corresponding high fusion peptide concentration^{9, 10, 15-17}. In addition, the functionally disruptive Val-2 to Glu-2 mutation in the gp41 fusion peptide is trans-dominant, i.e. cells expressing 10% mutant protein and 90% wild-type protein exhibit only 40% of the fusion activity of cells with 100% wild-type protein¹⁸. One interpretation of these data is that the mutant peptide disrupts the correct assembly of a functionally important fusion peptide oligomer^{13, 14}.

In chapter three and four, we described the solid-state NMR studies on the HIV-1 fusion peptide and demonstrated that the peptide adopts a predominantly β strand structure when associated with membranes whose lipid head group and cholesterol composition is comparable to that found in the virus infected host cells. In chapter five, the solid-state NMR technique, REDOR spectroscopy, was shown to be feasible for detecting the ^{13}C - ^{15}N distance in a hydrogen bond, at least semi-quantitatively. In the present study, oligomeric structure in the membrane-bound HIV-1 fusion peptide was investigated via REDOR measurements which probe inter-peptide hydrogen bonding through samples containing a 1:1 mixture of ^{13}C carbonyl labeled peptide and ^{15}N amide labeled peptide. In addition, the relative populations and structures of parallel and antiparallel strand arrangements in the oligomers were probed using a variety of samples which differed by the residue positions of the ^{13}C labeling in one peptide and/or the ^{15}N

labeling in the other peptide. The REDOR experiments demonstrate the presence of a large population of membrane-associated fusion peptide oligomers with approximately equal weighting of parallel and antiparallel strand arrangements.

MATERIALS AND METHODS

Solid-State NMR Sample Preparation. The samples were prepared using method 1. In brief, peptide was dissolved in ~ 35 ml of 5 mM HEPES, pH 7.0. Peptide concentrations were determined by the BCA assay which had been calibrated using quantitative amino acid analysis. For samples containing two differently labeled peptides, each peptide was dissolved separately and the two solutions were then combined. Two kinds of lipid/cholesterol mixtures reflecting the approximate lipid and cholesterol content of the HIV-1 virus and its target T-cells were used: LM-3 had POPC, POPE, POPS, sphingomyelin, PI and cholesterol in a 10:5:2:2:1:10 molar ratio, and LM-4 had the same components except the POPC was replaced by DPPC-1-¹³C. LUVs of LM-3 or LM-4 were prepared in ~ 2 ml buffer. The peptide and LUV solutions were then mixed and kept at room temperature overnight to ensure maximum peptide/lipid binding. Subsequent ultracentrifugation of the solution at 100,000 × g for four hours pelleted the membrane and associated bound peptide, and left unbound peptide in the supernatant. Peptide binding was typically quantitative as determined by BCA assay measurements of negligible peptide concentration in the supernatant. The peptide/lipid pellet formed after ultracentrifugation was transferred by spatula to a 6 mm diameter MAS NMR rotor.

Solid-State NMR Spectroscopy. Experiments were done on the 9.4 T Varian Infinity Plus spectrometer using a 6 mm triple resonance MAS probe. The detection

channel was tuned to ^{13}C , the decoupling channel was tuned to ^1H , and the third channel was tuned to ^{15}N . ^{13}C and ^{15}N chemical shifts were externally referenced to the methylene resonance of adamantane at 38.2 ppm and $(\text{NH}_4)_2\text{SO}_4$ at 20 ppm, respectively. Experiments used a MAS frequency of 8.000 ± 0.002 kHz. In the NMR probe circuit, the RF fields are attenuated at the ends of the coil. Hence, for the FPK3 samples, longer spacers were used to restrict samples to the 2/3 central volume (~ 160 μl). For the other samples, the full volume of the rotor was used. Because the comparison of these two volumes in 6 mm rotor showed negligible difference, direct comparison could be made between all of the samples. The chief advantage of the volume restriction is lower sample requirement.

In REDOR experiments to detect hydrogen bonds, between 1 and 2 ms of CP at 50 kHz was followed by a 24.0 ms dephasing period and then direct ^{13}C detection. The all ^{15}N π pulse REDOR was applied with a single 50 kHz ^{13}C refocusing π pulse was placed at the center of the dephasing period and ^1H TPPM decoupling of 65 kHz was applied during both dephasing and detection. The ^{13}C transmitter was set to 155 ppm and the ^{15}N transmitter was set to 115 ppm. For the S_1 acquisition, the dephasing period contained a 40 kHz ^{15}N π pulse at the middle and end of each rotor cycle, while the S_0 acquisition did not contain these pulses. XY-8 phase cycling was used for the ^{15}N pulses.

The spectrometer parameters were optimized with the lyophilized MB(i+4)EK-A9_CA13_N model helical peptide as described in chapter five. The data were processed with 100 Hz line broadening and with fifth order polynomial baseline correction.

REDOR Data Analysis and Simulations. The experimental $\Delta S/S_0$ is obtained following the equation 4. In addition, for each pair of S_0/S_1 spectra, an experimental

uncertainty σ was calculated as the root-mean-squared-deviation of integrated intensities in twenty-four regions of the spectra without signal. $\sigma_{\Delta S/S_0}$, the uncertainty in $\Delta S/S_0$, was calculated using the formula¹⁹:

$$\sigma_{\Delta S/S_0} = \sigma \times S_1/S_0 \times \sqrt{(1/S_0)^2 + (1/S_1)^2} \quad (6)$$

Simulations of the REDOR experiment were carried out as a function of peptide structure and dephasing period using the SIMPSON program²⁰. The experimental pulse sequence, MAS frequency, ¹³C and ¹⁵N RF fields and pulse lengths, and ¹⁵N phases were incorporated into the simulations. Carbonyl chemical shift anisotropy (CSA) principal values were set to be 250, 190, and 90 ppm, and the principal axis directions were taken from the literature with the following orientations: δ_{33} perpendicular to the peptide plane and δ_{22} at an angle $\chi = 130^\circ$ from the C–N bond²¹. ¹H were not considered in the simulations.

RESULTS

REDOR Simulations of Multiple ¹⁵N Coupled to ¹³C. Although it is possible to obtain the numeric calculation of REDOR dephasing ratio accurately based on equation 5 for a single ¹³C–¹⁵N pair, it is difficult to calculate the result when one ¹³C is coupled to multiple ¹⁵N nuclei, as is the case in the real peptide samples. The SIMPSON program, a simulation program for solid-state NMR was applied to provide information about the multiple coupled REDOR dephasing ratio.

First we compared the result of single ¹³C–¹⁵N pair from SIMPSON with that from a previous numeric calculation and a satisfying agreement was observed in Figure 28, indicating that the program can be used for further investigation. The simulated

REDOR dephasing curves were found approximately independent of the carbonyl CSA principal axis geometry, which is also consistent with the simulations in other studies²².

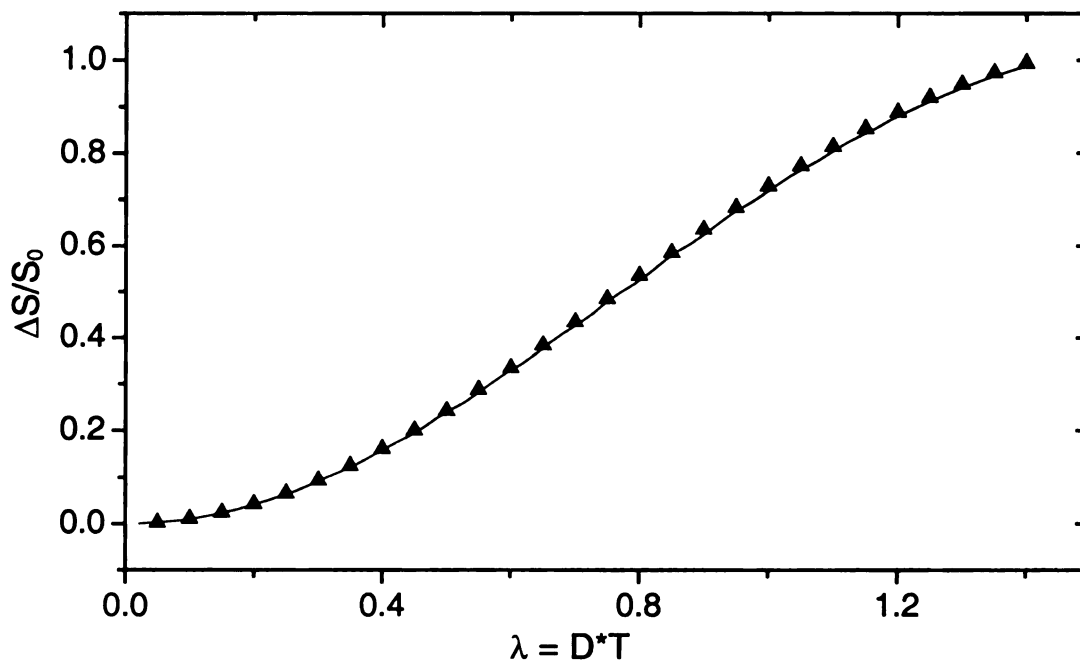


Figure 29. REDOR simulation from the SIMPSON program (triangles) and numeric calculation (solid line). A 44.4 Hz dipolar coupling D (4.1 Å) was used in both cases.

Next we calculated the case where one ^{13}C is coupled not only to the hydrogen bonded ^{15}N , but also to the adjacent two other ^{15}N as in the case of triply ^{15}N labeled fusion peptide samples. Since we are probing the possible hydrogen bonds among peptides forming parallel or anti-parallel beta sheets, the simulation was conducted with the coordinates from the crystal structure of the parallel and anti-parallel segments of streptococcal protein G B1 domain (PDB file 1igd)²³. Each simulation also used a defined register of the ^{13}C and ^{15}N labeled residues in neighboring strands. Figure 29 shows that according to the typical structure of parallel or anti-parallel arrangements, ^{13}C that couples with two additional adjacent ^{15}N generally experiences more dephasing than if it only dephases by the hydrogen bonded ^{15}N (open symbols). Not surprisingly we also found little difference exists between parallel and anti-parallel arrangements since the two geometries are quite similar. To get a more realistic estimate, we expanded the typical hydrogen bond distance from 4.1 Å to 4.6 Å based on the REDOR result of the MK(i+4)-A9_CA13_N peptide and expanded the other two ^{13}C - ^{15}N distances in parallel or anti-parallel arrangements with the same ratio (4.6/4.1) and redid the simulation. The filled symbols in Figure 29 are the corresponding results. Again we found similar results as with the regular distances. Using these results, at 24 ms dephasing time, we would obtain a dephasing ratio of ~ 0.5 exclusively for the ^{13}C coupled to three ^{15}N , which will be used for the semi-quantitative analysis in real samples.

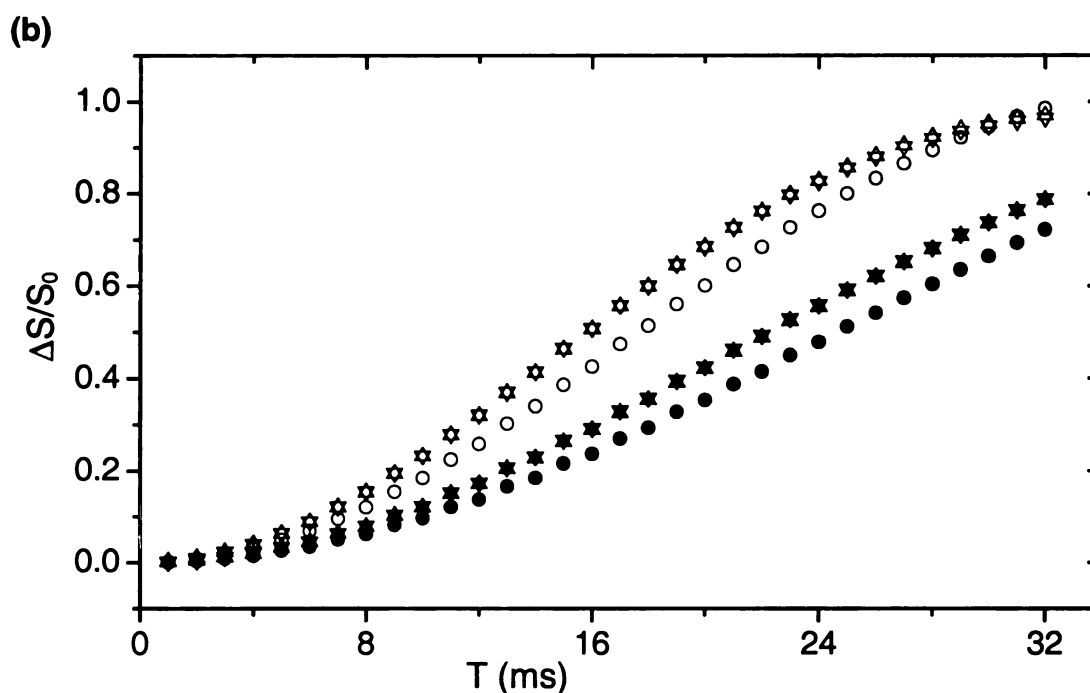
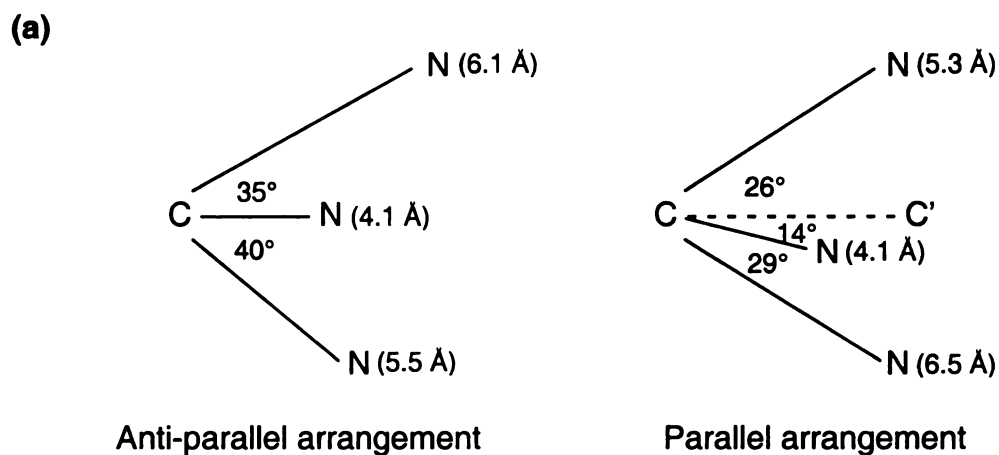


Figure 30. (a) Coordinates of one ^{13}C coupled to three adjacent ^{15}N in parallel and anti-parallel segments of streptococcal protein G B1 domain with the carbonyl carbon hydrogen bonded to the middle amide nitrogen. (b) SIMPSON simulated REDOR dephasing ratios of the ^{13}C dephased by only hydrogen bonded ^{15}N (open circles), or two more adjacent ^{15}N in parallel strand arrangement (open upper triangles), or two more adjacent ^{15}N in anti-parallel strand arrangement (open lower triangles). The filled symbols represent the corresponding simulation results when all the distances are extended by a factor of 4.6/4.1 as the hydrogen bond distance expands from 4.1 Å to 4.6 Å based on the REDOR result of MK(i+4)-A9_CA13_N peptide at 24 ms dephasing time.

REDOR Control Experiments. We have discussed the optimization of the REDOR experiment in Chapter V. One important reason to choose the all ^{15}N π pulse REDOR is the consideration of sensitivity when the sample contains triply ^{13}C labeled peptide. Figure 30 demonstrates that using this version of REDOR on such a sample, the S_0 signal at 24.0 ms dephasing time was about 1/8 that obtained with direct CP. With the alternating $^{13}\text{C}/^{15}\text{N}$ π pulse version of REDOR, there was additional attenuation by a factor of ~ 0.6 , which may be a result of π pulse recoupling of ^{13}C - ^{13}C homonuclear interactions²⁴⁻²⁶. In our study, REDOR was used as a semi-quantitative probe of the extent of hydrogen bonding, and we chose to use the higher signal-to-noise all ^{15}N π pulse REDOR. In general, as the dephasing period increases, $\Delta S/S_0$ also increases, whereas the overall signal decreases. The chosen 24.0 ms dephasing period represents a compromise between these two competing effects.

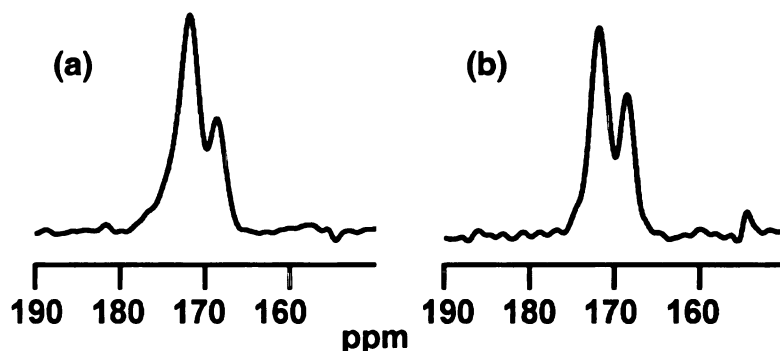


Figure 31. ^{13}C solid-state NMR spectra of the FPK3-(G5A6L7)_C/FPK3-(A14A15G16)_N/LM-3 sample from (a) CP experiment and (b) S_0 REDOR experiment with a 24.0 ms dephasing time. The spectral intensities in each experiment were divided by the number of scans in that experiment. The vertical scale in (b) is 8 times that in (a), showing that the signal/scan in (b) is $\sim 1/8$ as large as that in (a). The (b) spectrum appears better resolved than the (a) spectrum because the natural abundance lipid carbonyls make a relatively smaller contribution to the S_0 signal than to the CP signal.

Table 9 lists $\Delta S/S_0$ values from a series of REDOR control experiments and Figure 31 displays some of the corresponding experimental spectra. The goal of the control experiments was to quantify $(\Delta S/S_0)_{\text{background}}$, representing the dephasing ratio in the membrane-associated peptide samples that was not due to the labeled ^{13}C - ^{15}N hydrogen bonded pairs. For samples containing only ^{13}C labeled and/or natural abundance peptide (cf. Figure 31a and 31e), the $\Delta S/S_0$ value is in the $-0.01 \sim 0.03$ range and is due to the 0.0037% ^{15}N natural abundance and the resulting small population of carbonyls with nearby ^{15}N . For example, a ^{13}C with ^{15}N one or two bonds away on the peptide backbone will have an individual $\Delta S/S_0 \approx 1$ at 24.0 ms dephasing time. For a sample containing a 1:1 mixture of ^{15}N labeled and unlabeled peptide (cf. Figure 31b), $\Delta S/S_0 \sim 0.2$, while for a sample containing only ^{15}N labeled peptide, $\Delta S/S_0 \sim 0.4$. These relatively large $\Delta S/S_0$ values are likely a result of the significant fraction of natural abundance carbonyls which are close to the labeled ^{15}N . For the samples used to probe fusion peptide strand arrangements, there was a 1:1 mixture of ^{13}C and ^{15}N labeled peptides and a $\sim 10\%$ natural abundance peptide contribution to the total ^{13}C signal. In these samples, we would expect therefore a ~ 0.02 contribution to $\Delta S/S_0$ from natural abundance peptide ^{13}C .

In samples containing 50% ^{13}C carbonyl labeled lipid (“LM-4”) and either ^{15}N labeled peptide or unlabeled peptide, $\Delta S/S_0 \sim 0.03$ or 0.01, respectively (cf. Figure 3d). In addition, when CP and S_0 intensities of these samples were compared to those of samples containing unlabeled lipid and ^{13}C labeled peptide, it was observed that the CP signal per ^{13}C is about three times less for a lipid carbonyl than for a peptide carbonyl while the S_0 signal per ^{13}C is about nine times less for a lipid carbonyl than for a peptide carbonyl. By

combining this latter result with the observation that $\Delta S/S_0 \sim 0.4$ for the sample containing unlabeled lipid and ^{15}N labeled peptide, it is possible to account for the $\Delta S/S_0$ values in the ^{13}C lipid labeled samples by only considering dephasing of the natural abundance peptide carbonyl signal. This analysis suggests negligible dephasing of the lipid carbonyls.

Table 9. REDOR Control Experiments.

Sample ^a	$\Delta S/S_0^b$	Figure
FP-(F8L9G10) _C /FP-unlabeled/LM-3	0.01 (0.01)	31a
FP-(F8L9G10) _N /FP-unlabeled/LM-3	0.20 (0.05)	31b
FPK3-unlabeled/LM-3	-0.01 (0.06)	31c
FP-(F8L9G10) _N /LM-4	0.03 (0.02)	31d
FP-(F8L9G10) _N /LM-3	0.41 (0.05)	n.s. ^c
FP-unlabeled/LM-4	0.01 (0.03)	n.s.
FP-(F11L12G13) _C	0.03 (0.02)	n.s.
FPK3-(A14A15G16) _N	0.35 (0.02)	n.s.
FPK3-unlabeled	0.00 (0.02)	n.s.

^a Samples with LM-3 or LM-4 contained peptide bound to hydrated membranes. All other samples were lyophilized dry peptide. For membrane-associated peptide samples, the overall peptide:lipid molar ratio was $\sim 1:25$ and for samples containing two peptides, the peptide:peptide molar ratio was $\sim 1:1$.

^b The uncertainty is enclosed in parentheses.

^c not shown in a figure.

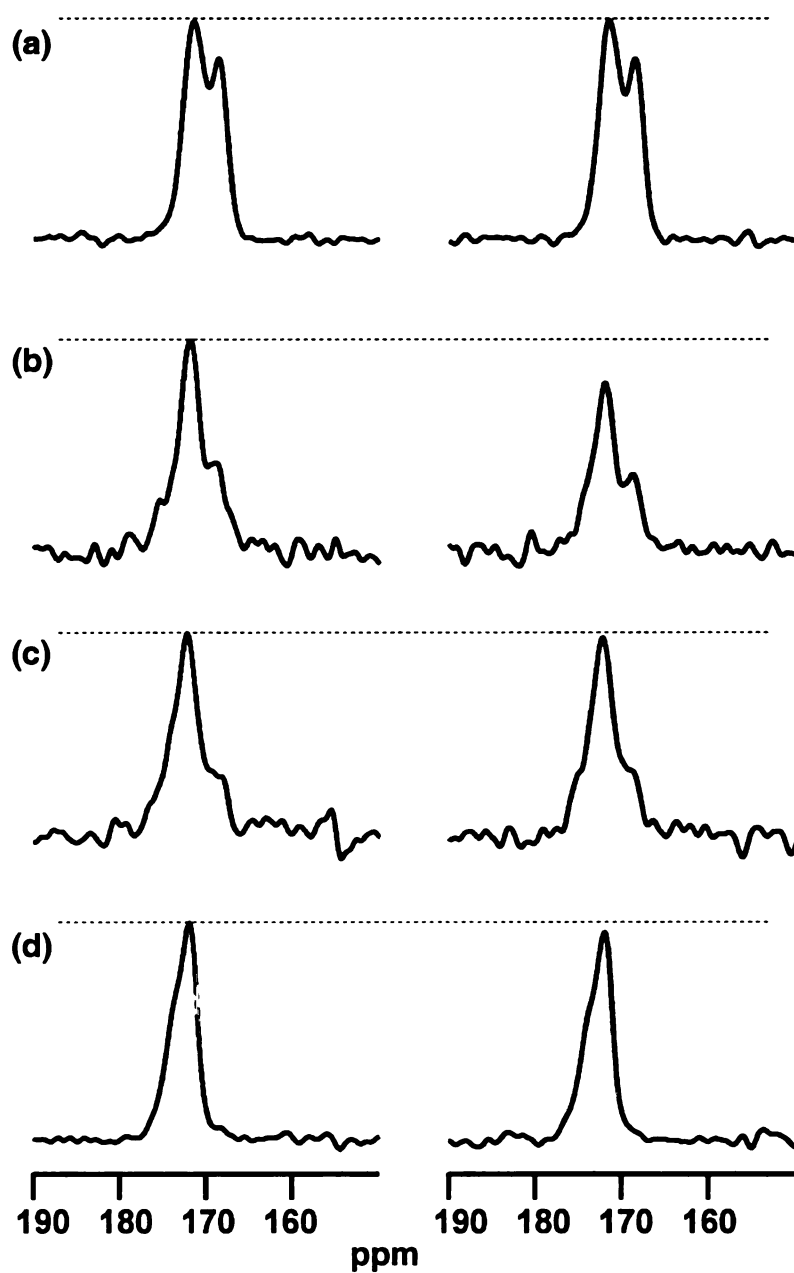


Figure 32. ^{13}C solid-state NMR S_0 (left) and S_1 (right) REDOR spectra of membrane-associated fusion peptides that had (a) $\sim 0.8 \mu\text{mol}$ each of FP-(F8L9G10)_C and FP-unlabeled, (b) $\sim 0.8 \mu\text{mol}$ each of FP-(F8L9G10)_N and FP-unlabeled, (c) $\sim 1.6 \mu\text{mol}$ FPK3-unlabeled, and (d) $\sim 1.6 \mu\text{mol}$ FP-(F8L9G10)_N. Each of the samples in (a-d) also contained $40 \mu\text{mol}$ lipid and $20 \mu\text{mol}$ cholesterol. For samples (a-c), LM-3 lipid mixture was used and for sample (d), LM-4 lipid mixture was used.

The overall conclusion of the control experiments is that $(\Delta S/S_0)_{\text{background}} \sim 0.03$ for the LM-3 samples with a 1:1 mixture of labeled ^{13}C and ^{15}N peptides, which is $\sim 2/3$ due to dephasing of natural abundance peptide carbonyl by labeled ^{15}N and $\sim 1/3$ due to dephasing of labeled peptide carbonyl by natural abundance ^{15}N . The contribution of the lipid carbonyl to $(\Delta S/S_0)_{\text{background}}$ is negligible.

REDOR Experiments to Probe Inter-Peptide Hydrogen Bonding. Figure 32a-h displays the S_0 and S_1 REDOR spectra of membrane-associated fusion peptide samples and the associated $\Delta S/S_0$ values are listed in Table 10. Each sample was made with LM-3 lipid mixture (40 μmol lipid and 20 μmol cholesterol), $\sim 0.8 \mu\text{mol}$ peptide with selective ^{13}C carbonyl labeling, and $\sim 0.8 \mu\text{mol}$ peptide with selective ^{15}N amide labeling.

Four samples (cf. Figure 32a-d) were prepared to probe for the presence of an approximate in-register parallel arrangement of peptide strands. In each of these samples, the labeling in the ^{13}C peptide and in the ^{15}N peptide was at the same set of three sequential residues. With these four samples, inter-strand hydrogen bonding of parallel strands was probed between Gly-5 and Gly-16. For the samples labeled between Gly-5 and Gly-13, the $\Delta S/S_0$ values were in the 0.11 - 0.13 range which is significantly above the 0.03 background value. For the sample containing peptide labeled between Ala-14 and Gly-16, $\Delta S/S_0 \sim 0.03$ which is the approximate background signal. Thus, it appears there is a population of peptides with parallel arrangements of strands, and this arrangement frays apart towards the C-terminal side of the peptide. These results are schematically presented in Figure 33a and are consistent with a reasonable biophysical model based on the peptide sequence. In the sequence, the N-terminal and central regions only contain apolar residues while the C-terminal region contains a substantial fraction of

polar or charged residues. For extended peptides in an oligomeric parallel strand arrangement, the apolar regions of all strands would be on one end of the oligomer and the polar regions would be on the other end of the oligomer. The apolar end of the oligomer may insert into the membrane so that in this region, the strands must hydrogen bond to one another, while the polar end of the oligomer is likely outside the membrane where the strands would hydrogen bond to water. This model is supported by previous measurements of carbonyl linewidths along the peptide backbone. In the N-terminal and central regions, the linewidths are 2 - 3 ppm, which indicates a narrow distribution of secondary structures with a regular hydrogen bonding pattern whereas in the C-terminal region, the linewidths are ~ 5 ppm, which indicates random coil structure and irregular hydrogen bonding.

Four samples (cf. Figure 32e-f) were also prepared to probe for anti-parallel arrangement of peptide strands. The midpoint of the arrangement was chosen to be between Gly-10 and Phe-11, which is about the middle of the peptide. For example, the sample used for Fig. 32h contained peptide which was ^{13}C labeled at Ala-14, Ala-15, and Gly-16, and peptide which was ^{15}N labeled at Gly-5, Ala-6, and Leu-7. For these four “anti-parallel arrangement” samples, the $\Delta S/S_0$ values were in the 0.08 ~ 0.16 range, and were significantly above the background level. Thus, in addition to the previously described parallel strand population, there also appears to be an anti-parallel strand population whose inter-peptide hydrogen bonding continues at least from Gly-5 to Gly-16. This result is schematically presented in Fig. 33b. For extended peptides in an oligomeric anti-parallel strand arrangement, there would be both polar and apolar ends of strands on each end of the oligomer, which is qualitatively different than what is expected

for a parallel strand arrangement. Because of this mixed polarity, it is less clear whether an anti-parallel oligomer would just stay on the surface or insert through the membrane.

Table 10. REDOR Measurements to Probe Inter-Peptide Hydrogen Bonds.

	Sample ^a	$\Delta S/S_0$ ^b	Figure
Parallel Arrangement Probed	FPK3-(G5A6L7) _C /FPK3-(G5A6L7) _N /LM-3	0.13 (0.01)	32a
	FP-(F8L9G10) _C /FP-(F8L9G10) _N /LM-3	0.13 (0.01)	32b
	FP-(F11L12G13) _C /FP-(F11L12G13) _N /LM-3	0.11 (0.01)	32c
	FPK3-(A14A15G16) _C /FPK3-(A14A15G16) _N /LM-3 ^c	$\left. \begin{array}{l} 0.01 (0.03) \\ 0.04 (0.02) \end{array} \right\}$	$\left. \begin{array}{l} 32d \\ \text{n.s.}^d \end{array} \right\}$
Anti-parallel Arrangement Probed	FPK3-(G5A6L7) _C /FPK3-(A14A15G16) _N /LM-3 ^c	$\left. \begin{array}{l} 0.11 (0.01) \\ 0.12 (0.02) \end{array} \right\}$	$\left. \begin{array}{l} \text{n.s.} \\ 32e \end{array} \right\}$
	FP-(F8L9G10) _C /FP-(F11L12G13) _N /LM-3	0.08 (0.02)	32f
	FP-(F11L12G13) _C /FP-(F8L9G10) _N /LM-3	0.09 (0.02)	32g
	FPK3-(A14A15G16) _C /FPK3-(G5A6L7) _N /LM-3	0.16 (0.02)	32h

^a The overall peptide:lipid mol ratio was ~ 1:25.

^b The uncertainty is enclosed in parentheses.

^c Two samples were prepared and measured separately.

^d not shown in a figure.

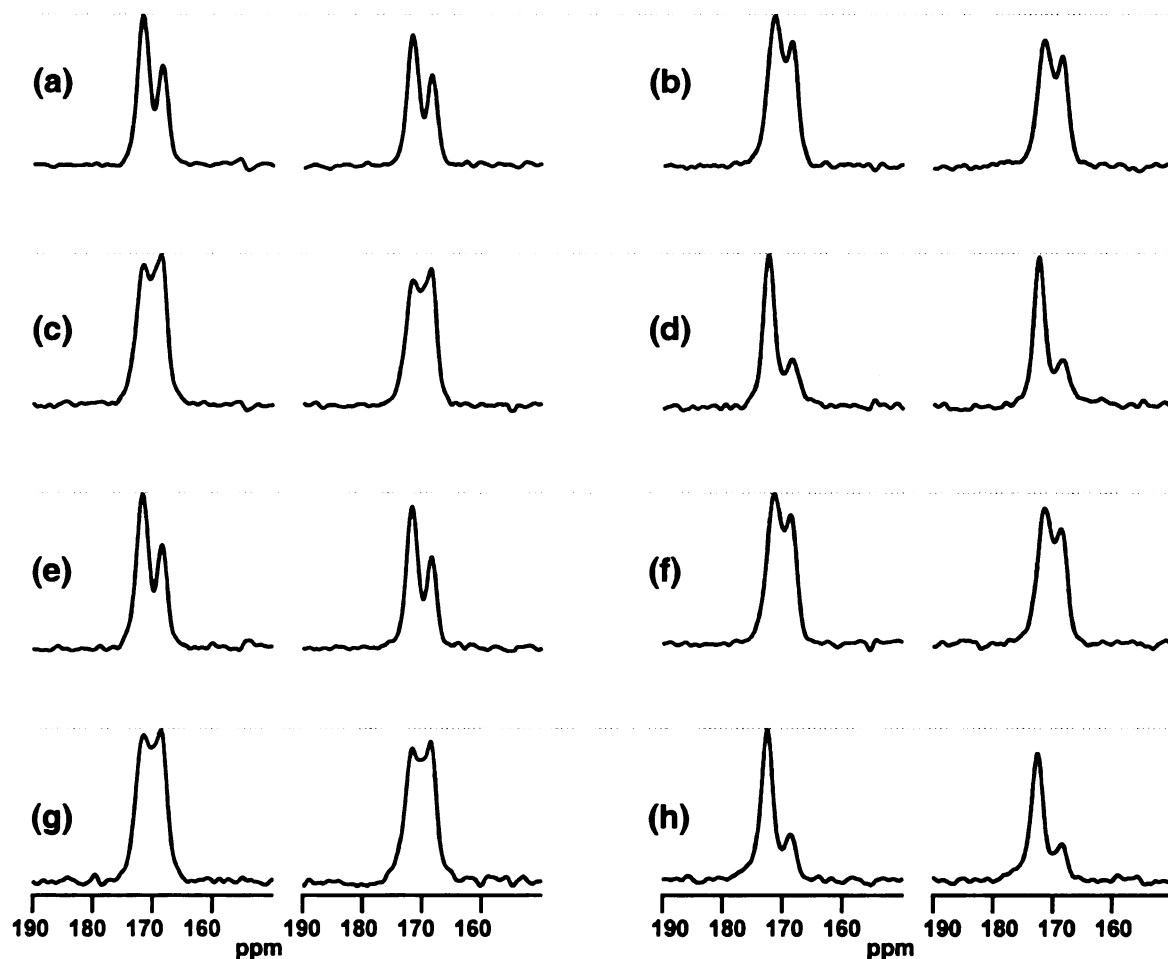


Figure 33. ^{13}C solid-state NMR S_0 and S_1 REDOR spectra of membrane-associated fusion peptides. Each sample was made with LM-3 lipid mixture, $\sim 0.8 \mu\text{mol}$ peptide with selective ^{13}C carbonyl labeling and $\sim 0.8 \mu\text{mol}$ peptide with selective ^{15}N amide labeling. The specific labeling schemes were: (a) FPK3-(G5A6L7)_C/FPK3-(G5A6L7)_N, (b) FP-(F8L9G10)_C/FP-(F8L9G10)_N, (c) FP-(F11L12G13)_C/FP-(F11L12G13)_N, (d) FPK3-(A14A15G16)_C/FPK3-(A14A15G16)_N, (e) FPK3-(G5A6L7)_C/FPK3-(A14A15G16)_N, (f) FP-(F8L9G10)_C/FP-(F11L12G13)_N, (g) FP-(F11L12G13)_C/FP-(F8L9G10)_N, and (h) FPK3-(A14A15G16)_C/FPK3-(G5A6L7)_N. Samples (a)-(d) primarily probed the presence of parallel strand arrangements and samples (e)-(h) primarily probed the presence of anti-parallel strand arrangements. The dotted lines are included for visual comparison of the spectral intensities.

Because most samples probing for parallel and antiparallel strand arrangements had comparable $\Delta S/S_0$ values, it is likely that there are roughly equal populations of each arrangement. Such arrangements could exist for fully extended peptides in a β sheet or β barrel structure or they could exist for peptides in a β hairpin structure. For the present inter-peptide hydrogen bonding study, we also considered whether $\Delta S/S_0$ values predicted for a totally extended oligomeric β strand model matched the experimental $\Delta S/S_0$ values. If the experimental values are significantly less than the predicted values, then there may be a population of hairpin peptides with intra-peptide hydrogen bonding.

In the extended peptide model, we considered that the total S_0 carbonyl signal had contributions from labeled ^{13}C in the peptide, natural abundance ^{13}C in the peptide, and natural abundance ^{13}C in the lipid. These contributions are denoted S_0^{C} , S_0^{N} , and S_0^{L} , respectively. There are corresponding contributions S_1^{C} , S_1^{N} , and S_1^{L} to the total S_1 signal. In quantifying ^{13}C , one ^{13}C labeled peptide, one ^{15}N labeled peptide, and 50 lipid molecules are considered in the sample. The ^{13}C peptide has three labels and S_0^{C} is set to 3.0. The following calculations were made for the other S_0 signals.

$$\begin{aligned} S_0^{\text{N}} &= (\text{number of unlabeled peptide carbonyl C}) \times (\text{natural abundance } ^{13}\text{C}) \\ &= 49 \times 0.011 = 0.539 \end{aligned} \quad (7a)$$

$$\begin{aligned} S_0^{\text{L}} &= (\text{number of lipid}) \times (\text{number of lipid carbonyl C per lipid molecule}) \times \\ &\quad (\text{signal per lipid } ^{13}\text{C}/\text{signal per peptide } ^{13}\text{C}) \times (\text{natural abundance } ^{13}\text{C}) \\ &= 50 \times 2 \times 0.11 \times 0.011 = 0.121 \end{aligned} \quad (7b)$$

For the S_0^{N} calculation, we considered the FPK3 peptide with 26 residues. As described in the “REDOR Control Experiments” section, $S_1^{\text{L}} \approx S_0^{\text{L}}$. Considering the spectrum

displayed in Fig. 31b, we approximate that $S_1^N \approx 0.8 \times S_0^N = 0.431$. Using the simulation result of the labeled ^{13}C dipole-coupled to three adjacent three ^{15}N , we approximate that $S_1^C \approx 0.50 \times S_0^C$ for the case where all three labeled ^{13}C on one strand are hydrogen bonded with ^{15}N on adjacent strands. Because the experimental samples contain a 1:1 mixture of ^{13}C and ^{15}N labeled peptide, there is only 50% probability that a ^{13}C labeled strand will be adjacent to a ^{15}N labeled strand. Therefore, a corrected $S_1^C \approx 0.75 \times S_0^C = 2.25$ was used in the calculations.

Using all of these results, the total $\Delta S/S_0$ for the extended strand model was calculated:

$$\begin{aligned} \Delta S/S_0 &= 1 - (S_1/S_0) \\ &= 1 - (2.25 + 0.431 + 0.121)/(3.0 + 0.539 + 0.121) = 0.23 \quad (8) \end{aligned}$$

As described in the “REDOR Control Experiments” section, $(\Delta S/S_0)_{\text{background}} \sim 0.03$, so the labeled ^{13}C - ^{15}N hydrogen bond contribution to dephasing, $(\Delta S/S_0)_{\text{model}}$, is ~ 0.20 . Comparison with experimental data was made using results from the FPK3-(G5A6L7)_C/FPK3-(G5A6L7)_N/LM-3 and FPK3-(G5A6L7)_C/FPK3-(A14A15A16)_N/LM-3 samples as measures of $(\Delta S/S_0)_{\text{expt.-parallel}}$ and $(\Delta S/S_0)_{\text{expt.-antiparallel}}$, respectively. After subtracting $(\Delta S/S_0)_{\text{background}}$ from each of the experimental $\Delta S/S_0$, we obtain values of $(\Delta S/S_0)_{\text{expt.-parallel}} \approx 0.10$ and $(\Delta S/S_0)_{\text{expt.-antiparallel}} \approx 0.08$. The total hydrogen bonding component of $\Delta S/S_0$ for the FPK3-(G5A6L7)_C peptide, $(\Delta S/S_0)_{\text{expt.}}$, is ~ 0.18 , which is comparable to $(\Delta S/S_0)_{\text{model}}$. This result suggests that the extended oligomeric structures account for much of the membrane-associated peptide population. The 10-15% difference between $(\Delta S/S_0)_{\text{model}}$ and $(\Delta S/S_0)_{\text{expt.}}$ could be due to uncertainties in the experimental data and model, different alignments of peptide strands than the fully in-register

arrangements used for the model, and/or a population of β turn peptides with intra-peptide hydrogen bonding. Intra-peptide hydrogen bonding was not probed in the experiments of this study.

DISCUSSION AND CONCLUSION

In this chapter, we applied solid-state NMR internuclear distance measurements to develop a structural model for the non-helical form of the membrane-associated HIV-1 fusion peptide. This work was based on previous solid-state NMR chemical shift and 2D exchange measurements which showed that the peptide is predominantly non-helical when associated with membranes whose lipid headgroup and cholesterol composition is close to that found in the virus and its target T cells. One of the possible non-helical structures is oligomeric β strands held together by inter-peptide hydrogen bonding and we did experiments to detect this type of structure. In membrane-associated fusion peptide samples containing a 1:1 mixture of ^{13}C carbonyl labeled and ^{15}N amide labeled peptide, detection of ^{13}C - ^{15}N proximity by solid-state NMR REDOR measurements strongly supports this structural model. Moreover, the semi-quantitative agreement between the $\Delta S/S_0$ values predicted by the model and the experimental $\Delta S/S_0$ values suggests that the oligomeric β strand structure represents a substantial population of the membrane-associated peptide. Solid-state NMR experiments are currently underway to test whether all of the peptide is fully extended or whether there is also a population of peptide with hairpin structure.

A second important result is that the data were consistent with roughly equal populations of peptide in parallel or antiparallel strand arrangements. Inter-strand

hydrogen bonding was observed from Gly-5 through Gly-16 in the antiparallel arrangement but only from Gly-5 through Gly-13 in the parallel arrangement. C-terminal fraying in the parallel arrangement is consistent with previous solid-state NMR linewidth measurements and with a reasonable biophysical model in which the apolar N-terminal and central regions of the oligomer insert into the membrane while the polar C-terminal region is outside the membrane. Experiments by other groups also suggest that the C-terminal region is not membrane-inserted, although some of these measurements suggest that this region is helical, rather than the random coil structure indicated by our previously published experiments². These different structures may be a result of the different lengths of the C-terminal regions used in the different studies.

The present study also provides some insight into oligomer formation. In chapter two, the analytical ultracentrifugation data strongly suggest that the 26-residue FPK3 construct is predominantly monomeric in the buffer solution, so formation of membrane-associated β strand oligomers can be a direct result of peptide/membrane interaction. In addition, the analytical ultracentrifugation data suggest that the 23-residue FP construct forms a mixture of oligomeric states in the buffer solution. In the initial step of FP solid-state NMR sample preparation, separate solutions of ^{13}C and ^{15}N labeled peptide were made and contained either ^{13}C or ^{15}N oligomers. After FP/membrane association, the solid-state NMR REDOR data showed significant $\Delta S/S_0$ values (comparable to those of FPK3 samples), which means that the membrane-associated FP oligomers were a molecular mixture of ^{13}C and ^{15}N labeled peptides. This transformation from separated to mixed oligomers could have been a result of exchange in aqueous solution. However, the ^{13}C and ^{15}N peptide solutions were mixed only briefly prior to addition of liposomes, and

we believe that it is more likely that the FP oligomers disassemble and reassemble upon interaction with the membrane. This disassembly/reassembly model is consistent with the experimental observation that an influenza fusion peptide which is oligomeric in aqueous solution can be converted to a helical structure upon membrane binding^{27, 28}. It is also consistent with ideas and experiments from other groups^{14, 29}; in particular, the fusogenically disruptive Val-2 to Glu-2 point mutation in the HIV-1 fusion peptide was correlated with formation of peptide dimers rather than the larger oligomers found for the wild-type peptide¹³. It was therefore hypothesized that the mutant peptide prevented the proper membrane-mediated assembly of peptides required for fusion activity. This idea was supported by studies showing that viruses which had 90% wild-type/10% mutant gp41 had only 40% of the infectivity of viruses which had 100% wild-type gp41¹⁸.

In summary, solid-state NMR has been applied to detect oligomeric β strand structure in the membrane-associated HIV-1 fusion peptide as a result of peptide/lipid interaction. A roughly equal mixture of parallel and antiparallel strand arrangements was observed with fraying of the strands towards the C-terminus in the parallel arrangement. These studies provide a basis to develop a more refined model of the peptide structure and to understand how it may catalyze membrane fusion.

REFERENCE

1. Epand, R. F., Macosko, J. C., Russell, C. J., Shin, Y. K., and Epand, R. M. (1999) The ectodomain of HA2 of influenza virus promotes rapid pH dependent membrane fusion. *J. Mol. Biol.* 286, 489-503.
2. Peisajovich, S. G., Epand, R. F., Pritsker, M., Shai, Y., and Epand, R. M. (2000) The polar region consecutive to the HIV fusion peptide participates in membrane fusion. *Biochemistry* 39, 1826-1833.
3. Peisajovich, S. G., Samuel, O., and Shai, Y. (2000) Paramyxovirus F1 protein has two fusion peptides: implications for the mechanism of membrane fusion. *J. Mol. Biol.* 296, 1353-1365.
4. Suarez, T., Gallaher, W. R., Agirre, A., Goni, F. M., and Nieva, J. L. (2000) Membrane interface-interacting sequences within the ectodomain of the human immunodeficiency virus type 1 envelope glycoprotein: putative role during viral fusion. *J. Virol.* 74, 8038-8047.
5. Sackett, K., and Shai, Y. (2002) The HIV-1 gp41 N-terminal heptad repeat plays an essential role in membrane fusion. *Biochemistry* 41, 4678-4685.
6. Peisajovich, S. G., Blank, L., Epand, R. F., Epand, R. M., and Shai, Y. (2003) On the interaction between gp41 and membranes: The immunodominant loop stabilizes gp41 helical hairpin conformation. *J. Mol. Biol.* 326, 1489-1501.
7. Chan, D. C., Fass, D., Berger, J. M., and Kim, P. S. (1997) Core structure of gp41 from the HIV envelope glycoprotein. *Cell* 89, 263-273.
8. Tan, K., Liu, J., Wang, J., Shen, S., and Lu, M. (1997) Atomic structure of a thermostable subdomain of HIV-1 gp41. *Proc. Natl. Acad. Sci. U. S. A.* 94, 12303-12308.
9. Weissenhorn, W., Dessen, A., Harrison, S. C., Skehel, J. J., and Wiley, D. C. (1997) Atomic structure of the ectodomain from HIV-1 gp41. *Nature* 387, 426-430.
10. Caffrey, M., Cai, M., Kaufman, J., Stahl, S. J., Wingfield, P. T., Covell, D. G., Gronenborn, A. M., and Clore, G. M. (1998) Three-dimensional solution structure of the 44 kDa ectodomain of SIV gp41. *EMBO J.* 17, 4572-4584.
11. Yang, Z. N., Mueser, T. C., Kaufman, J., Stahl, S. J., Wingfield, P. T., and Hyde, C. C. (1999) The crystal structure of the SIV gp41 ectodomain at 1.47 Å resolution. *J. Struct. Biol.* 126, 131-144.

12. Gordon, L. M., Curtain, C. C., Zhong, Y. C., Kirkpatrick, A., Mobley, P. W., and Waring, A. J. (1992) The amino-terminal peptide of HIV-1 glycoprotein 41 interacts with human erythrocyte membranes: peptide conformation, orientation and aggregation. *Biochim. Biophys. Acta* 1139, 257-274.
13. Kliger, Y., Aharoni, A., Rapaport, D., Jones, P., Blumenthal, R., and Shai, Y. (1997) Fusion peptides derived from the HIV type 1 glycoprotein 41 associate within phospholipid membranes and inhibit cell-cell Fusion. Structure- function study. *J. Biol. Chem.* 272, 13496-13505.
14. Pritsker, M., Rucker, J., Hoffman, T. L., Doms, R. W., and Shai, Y. (1999) Effect of nonpolar substitutions of the conserved Phe11 in the fusion peptide of HIV-1 gp41 on its function, structure, and organization in membranes. *Biochemistry* 38, 11359-11371.
15. Munoz-Barroso, I., Durell, S., Sakaguchi, K., Appella, E., and Blumenthal, R. (1998) Dilation of the human immunodeficiency virus-1 envelope glycoprotein fusion pore revealed by the inhibitory action of a synthetic peptide from gp41. *J. Cell Biol.* 140, 315-323.
16. Bentz, J. (2000) Minimal aggregate size and minimal fusion unit for the first fusion pore of influenza hemagglutinin-mediated membrane fusion. *Biophys. J.* 78, 227-245.
17. Bentz, J. (2000) Membrane fusion mediated by coiled coils: a hypothesis. *Biophys J* 78, 886-900.
18. Freed, E. O., Delwart, E. L., Buchschacher, G. L., Jr., and Panganiban, A. T. (1992) A mutation in the human immunodeficiency virus type 1 transmembrane glycoprotein gp41 dominantly interferes with fusion and infectivity. *Proc. Natl. Acad. Sci. U. S. A.* 89, 70-74.
19. Bevington, P. R., and Robinson, D. K. (1992) *Data Reduction and Error Analysis for the Physical Sciences*, McGraw-Hill, Boston.
20. Bak, M., Rasmussen, J. T., and Nielsen, N. C. (2000) SIMPSON: A general simulation program for solid-state NMR spectroscopy. *J. Magn. Reson.* 147, 296-330.
21. Oas, T. G., Hartzell, C. J., McMahon, T. J., Drobny, G. P., and Dahlquist, F. W. (1987) The carbonyl C-13 chemical-shift tensors of 5 peptides determined from N-15 dipole-coupled chemical-shift powder patterns. *J. Am. Chem. Soc.* 109, 5956-5962.
22. Balbach, J. J., Yang, J., Weliky, D. P., Steinbach, P. J., Tugarinov, V., Anglister, J., and Tycko, R. (2000) Probing hydrogen bonds in the antibody-bound HIV-1

- gp120 V3 loop by solid state NMR REDOR measurements. *J. Biomol. NMR* 16, 313-327.
23. Derrick, J. P., and Wigley, D. B. (1994) The third IgG-binding domain from streptococcal protein G. An analysis by X-ray crystallography of the structure alone and in a complex with Fab. *J. Mol. Biol.* 243, 906-918.
 24. Gullion, T., and Vega, S. (1992) A simple magic angle spinning NMR experiment for the dephasing of rotational echoes of dipolar coupled homonuclear spin pairs. *Chem. Phys. Lett.* 194, 423-428.
 25. Bennett, A. E., Ok, J. H., Griffin, R. G., and Vega, S. (1992) Chemical shift correlation spectroscopy in rotating solids - radio frequency-driven dipolar recoupling and longitudinal exchange. *J. Chem. Phys.* 96, 8624-8627.
 26. Bennett, A. E., Rienstra, C. M., Griffiths, J. M., Zhen, W. G., Lansbury, P. T., and Griffin, R. G. (1998) Homonuclear radio frequency-driven recoupling in rotating solids. *J. Chem. Phys.* 108, 9463-9479.
 27. Yang, J., Parkanzky, P. D., Bodner, M. L., Duskin, C. G., and Weliky, D. P. (2002) Application of REDOR subtraction for filtered MAS observation of labeled backbone carbons of membrane-bound fusion peptides. *J. Magn. Reson.* 159, 101-110.
 28. Parkanzky, P. D., and Weliky, D. P., unpublished experiments.
 29. Han, X., and Tamm, L. K. (2000) pH-dependent self-association of influenza hemagglutinin fusion peptides in lipid bilayers. *J. Mol. Biol.* 304, 953-965.

CHAPTER VII

SUMMARY AND FUTURE DIRECTIONS OF THE RESEARCH

The ultimate goal of this research on the fusion peptide is to gain insight into its role in inducing/catalyzing viral/host cell fusion. The earlier part of the work involves the examination of the biological functionality of various synthetic fusion peptide constructs and their structures prior to the binding of membrane lipids. These studies demonstrate that the free peptide without the rest of the gp41 protein can serve as a good model to understand the fusion mechanism. Sample preparation studies confirm that the structure we observed in solid-state NMR is indeed the membrane-associated structure and biologically relevant.

The structural plasticity of membrane-associated fusion peptides has been observed by several groups using a variety of experimental probes and it is known that they can exist in well-structured helical or non-helical forms^{1, 2}. Other investigators have developed structural models for the helical form of the peptides based principally on solution NMR, ESR, and infrared data³⁻⁵. In the next step of our work, we applied various solid-state NMR techniques (chemical shift analysis of 1D CP/MAS experiments and peptide dihedral angle analysis from 2D exchange experiments) that provided strong evidence for the presence of an extended β strand conformation in the N-terminal and central regions of the membrane-bound peptide. The C-terminus is more disordered.

In the fusogenic atomic-resolution structure of the gp41 ectodomain, the protein is trimeric and its three N-termini are in close proximity at the end of an in-register helical coiled-coil. These structures end several residues C-terminal of the fusion peptide and it has therefore been hypothesized that during viral/target cell fusion, at least three fusion peptides insert into the target cell membrane with their C-termini in close proximity⁶⁻¹⁰. The observation of β strand conformation also suggests that the close proximity may be

the result of forming peptide oligomers. REDOR spectroscopy, a solid-state NMR technique, was applied to detect inter-peptide hydrogen bonds in membrane-associated fusion peptide samples that have equimolar amounts of two peptides, one with selective ^{13}C carbonyl labeling and the other with selective ^{15}N amide labeling. Comparison of REDOR spectra on samples that were labeled at different residue positions suggests that there are both parallel and anti-parallel arrangements of peptide strands in the oligomers with about equal populations. In the parallel arrangement, inter-peptide hydrogen bonding decreases toward the C-terminus while in the antiparallel arrangement, hydrogen bonds are observed along the entire length of residues which was probed (Gly-5 to Gly-16). For the parallel arrangement, these observations are consistent with the model in which the apolar N-terminal and central regions of the peptides penetrate into the membrane and hydrogen bond with one another while the polar C-terminus of the peptide is outside the membrane and hydrogen bonds with water, which is also consistent with the previous measurements of carbonyl linewidths along the peptide backbone. In the N-terminal and central regions, the linewidths are 2 ~ 3 ppm, which indicates a narrow distribution of secondary structures with a regular hydrogen bonding pattern whereas in the C-terminal region, the linewidths are ~ 5 ppm, which indicates random coil structure and irregular hydrogen bonding.

It is useful to consider our results in the context of the membrane fusion. The samples were made by the insertion of the fusion peptide into the membrane from aqueous solution, which is likely the means by which the viral peptide domain inserts into the target cell membrane. The fusion activity results in Chapter II also provide evidence for the fusogenic nature of the peptide under conditions comparable to those

used in the preparation of solid state NMR samples. Thus, the observed β strand conformation likely reflects at least the end-state fusogenic structure of the peptide domain.

The oligomerization study also provided information about the expected fusion peptide topology in the gp41 protein. Structures of the gp41 soluble ectodomain begin around residue 30 and are trimeric with the three N-termini in close proximity at the end of an in-register helical coiled-coil. These structures end several residues C-terminal of the fusion peptide and it has been hypothesized that during viral/target cell fusion, at least three fusion peptides insert into the target cell membrane with their C-termini in close proximity⁶⁻¹⁰. In the HIV-1 fusion peptide model system, the biological topology has been mimicked with C-terminal cross-linking, and it has been observed that in many cases, the cross-linked peptides induce both a greater final extent and a more rapid rate of fusion than their non-cross-linked analogs¹¹. Similar fusogenic enhancements have been observed for influenza protein domains for which the fusion peptide is thought to assume the biologically relevant oligomeric topology^{3, 12-17}. In these contexts, it is appealing that a fusion peptide population was indeed observed in the present study with an approximately in-register parallel strand arrangement. This arrangement seems like a reasonable continuation of the known ectodomain oligomeric structure and this arrangement also has a defined apolar region of the fusion peptide oligomer which could insert into the membrane and catalyze fusion. For the non-cross-linked peptides used for the present study, a population of peptide with anti-parallel strand arrangement was also observed. In the anti-parallel arrangement, it is not as clear how the oligomer might insert into the membrane and catalyze fusion. Thus, the fusogenic enhancement of the HIV-1

cross-linked peptides may be in part due to their preference for a parallel strand arrangement.

There are several remaining questions about the structures of membrane-associated oligomeric β strand HIV-1 fusion peptides including:

- (1) the relative populations of hairpin and extended structures;
- (2) the effect of the biologically relevant oligomeric topology on the relative populations of parallel and antiparallel strand arrangements;
- (3) the overall oligomer size and the number of peptides with a particular strand arrangement;
- (4) the precise residue register(s) between neighboring strands in a particular arrangement.
- (5) the insertion of the oligomer into the membrane.

Question (5) has been previously investigated with fluorescence and ESR measurements but the data analyses may have been complicated by the presence of parallel and antiparallel oligomers which may have different insertion depths¹⁸⁻²⁰. These questions are currently investigated using solid-state NMR and other biophysical techniques.

Larger biological questions include the relative fusogenicities of the helical and non-helical forms of the peptide and the possible role of transient structures in fusion catalysis. At least for the influenza fusion peptide, it appears that both helical and non-helical forms are fusogenic and that there is not a single transient fusogenic structure²¹. For the helical form of the influenza fusion peptide, some of the relationships between point mutations and fusogenicity have been correlated with structural changes, in particular angle and depth of membrane insertion^{5, 22}. For the non-helical form of the

HIV-1 fusion peptide, the mutation/fusogenicity data have generally been correlated both with membrane insertion and with oligomer size, but more work needs to be done to establish the structure-function relationships^{19, 23, 24}. Finally, we note that data from our lab suggest that the relative populations of helical and non-helical peptide structures are significantly affected by the lipid and cholesterol composition of the target membrane²⁵. Further experiments, computer simulation, and modeling will be necessary to understand the specific peptide/peptide, peptide/lipid, peptide/cholesterol interactions which underly the molecular mechanism of HIV-1 viral fusion.

REFERENCE

1. Durell, S. R., Martin, I., Ruyschaert, J. M., Shai, Y., and Blumenthal, R. (1997) What studies of fusion peptides tell us about viral envelope glycoprotein-mediated membrane fusion (review). *Mol. Membr. Biol.* 14, 97-112.
2. Suarez, T., Gomara, M. J., Goni, F. M., Mingarro, I., Muga, A., Perez-Paya, E., and Nieva, J. L. (2003) Calcium-dependent conformational changes of membrane-bound Ebola fusion peptide drive vesicle fusion. *FEBS Lett.* 535, 23-28.
3. Macosko, J. C., Kim, C. H., and Shin, Y. K. (1997) The membrane topology of the fusion peptide region of influenza hemagglutinin determined by spin-labeling EPR. *J. Mol. Biol.* 267, 1139-1148.
4. Han, X., Bushweller, J. H., Cafiso, D. S., and Tamm, L. K. (2001) Membrane structure and fusion-triggering conformational change of the fusion domain from influenza hemagglutinin. *Nat. Struct. Biol.* 8, 715-720.
5. Epand, R. M., Epand, R. F., Martin, I., and Ruyschaert, J. M. (2001) Membrane interactions of mutated forms of the influenza fusion peptide. *Biochemistry* 40, 8800-8807.
6. Chan, D. C., Fass, D., Berger, J. M., and Kim, P. S. (1997) Core structure of gp41 from the HIV envelope glycoprotein. *Cell* 89, 263-273.
7. Tan, K., Liu, J., Wang, J., Shen, S., and Lu, M. (1997) Atomic structure of a thermostable subdomain of HIV-1 gp41. *Proc. Natl. Acad. Sci. U. S. A.* 94, 12303-12308.
8. Weissenhorn, W., Dessen, A., Harrison, S. C., Skehel, J. J., and Wiley, D. C. (1997) Atomic structure of the ectodomain from HIV-1 gp41. *Nature* 387, 426-430.
9. Caffrey, M., Cai, M., Kaufman, J., Stahl, S. J., Wingfield, P. T., Covell, D. G., Gronenborn, A. M., and Clore, G. M. (1998) Three-dimensional solution structure of the 44 kDa ectodomain of SIV gp41. *EMBO J.* 17, 4572-4584.
10. Yang, Z. N., Mueser, T. C., Kaufman, J., Stahl, S. J., Wingfield, P. T., and Hyde, C. C. (1999) The crystal structure of the SIV gp41 ectodomain at 1.47 Å resolution. *J. Struct. Biol.* 126, 131-144.
11. Yang, R., Yang, J., and Weliky, D. P. (2003) Synthesis, enhanced fusogenicity, and solid state NMR measurements of cross-linked HIV-1 fusion peptides. *Biochemistry* 42, 3527-3535.

12. Kim, C. H., Macosko, J. C., Yu, Y. G., and Shin, Y. K. (1996) On the dynamics and confirmation of the HA2 domain of the influenza virus hemagglutinin. *Biochemistry* 35, 5359-5365.
13. Kim, C. H., Macosko, J. C., and Shin, Y. K. (1998) The mechanism for low-pH-induced clustering of phospholipid vesicles carrying the HA2 ectodomain of influenza hemagglutinin. *Biochemistry* 37, 137-144.
14. Epand, R. F., Macosko, J. C., Russell, C. J., Shin, Y. K., and Epand, R. M. (1999) The ectodomain of HA2 of influenza virus promotes rapid pH dependent membrane fusion. *J. Mol. Biol.* 286, 489-503.
15. LeDuc, D. L., Shin, Y. K., Epand, R. F., and Epand, R. M. (2000) Factors determining vesicular lipid mixing induced by shortened constructs of influenza hemagglutinin. *Biochemistry* 39, 2733-2739.
16. Leikina, E., LeDuc, D. L., Macosko, J. C., Epand, R., Shin, Y. K., and Chernomordik, L. V. (2001) The 1-127 HA2 construct of influenza virus hemagglutinin induces cell-cell hemifusion. *Biochemistry* 40, 8378-8386.
17. Epand, R. F., Yip, C. M., Chernomordik, L. V., LeDuc, D. L., Shin, Y. K., and Epand, R. M. (2001) Self-assembly of influenza hemagglutinin: studies of ectodomain aggregation by in situ atomic force microscopy. *Biochim. Biophys. Acta-Biomembr.* 1513, 167-175.
18. Gordon, L. M., Curtain, C. C., Zhong, Y. C., Kirkpatrick, A., Mobley, P. W., and Waring, A. J. (1992) The amino-terminal peptide of HIV-1 glycoprotein 41 interacts with human erythrocyte membranes: peptide conformation, orientation and aggregation. *Biochim. Biophys. Acta* 1139, 257-274.
19. Kliger, Y., Aharoni, A., Rapaport, D., Jones, P., Blumenthal, R., and Shai, Y. (1997) Fusion peptides derived from the HIV type 1 glycoprotein 41 associate within phospholipid membranes and inhibit cell-cell Fusion. Structure- function study. *J. Biol. Chem.* 272, 13496-13505.
20. Saez-Cirion, A., and Nieva, J. L. (2002) Conformational transitions of membrane-bound HIV-1 fusion peptide. *Biochim. Biophys. Acta-Biomembr.* 1564, 57-65.
21. Parkanzky, P. D., and Weliky, D. P., unpublished experiments.
22. Tamm, L. K., Han, X., Li, Y. L., and Lai, A. L. (2002) Structure and function of membrane fusion peptides. *Biopolymers* 66, 249-260.
23. Pereira, F. B., Goni, F. M., Muga, A., and Nieva, J. L. (1997) Permeabilization and fusion of uncharged lipid vesicles induced by the HIV-1 fusion peptide

adopting an extended conformation: dose and sequence effects. *Biophys. J.* 73, 1977-1986.

24. Pritsker, M., Rucker, J., Hoffman, T. L., Doms, R. W., and Shai, Y. (1999) Effect of nonpolar substitutions of the conserved Phe11 in the fusion peptide of HIV-1 gp41 on its function, structure, and organization in membranes. *Biochemistry* 38, 11359-11371.
25. Bodner, M. L., Gabrys, C. M., Parkanzky, P. D., Yang, J., Duskin, C. A., and Weliky, D. P. Temperature dependence and resonance assignment of ¹³C NMR spectra of selectively and uniformly labeled fusion peptides associated with membranes. *Magn. Reson. Chem.*, in press.

MICHIGAN STATE UNIVERSITY LIBRARIES



3 1293 02504 7923